Understanding the Structure and Reactivity of Solid State Electrolyte Model Systems

By

Joey Allen Lussier

A Thesis submitted to the Faculty of Graduate Studies of

The University of Manitoba

in partial fulfilment of the requirements of the degree of

DOCTOR OF PHILOSOPHY

Department of Chemistry

University of Manitoba

Winnipeg

Abstract

Solid oxide fuel cells (SOFCs) are considered a promising energy conversion technology for the future. These devices show fuel flexibility, high conversion efficiency, and low emissions. Solid-state electrolytes play a crucial role in improving the performance of SOFCs. Currently, defect fluorites are most commonly used as electrolytes for commercial SOFCs. This thesis focuses primarily on fluorite and fluorite-related structures with the goal of furthering the understanding of oxide defect model systems. The $Y_{2-x}Pr_xO_{3+\delta}$ and $Sc_{2-x}V_xO_{3+\delta}$ ($0 \leq x \leq 2.00$, and $0 \leq \delta \leq 1$) systems will be explored with a particular emphasis on synthesis and structure-reactivity relationships. Using *in-situ* methods, including powder diffraction (both X-ray and neutron), and thermogravimetric analysis, allows for a deeper understanding of reaction pathways, and provides insights into mechanistic details of reactions. Throughout this thesis, comments will be made on the importance of synthesis strategies and understanding structural details when designing functional materials.

Acknowledgements

First and foremost, I'd like to thank my supervisor Dr. Mario Bieringer. The support, guidance, and direction provided throughout my tenure as a student has made this thesis possible. There is no doubt in my mind that without the enormous amount of time and effort that you've invested in me throughout the years, I would not be the scientist I am today.

My committee members, Drs. Chris Wiebe, David Herbert, Can-Ming Hu, and Derek Oliver have been extremely encouraging, and have always been available to answer questions, give input on my projects, or simply have a friendly conversation. For this I am very appreciative.

The Chemistry Department, including the students, professors, and support staff, have always been friendly and open to a conversation. With the many specialties of all members of the department, it is rare to have a question go unanswered. I feel it is especially important to thank Dr. Jennifer van Wijngaarden, for her open door and helpful guidance. Furthermore, I must extend this thanks to the Manitoba Institute for Materials. Jen and Kev, I thank you for all the discussions and lunches, and I'm glad to call you both friends.

The Bieringer group, both past and present, Shahid, Kevin, Graham, Fabian, Golnaz, Diego, Harlyn, Pierre-Olivier, Jenny, Dmitry, Lee, and Jonah. I have learned a lot with you all throughout the years, and I wish you all success in the future.

I would also like to thank every organization that has contributed to my funding over the years, particularly the National Science and Engineering Research Council of Canada (NSERC), the University of Manitoba, and the Department of Chemistry.

To all my collaborators, thank you for the effort that each of you have put in throughout my tenure here. Research is truly a collaborative endeavor and I thank you all for the time you've

dedicated. This includes the many beamline scientists and technicians that have provided support throughout our numerous experiments.

I must thank all of my family and friends for all the patience and understanding, for celebrating the “ups”, and helping me through the “downs” that come with a doctoral degree. The unconditional love and encouragement you’ve shown will never be forgotten.

Finally, to my collaborator-turned-wife Arzoo, thank you for always being by my side, I look forward to many more successful collaborations to come.

Table of Contents

List of Tables

List of Figures

Chapter 1. Introduction

1.1. Solid State Synthesis: Techniques for the Rational Design of Solids

Solid-state materials chemistry is one of the oldest chemical sciences; however, the ability to predict composition, structure, and reaction pathways or mechanisms has lagged behind those of other branches of chemistry, such as organic chemistry.[1] Molecular chemists have long had kinetic control of syntheses, concerning themselves with the mechanistic details of reactions in order to take advantage of activation barriers and kinetically trap the atoms. This allows for molecular design, and the formation of molecules with desired configurations.[2] A critical benefit in these types of syntheses comes from increased access to molecules due to the use of solvents.[3] Furthermore, specific portions of the molecules, such as functional groups, are targeted for transformation.[4] Solid-state methods are adapting to include a variety of approaches which allow for the synthesis of kinetic products or metastable phases. The structure of materials is often directly correlated to the synthesis route used. Pressure, temperature, atmosphere, and the choice of starting materials and their structures all play a large role in determining the product obtained.

Bulk solid-state materials have been formed in many ways including, but not limited to, conventional solid-state synthesis, sol-gel synthesis,[5,6] microwave synthesis,[7] and hydrothermal synthesis.[8,9] In this thesis, the synthesis of metastable solid-state materials is a central theme, and

therefore, a variety of techniques will be explored. This section will provide an overview of each of these techniques.

1.1.1. Conventional Solid State Synthesis

The preparation of materials in the solid-state has developed throughout the ages due to the demands of civilization.[10] One of the most common synthesis methods for producing oxide materials is what has come to be known as the conventional solid-state synthesis, or the ceramic method. Colloquially referred to as the "shake and bake" method, the conventional solid-state synthesis method is widely used due to its simplicity. In this method, powders of starting materials, commonly oxides, carbonates, or nitrates, are ground together stoichiometrically, and heated to high temperatures. In order to maximize contact between reagents, the materials are often pressed into pellets prior to heating. The limiting step in most conventional solid-state syntheses is the diffusion of atoms throughout the system and the difficulty in crossing grain boundaries. High temperatures are required in order to promote the diffusion of ions, but because of the large amount of energy being offered to the system, thermodynamic products are commonly found as products. Therefore, disadvantages of this technique include the difficulty in isolating metastable products, as well as the challenge of working with low melting point reagents such as V_2O_5 (m.p. ~670 °C) or Bi_2O_3 (m.p. ~817 °C)[11,12]. Furthermore, at high temperatures reaction with crucibles or other reaction vessels must be monitored.[13]

1.1.2. Sol-Gel Method

Sols are dispersions of colloidal particles in liquids, whereas gels are interconnected three dimensional rigid networks containing pores.[6] In this method, the nature of both sols and gels are taken advantage of in order to form a desired product. An organic reagent (e.g. citric acid) is used to help with the gelation process and because it can be easily removed using combustion. This technique involves the dissolution of compounds in order to achieve near-atomistic mixing, the formation of a gel in order to avoid inhomogeneous precipitation, followed by the combustion of the organic component, and the subsequent reaction of the remaining components (the desired metal oxides).[5] These steps are visualized in figure 1.1. The main advantage of this technique is that typically lower reaction temperatures are required. The metal oxide product can be formed at considerably lower temperatures than with the conventional solid-state method, because transport between grains is often a limiting factor in conventional solid-state reactions. This phenomenon was shown in the synthesis of $CoAl_2O_4$ by Zayat, et al.[14]

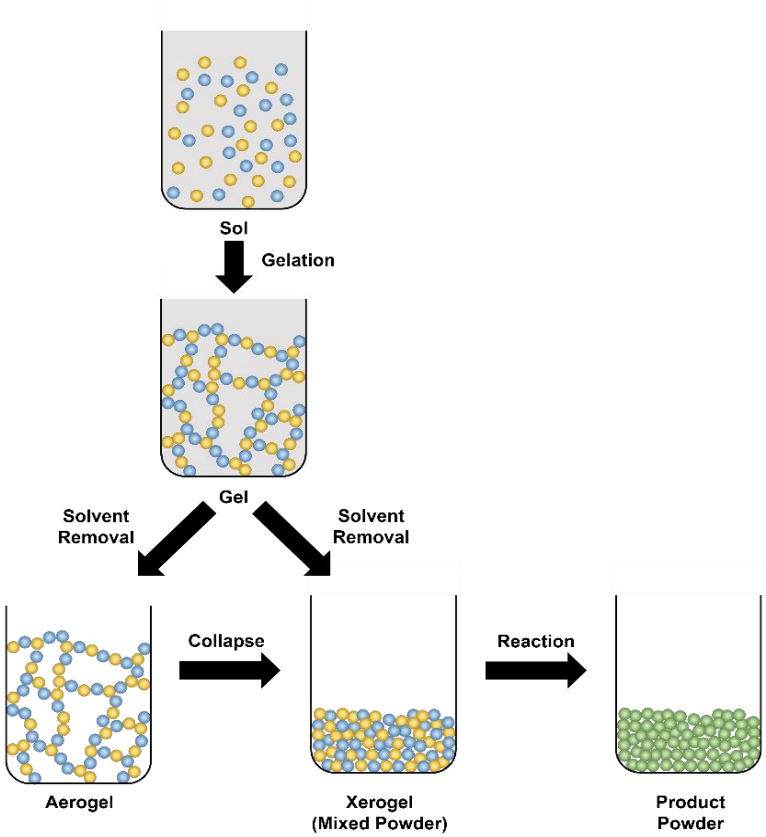

Figure 1.1 Schematic of the processes in a sol-gel synthesis.

1.1.3. Topotactic Synthesis

The term topotactical, also referred to as topotactic, or topochemical was proposed by Lotgering in 1959, to describe a reaction for which the topology of the ions is conserved throughout the reaction.[15] Topotactic reactions offer a way to manipulate host materials at significantly lower temperatures than conventional methods, allowing access to materials which cannot be made using high temperatures.[3] These metastable materials are often stable up to temperatures of several hundred degrees, preserving their usefulness as materials in technologically relevant devices. During topotactic reactions, weakly bonded substructures are modified, whereas the more strongly bonded substructure is left intact.[16] The most common topotactic methods are intercalation,[17,18] ion exchange,[19,20] substitution,[21,22] and deintercalation.[23] Recently, solid-state hydrides such as LiH, NaH, and CaH_2 have been used as low-temperature reductants. This topotactic technique has led to many new products with unusual structural features. Rosseinsky and coworkers have used this technique to create layered mixed metal oxides and oxyhydrides;[24–26] Kageyama and coworkers have used this technique to form, for the first time, square planar iron oxide layers;[27,28] and in published work which is not included in this thesis, Lussier et al. reported the reduction of Sr_2MnO_4 to $Sr_2MnO_{3.63(1)}$. This article includes comments on the mechanistic details of metal hydride reductions, including a discussion on the amount of electrons used from each hydride anion for reduction.[29] When combined in series, these individual techniques can complement one another, allowing for a powerful toolbox of solid-state reactions.[30] Wiley and coworkers have published a comprehensive review on the topic of topotactic reactions, focusing on the manipulation of perovskite materials.[3]

1.2. The Importance of Structures

1.2.1. Structure-Property Relationships

In order to rationally design functional materials, a good understanding of the relationship between structures and their properties is necessary. The most relevant example for this thesis is in the design of solid-state electrolytes. The mobility of anions found in the fluorite structure, partially due to its energetically equivalent anion lattice sites, makes it a promising candidate for the development of novel fast ion conductors. This will be discussed in more detail in 1.3. Other examples of the use of structure-property relationships in the rational design of materials include the design of polar materials by Halasyamani and coworkers in order to form new second harmonic generation piezoelectric materials which are also ferroelectric and/or pyroelectric;[31] and the design of novel thermoelectric materials.[32]

1.2.2. The Fluorite Structure

The cubic fluorite structure refers to the mineral fluorite (CaF_2). It can be described with the cations (Ca^{2+}) forming a cubic close packed structure (found in the FCC sublattice) and the anions (F^-) filling all tetrahedral holes. Consequently, FCa_4 units are formed (grey tetrahedron in figure 1.2); however, more commonly shown are the Ca^{2+} ions found in the cubic hole surrounded by 8 fluorine ions (CaF_8 units). These are shown as green cubes in figure 1.2. This structure is not limited to 2+ cations and 1- anions, and is often found for oxide materials where the cation is in the 4+ oxidation state. The fluorite structure crystallizes in the cubic $Fm\bar{3}m$ space group (no. 225), where the cations are found in the *4a* site and the anions are found in the *8c* site. Fluorite phases are very tolerant to anion vacancies, which give rise to defect fluorites ($MX_{2-\delta}$). Because there is

only one site for cations in this structure, in order to maintain the $Fm\bar{3}m$ symmetry, mixed-cation systems must be disordered. Similarly, with only one anion lattice site, oxide defects and mixed anion systems must also be disordered. This causes all anion sites to be energetically equivalent, making the fluorite structure an ideal target structure for the construction of oxide conducting electrolytes (more on this in 1.3).

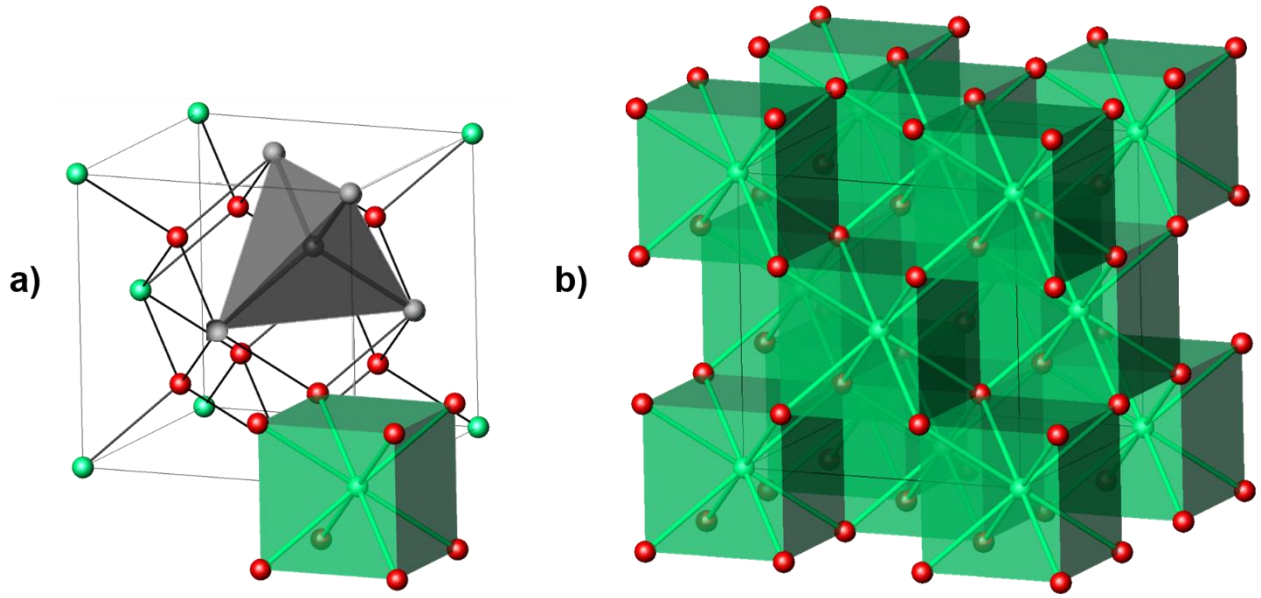

Figure 1.2: Illustrations of the cubic fluorite structure (space group: $Fm\bar{3}m$). Green = Ca^{2+} (*4a* site) and red = F^- (*8c* site). a) Emphasis on the ions in the unit cell, the anionic environment, FCa_4 (grey tetrahedron), and the cationic environment, CaF_8 (green cube). b) Illustrates the cubic fluorite structure as cation polyhedra sharing edges with their nearest neighbours.

1.2.3. The Bixbyite Structure

The bixbyite structure is very similar to the defect fluorite structure, but in this structure, the anions are ordered. The mineral bixbyite ($(Mn,Fe)_2O_3$) has variable Mn:Fe ratios which are disordered over 2 sites (*8b* and *24d*) in space group $Ia\bar{3}$ (no. 206). The anions in this cubic structure are found in the general position *48e*. The bixbyite structure is illustrated in figure 1.3. Most importantly for this work, the bixbyite structure is very tolerant toward addition of extra anions.

These anions are added in the *16c* site, which is shown as orange spheres in figure 1.3b. This, in combination with the fact that the cation sublattice of the bixbyite and fluorite structures have very similar topologies, makes the bixbyite-fluorite system an ideal candidate for low temperature topotactic redox chemistry.

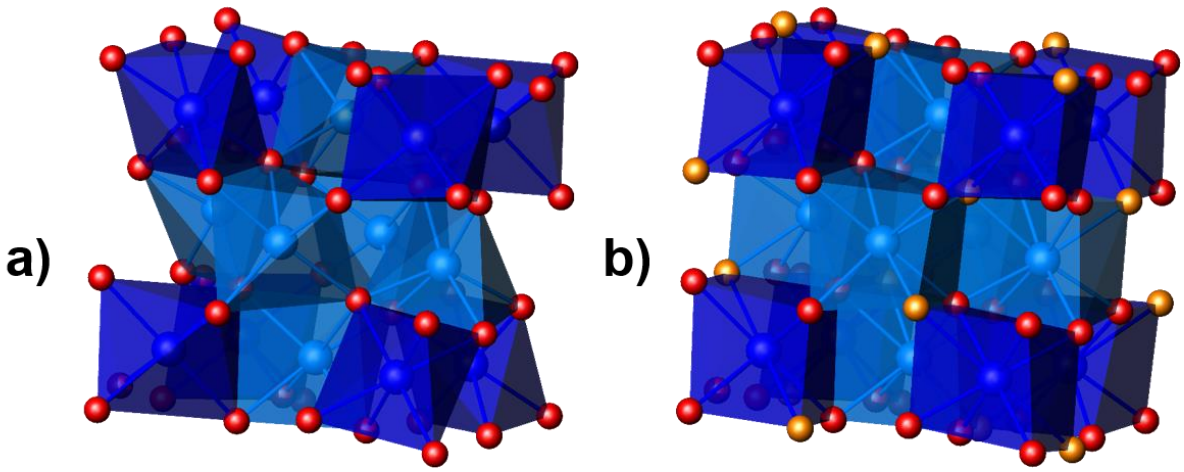

Figure 1.3: Illustration of the cubic bixbyite structure (space group: $Ia\bar{3}$) and the topotactically oxidized product. Blue = cation sites (dark blue = *8b*, light blue = *24d* sites), red = anion sites (*48e* site), orange = oxygen/defects (*16c* site).

1.2.4. The Zircon Structure

The zircon structure is based on the mineral zirconium silicate ($ZrSiO_4$). This is a cation ordered structure, which crystallizes in the tetragonal *I4₁/amd* space group (no. 141). In this structure Zr is found in the *4a* site dodecahedrally (although distorted) coordinated with 8 oxygen anions and Si is found in the *4b* site tetrahedrally coordinated with 4 oxide anions. The isolated

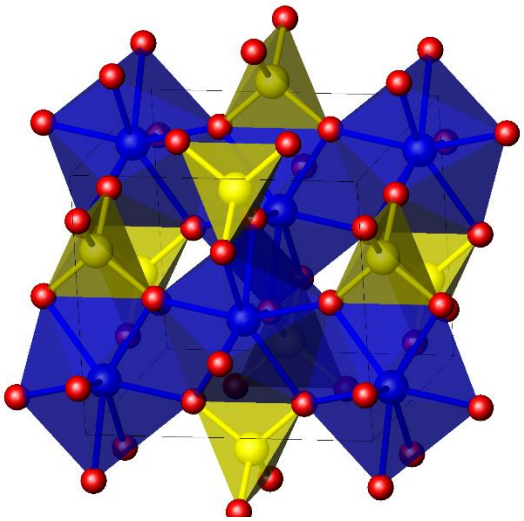

Figure 1.4: Illustration of the zircon structure (space group *I4₁/amd*). Blue = Zr^{4+} (*4a* site), yellow = Si^{4+} (*4b* site), red = O^{2-} (*16h* site).

SiO_4 tetrahedra share corners and edges with the ZrO_8 dodecahedra, which in turn share edges with each other.[33] For this thesis, the zircon structure is important due to the compound $ScVO_4$. $ScVO_4$ is isostructural with $ZrSiO_4$ and has been investigated extensively, along with the other rare earth orthovanadates, for their interesting optical properties.[34–37]

1.2.5. The Corundum Structure

The corundum structure, based on the mineral corundum - a crystalline form of aluminium oxide (Al_2O_3), crystallizes in the rhombohedral space group $R\bar{3}c$ (no. 167). The cations are octahedrally coordinated to 6 oxides and the anions tetrahedrally coordinated to 4 cations. This structure is based on a hexagonal close packed array of oxide ions with the cation found in two thirds of the octahedral sites. The vacant sites are ordered in a way that allows each octahedron to share a face with another along the c-axis. Many oxides are found in the corundum structure; some examples include: Ti_2O_3, V_2O_3, Cr_2O_3, and Fe_2O_3.

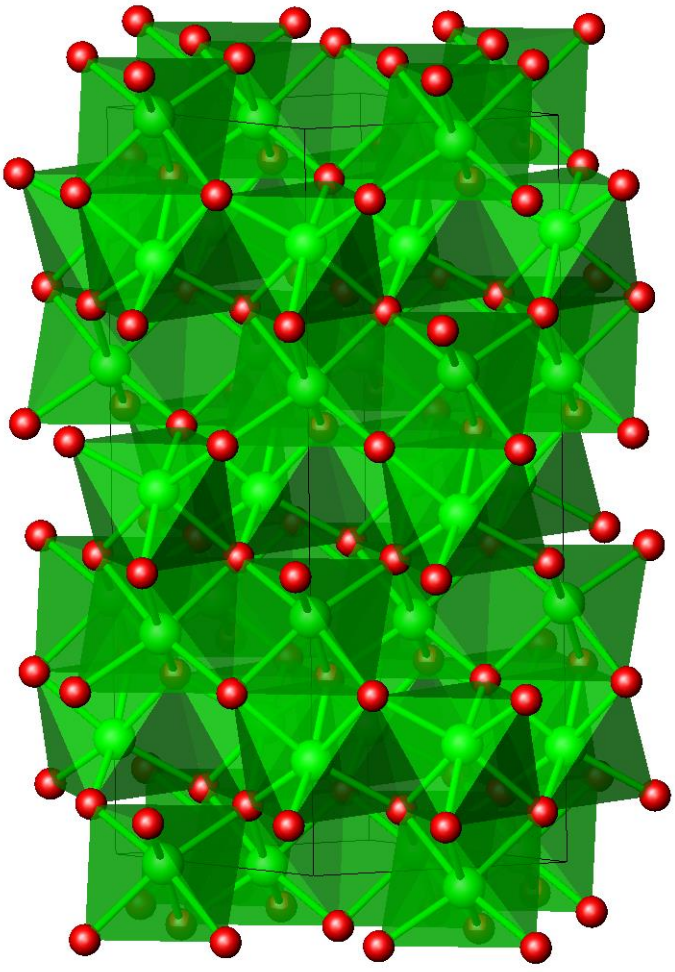

Figure 1.5: Illustration of the corundum structure (space group $R\bar{3}c$. Green = Al^{3+} (*12c* site) Red = O^{2-} (*18e* site).

1.3. Background Literature and Focus of the Project

Materials science has always been an applied science with a strong connection to global and technological needs. Global energy demands have constantly risen, and the World Energy Outlook 2017 predicts that global energy consumption will rise by about 28% between the years 2015 and 2040.[38] In order to avoid the use of fossil fuels, alternative energy resources are necessary. Of these alternative energy resources, those which are clean and sustainable are preferred. Photovoltaics, thermoelectrics, batteries, and fuel cells can all be used for the conversion or storage of energy. To design these devices, a deeper understanding of the materials within is required. To rationally design these materials, their fundamental functions must first be understood. Good model systems which are capable of fostering an understanding towards the relationship between the desired properties and their structures are important. Particularly important for this thesis is the understanding of ion conducting materials for use in solid oxide fuel cells (SOFC). A simple schematic of a SOFC is shown in figure 1.6. Other designs are being used as well, but all SOFCs follow the same general scheme.[39] The cathode and anode are both mixed conductors, conducting ions and electrons, whereas the electrolyte is an electronic insulator and an oxide ionic conductor.

To design an efficient electrolyte, many chemical and engineering-related properties must be optimized. The main requirements for an efficient electrolyte are:[40–42]

(i) High ionic conductivity (0.1 S/cm at operating temperature);

(ii) High electronic resistivity;

(iii) Thermal expansion compatible with the other components of the cell;

(iv) Chemical stability up to operating temperature (especially in contact with the electrodes);

(v) Stability during thermal cycling;

(vi) Low cost.

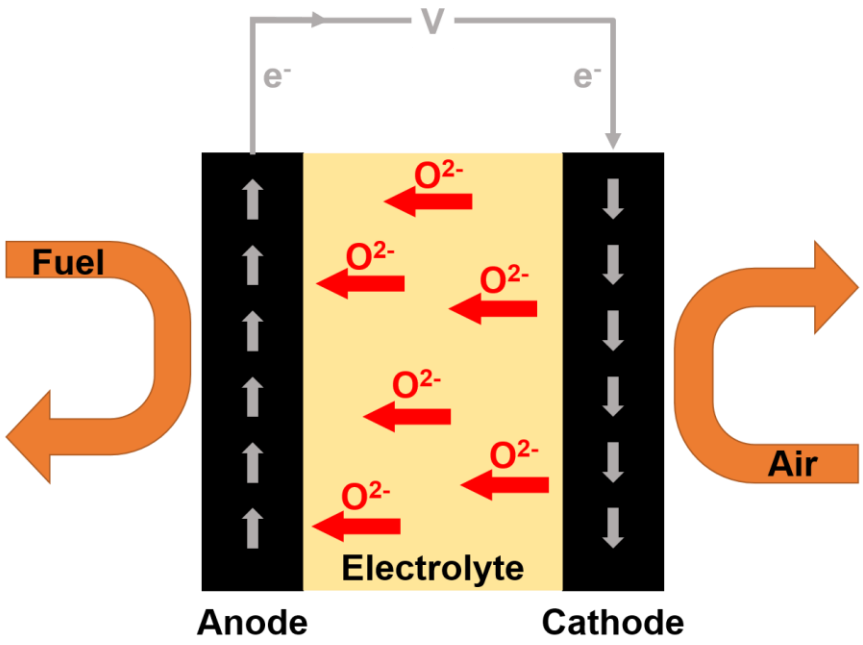

Figure 1.6: Schematic of a solid oxide fuel cell. The grey arrows show the path of electrons, while the red arrows show the path of oxide anions. Oxygen is reduced at the cathode and reoxidized at the anode while converting fuel. The schematic is annotated with all the different components.

In oxide ion conductors, current flow occurs via the movement of the anions through a crystal lattice as a result of thermally-activated hopping between crystal lattice sites. The ionic conductivity is therefore highly temperature dependent.[43] In order to design a good ion conducting material, a few important factors must be considered:

1. The structure must contain unoccupied sites equivalent to those occupied by the oxide anions in the lattice.[44]
2. The activation energy for the hopping process from one site to another must be small. This is difficult to attain because anions are typically the largest ions in the lattice, making cations a more intuitive candidate for mobility.

3. Due to the high operating temperatures of SOFCs the materials must be stable up to high temperatures (at least 800°C).[43]

As mentioned earlier, the fluorite structure has been identified as one which shows a great deal of promise for solid-state oxide ion conducting applications.

Over 200 years ago, Faraday observed that at elevated temperatures fast fluoride ion conduction could be seen in the compound PbF_2.[43,45] This discovery led scientists to investigate the fluorite structure to understand its conductivity. It was found that because there's only one set of anion lattice points which are consequently energetically equivalent, if the anion site is only partially occupied, overcoming a small energy barrier (E_a) is all that is necessary for anions to diffuse. Goodenough reports[45] that oxide ion conductivity σ_o, can be described with:

$$\sigma_o = (A/T)e^{-E_a/kT} \qquad \text{(eq. 1. 1)}$$

where T is the temperature, k is the Boltzmann constant, and A is a factor represented by:

$$A = f(z/6)e^{\Delta S_m/k}(Nq^2/k)n_v(1-n_v)l^2\upsilon_0 \qquad \text{(eq. 1.2)}$$

where f is a geometrical factor which depends on the jump path, z is the number of near neighbour sites, N is the number of normal sites per unit volume, q = 2e (the lattice charge of the oxygen vacancy), n_v is the fraction of vacant sites, l is the distance between neighbouring sites, and υ_o is the frequency of vibrations of the mobile oxide ion. To design a good oxide ion conductor, A must be maximized, while E_a is minimized. An E_a less than about 1 eV has been shown to be reasonable for good oxide ion conductivity.[43] The equivalent anion sites in a fluorite lattice are separated by a shared edge of the surrounding cation tetrahedron. Therefore, in order for the anion to hop from site to site, it must squeeze through this edge, as shown in figure 1.7. E_a represents the energy required for the anion to squeeze through this channel, and it has been found to be lowest when the peripheral cations of this bottleneck are easily polarized.[44] To maximize A, one may conclude

that due to the $n_v(1-n_v)$ term, more defects would make for a better conductor, increasing up to about 50% holes; however, it has been shown that the elastic strain caused by the mismatch in cation size lowers the conductivity significantly.[46–48] Typically, 5% to 10% oxide defects are ideal to optimize the anionic conductivity in these fluorite structures.[40] This defect creation has been attempted in two ways: one way is to substitute cations with a lower charge into the host cation array, creating an extrinsic vacancy concentration; and the other is to choose an oxide with an intrinsic vacancy concentration (a multivalent cation).[45] Most commercial solid-state electrolytes dope with cations which have only one commonly stable oxidation state to create vacancies, which reduces the risk of redox reactions occurring during operation and typically makes synthesis less complicated. The classic oxide conducting electrolytes are yttria-stabilized-zirconia (YSZ) or Gd_2O_3 doped CeO_2. Exchanging the zirconium cation (4+) in zirconia with yttrium or scandium (both 3+) stabilizes the fluorite structure and creates a valuable oxide ion conductor at elevated temperatures. Because of the high price of scandium, YSZ is the electrolyte of choice for SOFC operating at or above 800 °C.[40] The same idea is true for Sm_2O_3 or Gd_2O_3 doped CeO_2, reducing the operating temperature further, to 550 °C.

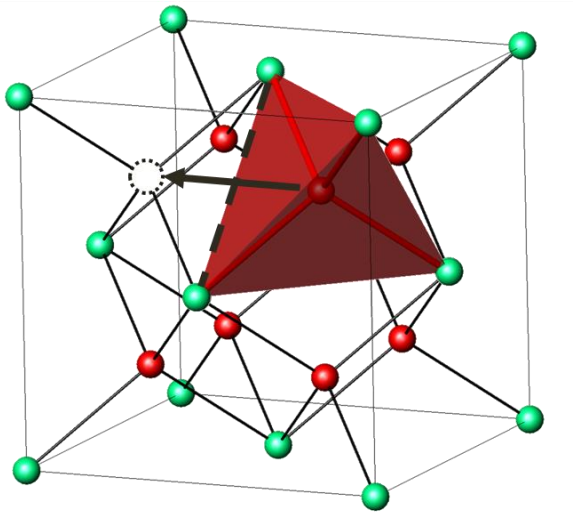

Figure 1.7: Illustration of the oxide hopping mechanism during oxide ion conduction in a fluorite lattice.

Currently, the main goals of SOFC research is to lower the operational temperature down to 300 - 400 °C while retaining a reasonable level of conductivity.[40] However in this thesis, the goal is to explore model systems in detail in order to gain a better understanding of structure-property relationships, which can be applied to more complex materials at a later stage.

1.4. Introduction to Experimental Techniques

1.4.1. Diffraction

1.4.1.1. Introduction

Diffraction techniques have long been used to characterize the structures of crystalline solids. The long range order found in crystalline materials makes diffraction an ideal probe of the arrangement of atoms and ions in crystal lattices. Diffraction relies on the interaction of incident radiation with the material being characterized. Because radiation with wavelengths commensurate to that of atomic sizes and interatomic spacings is required in order for diffraction to occur, wavelengths on the order of 10^{-10} m (angstroms) are typically used. Furthermore, the nature of the radiation used will also have a drastic effect on its interaction with the material. Due to wave-particle duality, the desired wavelength can be achieved using either electromagnetic radiation (EMR) or particles in motion. The EMR with wavelengths in the range of angstroms is that of X-rays. X-rays interact with the electron density (commonly referred to as the electron cloud) of the sample. Particles such as neutrons or electrons may be used as an alternative to X-rays when in motion. The wave-particle duality explains that all physical entities, such as light and matter, exhibit both wave-like and particle-like properties. The de Broglie equation (eq. 1.3) allows us to describe the wavelength of any particle in motion.

$$\lambda = \frac{h}{m\nu} \qquad \text{(eq. 1. 3)}$$

where: h is Planck's constant (h = 6.626x10^{-34} J·s), m is the particle's rest mass, and ν is the particle's velocity. In contrast to X-rays, neutrons interact primarily with the nuclei of atoms; this leads to a much weaker interaction than found with X-rays, so larger samples are needed. Neutrons also often allow the differentiation between neighbouring elements. Furthermore, neutrons have a

magnetic moment which allows for interactions with unpaired electrons in the material. This phenomenon allows for both nuclear and magnetic diffraction to be measured leading to the ability to measure magnetic structures. Finally, electrons are also commonly used for diffraction, they interact much stronger than X-rays or neutrons due to their charged nature. As a result, electron diffraction typically results in multiple scattering events, which eliminates the ability to use the kinematical theory (where an approximation is used that only one scattering event occurs) and complicates the analysis. Electron diffraction was not used in the scope of this work and will not be discussed any further.

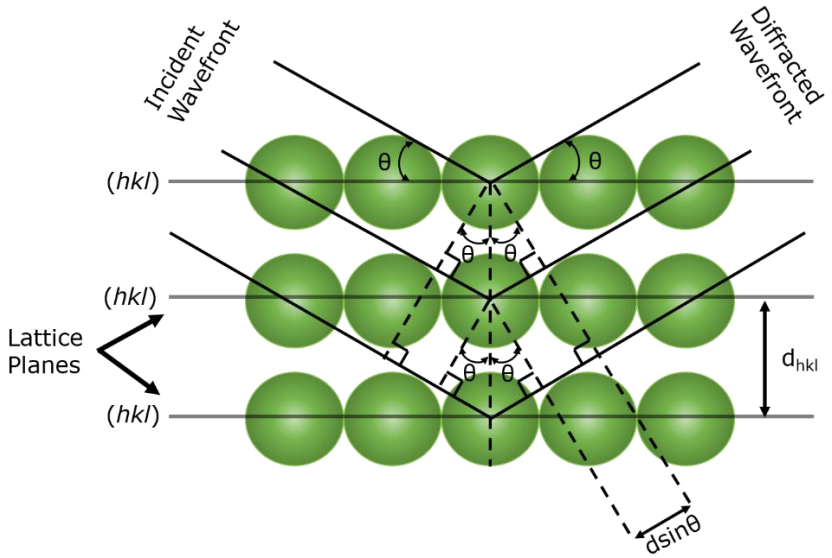

Figure 1.8 Schematic illustration of Bragg's law. The lattice planes, incident and diffracted wavefronts, and all relevant symbols are annotated on the figure.

Diffraction from crystallographic planes can be described using Bragg's law (eq. 1.4) which describes the relationship between the wavelength of the radiation used (λ), the spacing between the sets of lattice planes (d), and the incident angle of incoming X-rays (θ). These planes are described using Miller indices (hkl), where all planes with the same Miller indices are parallel to one another and separated equally. The periodic spacing of these planes act as a diffraction grating.

$$n\lambda = 2dsin\theta \quad \text{(eq. 1. 4)}$$

When Bragg's law is satisfied, the difference in path length between the diffracted beams from different lattice planes is an integer multiple of the wavelength. Satisfying this condition will enable the X-rays to interfere constructively, producing a Bragg peak at the angle 2θ; if the condition is not met, destructive interference will result and no peak will be seen. Figure 1.8 illustrates Bragg's law.

1.4.1.2. Powder X-ray Diffraction (XRD)

1.4.1.2.1. General

Bragg's law allows us to identify the spacing between planes in the crystal lattice; however, to identify and locate the atoms or ions in the unit cell, the intensity of the Bragg peaks becomes important. The integrated intensity of each peak is a function of the atomic structure; however it also depends on a variety of geometrical factors which are expressed as functions of 2θ. In diffraction, the intensity of equivalent peaks (in a powder diffraction pattern) can be expressed using:

$$I_{hkl} = K \times G \times |F_{hkl}|^2 \quad \text{(eq. 1. 5)}$$

where: K is the scale factor, a multiplier which normalizes the observed intensities with absolute intensities due to the fact that scattered intensity is measured in relative and not absolute units;
G represents a variety of geometrical factors including: the multiplicity factor (p_{hkl}), the Lorentz multiplier (L_θ), the polarization factor (P_θ), the absorption multiplier (A_θ), the preferred orientation factor (T_{hkl}), and the extinction parameter (E_{hkl}). The formula for G is:

$$G = p_{hkl} \times L_\theta \times P_\theta \times A_\theta \times T_{hkl} \times E_{hkl} \quad \text{(eq. 1. 6)}$$

where: $|F_{hkl}|^2$ is the structure factor, the square of the absolute value of the structure amplitude (F_{hkl}). This is the factor which describes the nature, distribution, population, and motion of atoms or ions in the unit cell, and can be represented with:

$$F_{hkl} = \sum_{j=1}^{n} g_j t_j(s) f_j(s)\, e^{2\pi i(hx_j + ky_j + lz_j)} \qquad \text{(eq. 1. 7)}$$

where:

n is the total number of atoms or ions in the unit cell, including all symmetrically equivalent atoms or ions;

s is $\sin\theta_{hkl}/\lambda$;

g_j is the occupation factor of the j^{th} atom or ion;

t_j is the temperature factor, describing the thermal motion of j^{th} atom or ion;

$i = \sqrt{-1}$;

hkl are the Miller indices for the peak;

x_j, y_j, z_j are the fractional coordinates for the j^{th} atom or ion in the unit cell;

and, f_j is the atomic scattering factor (or form factor), describing the interaction of the incident wave with the j^{th} atom or ion.

As was mentioned earlier, X-rays scatter off the electron clouds of the atoms found in the crystal lattice. Consequently, the strength of scattering depends on the nature of the atoms or ions found in the crystalline lattice. The scattering power for any single atom or ion is described with a form factor $f_j^0(s)$, which depends on the wavelength of the X-rays used, the diffraction angle, and the nature of the atom or ion in question. At $\sin\theta/\lambda = 0$, the scattering factor is equal to the number of electrons found in the atom or ion. As the diffraction angle is increased the scattering factor will gradually decrease, due to the radial distribution of electrons in the atom or ion.[49] This decay was

modelled by Cromer & Mann[50] based on Hartree-Fock calculations and fitted to the analytical function shown in (eq. 1.8). Nine parameters (a_{1-4}, b_{1-4}, and c) are used to describe the approximation to the scattering factor. The parameters for common atoms and ions can be found published in the International Tables for Crystallography: Volume C.[51]

$$f_j^0\left(sin\theta/\lambda\right) = \sum_{i=1}^{4} a_i\, e^{-b_i(sin^2\theta/\lambda^2)} + c \qquad \text{(eq. 1. 8)}$$

Figure 1.9 illustrates the scattering factor of multiple atoms and ions as a function of sinθ/λ. Most notably, lighter elements scatter much more weakly than heavier elements, making it extremely difficult to obtain reliable parameters (such as positional coordinates) for light elements when heavier elements are present. Furthermore, one can infer that neighbouring elements (or those with similar electron counts) will be difficult to distinguish (i.e. V vs. Ti). Finally, when comparing the form factor curves for Pr vs. Pr^{3+}, one can see that they are only significantly different at low angles (sinθ/λ < 0.25), meaning that different oxidation states also cannot be reliably differentiated.

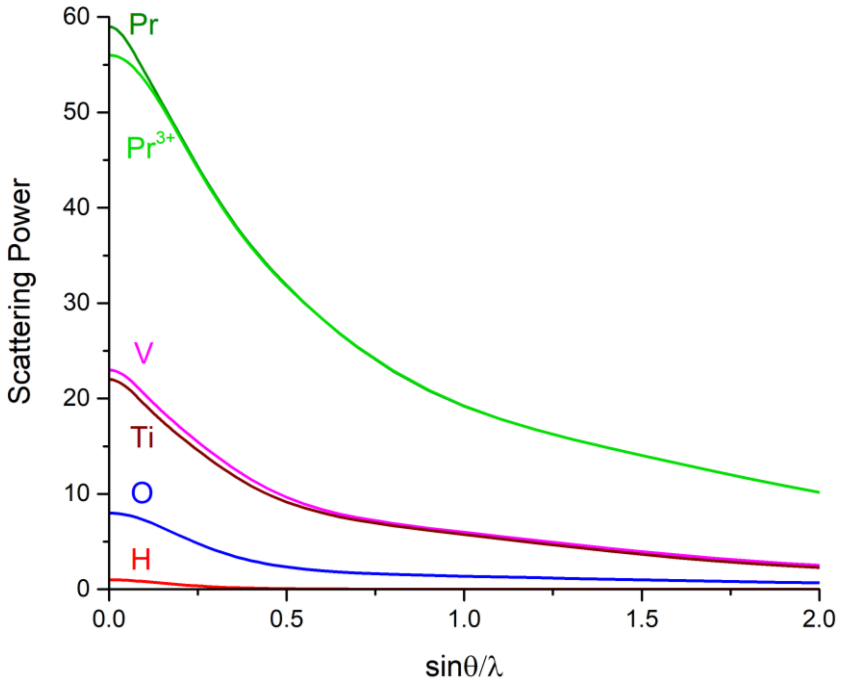

Figure 1.9: Schematic of form factors for H, O, Ti, V, Pr, and Pr^{3+} as a function of sinθ/λ.

Powder X-ray diffraction is typically collected using either lab instruments, which are normally far more convenient, or synchrotron sources which are much more brilliant. These different types of instruments will be further discussed below.

1.4.1.2.2. Laboratory X-ray Diffraction

Powder X-ray diffractometers found in a laboratory setting generally generate X-rays using an X-ray tube as the source. As can be seen in figure 1.10, these X-ray tubes produce X-rays by first ejecting electrons from a cathode material by heating the material beyond its work function. These electrons accelerate in an electrical field from the cathode to a metal target (the anode) in an evacuated tube. Upon collision of the electrons with the anode material, X-rays are formed in two ways: firstly, the fast deceleration of the electron releases X-ray photons with a continuous spectrum; and secondly by ejecting a core electron from the target, causing an electron from a higher shell to take its place, releasing a photon as it relaxes. The radiation produced in this way is characteristic for the material used in the anode, and depends both upon the shell of the vacancy and that of the electron taking its place. Typical

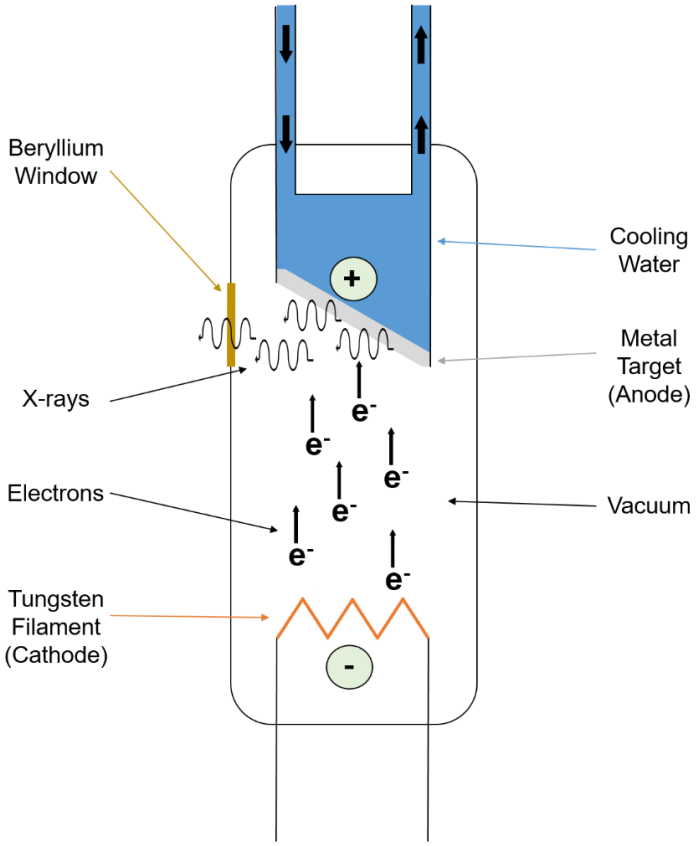

Figure 1.10: Schematic representation of an X-ray tube.

anode materials include copper, molybdenum, iron, cobalt and silver; however, the most common anode material used, and the one that was used throughout this thesis is copper. For copper, the typical radiation used is Kα (average wavelength of 1.5418 Å), which comprised of $K\alpha_1$ and $K\alpha_2$, with wavelengths of 1.54056 Å and 1.54439 Å, respectively.

Once X-rays are produced, they travel through a series of beam optics, in order to shape the beam improving the resolution and final peak shape. This often occurs at the expense of flux. Using a monochromator or filter helps to select the X-ray wavelengths used for the measurement. A monochromator will select a single wavelength, whereas filters will absorb energies higher than a certain threshold depending on the material used. For a copper source, a nickel filter is used in order to remove the unwanted radiation (such as the copper Kβ emission line). The radiation then reaches the sample, where diffraction occurs, and is collected by an X-ray detector. There are many different configurations of diffractometers, including transmission and reflection geometry; however, for the lab diffractometer used in this thesis, the Bragg-Brentano geometry was used. Figure 1.11 shows a schematic of a diffractometer in the Bragg-Brentano (θ - 2θ) setting. In this geometry, the incident beam and the diffracted beam both form the same angle (θ) with the sample stage; consequently, the diffracted beam will form the angle 2θ with the incident beam. The sample is irradiated with a divergent incident beam, and when properly aligned, the beam will self-focus (converge) at the receiving slit, where the detector is located. The focal point of the X-ray source and the receiving slit of the detector are both found on the perimeter of an imaginary circle known as the goniometer circle.[49]

The flat plate sample mount often used for Bragg-Brentano geometry is more susceptible to preferred orientation, and the divergent incident beam causes an angular dependence on the amount of sample being illuminated by X-rays. This effect becomes so extreme at low angles that

beam overspill occurs where a portion of the beam is no longer on the sample, causing unreliable intensities. However, advantages include that the focusing of the diffracted beam results in both high diffracted intensities and high resolution. Furthermore, the effects of absorption are reduced in comparison to transmission geometry, making this setup ideal for samples containing heavier elements.

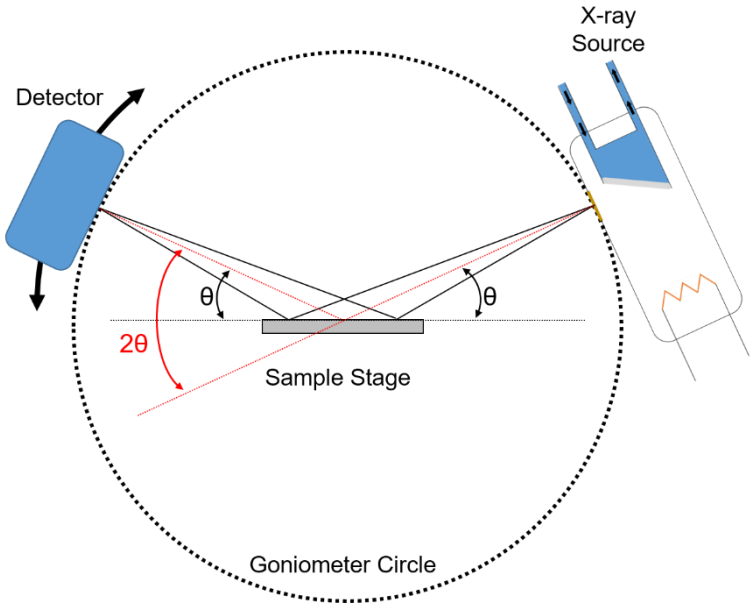

Figure 1.11: Schematic of an X-ray diffractometer in the Bragg-Brentano setting.

The laboratory diffractometer used throughout this thesis is a Panalytical X'Pert Pro (PANalytical B.V., Almelo, the Netherlands) in Bragg-Brentano geometry using Cu-Kα radiation and an X'Celerator detector with 128 microstrip detector elements. Using multiple detector elements allows for faster data collection as all microstrips collect a complete diffractogram covering the full 2θ range. Using acetone slurries, samples are mounted as thin layers on silicon zero background sample holders (Si(510)) and measured on a PW3040/60 sample spinner stage at 1 revolution per second. Incident beam optics include Soller slits, divergence slits, a mask, and an

anti-scatter slit. The diffracted beam optics include an anti-scatter slit, Soller slits and a nickel filter. Details of the experimental setups can be found in each of the individual chapters.

1.4.1.2.3. Synchrotron Diffraction

Currently, the most brilliant X-ray sources are synchrotrons, producing intensities which are orders of magnitudes higher than conventional X-ray tubes. These synchrotron radiation sources began to appear in the 1960's and have been improved upon ever since. Synchrotron X-rays are produced by accelerating charged particles (electrons or positrons) close to the speed of light using a linear accelerator (Linac) and booster ring. These charged particles are injected into a storage ring and, using a magnetic field, forced into a large (almost) circular orbit, typically hundreds of metres in diameter.[49] Using bending magnets, the path of the particles is curved causing a change in momentum; consequently, radiation is given off tangentially. Experimental stations are constructed on these beamlines in order to use the radiation produced. Figure 1.12 shows a schematic of a synchrotron radiation facility. New generation synchrotron sources also include insertion devices on the straight sections, which produce even brighter light. These insertion devices include undulators and wigglers, however the beamlines used in this thesis are all from bending magnets and therefore, insertion devices will not be discussed in detail.

The main properties of synchrotron radiation include very high intensity, broad and continuous spectral range (allowing for the selection of nearly any desired wavelength), natural narrow angular collimation, and high brightness.[52] These combined properties result in very high resolution and intense diffraction patterns.

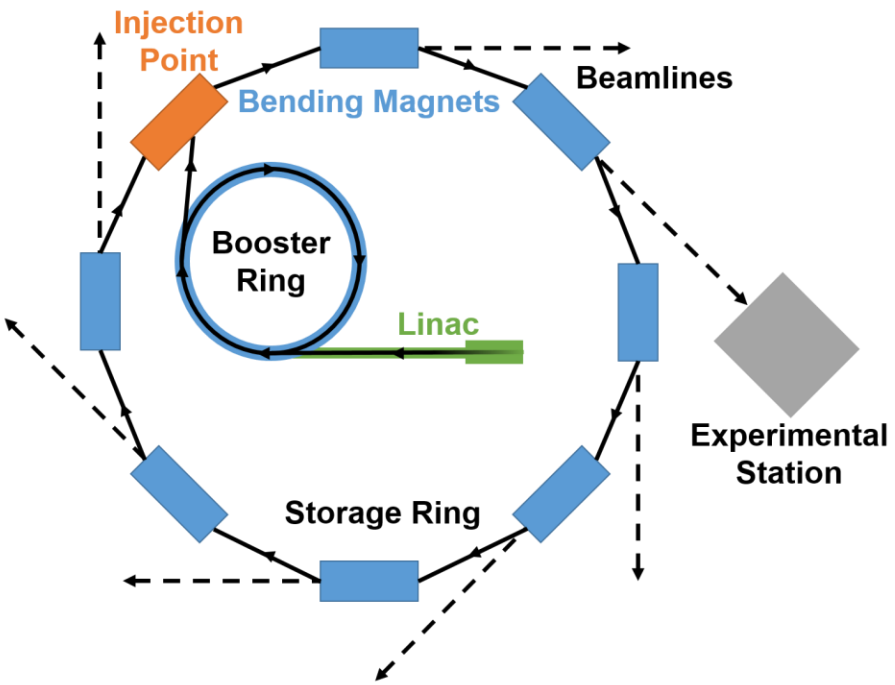

Figure 1.12: Schematic of a synchrotron facility.

Typically, Debye-Scherrer geometry is used at synchrotron sources. In this geometry samples are typically contained in capillaries and parallel beams are used in contrast to a diverging beam for Bragg-Brentano. This avoids the angle-dependence of beam size at the sample, preventing unreliable intensities from beam overspill seen with the Bragg-Brentano geometry. Furthermore, error associated with the focusing circle is eliminated and the effect of preferred orientation is deemphasized. Due to the transmission geometry however, care must be taken to deal with highly absorbing samples via dilution.

In order to produce synchrotron X-rays, large scale facilities are required. Some examples of synchrotron facilities include: The Canadian Light Source (CLS) in Saskatoon, SK, Canada; the Advanced Photon Source (APS) at Argonne National Lab in Argonne, IL, USA; and the European Synchrotron Radiation Facility (ESRF) in Grenoble, France. Throughout the work carried out in

this thesis, beamlines 11-BM-B[53–55] and 17-BM-B at the APS were used extensively. The experimental setups for experiments are mentioned in the individual chapters.

11-BM-B is a beamline which can be operated over the energy range of 15 - 35 keV (λ = 0.83 – 0.35 Å). The beam optics include a collimating mirror with Si and Pt stripes, a 20 mm offset double-crystal Si (111) monochromator (the second of which is bent for horizontal focusing), and a 1 m vertical focusing mirror. The X-ray beam at the sample is approximately 1.5 mm x 0.5 mm at the sample. The sample is located approximately 50 m from the source where a Huber two circle diffractometer mounted on an optical table is used. The 12-analyzer detection assembly is mounted to the main circle of the diffractometer, where the diffracted beam is received by 12 independent Si (111) crystal analyzers before hitting the $LaCl_3$ scintillation detectors. A pair of slits between the sample and each crystal ensures a separated and collimated diffracted beam.

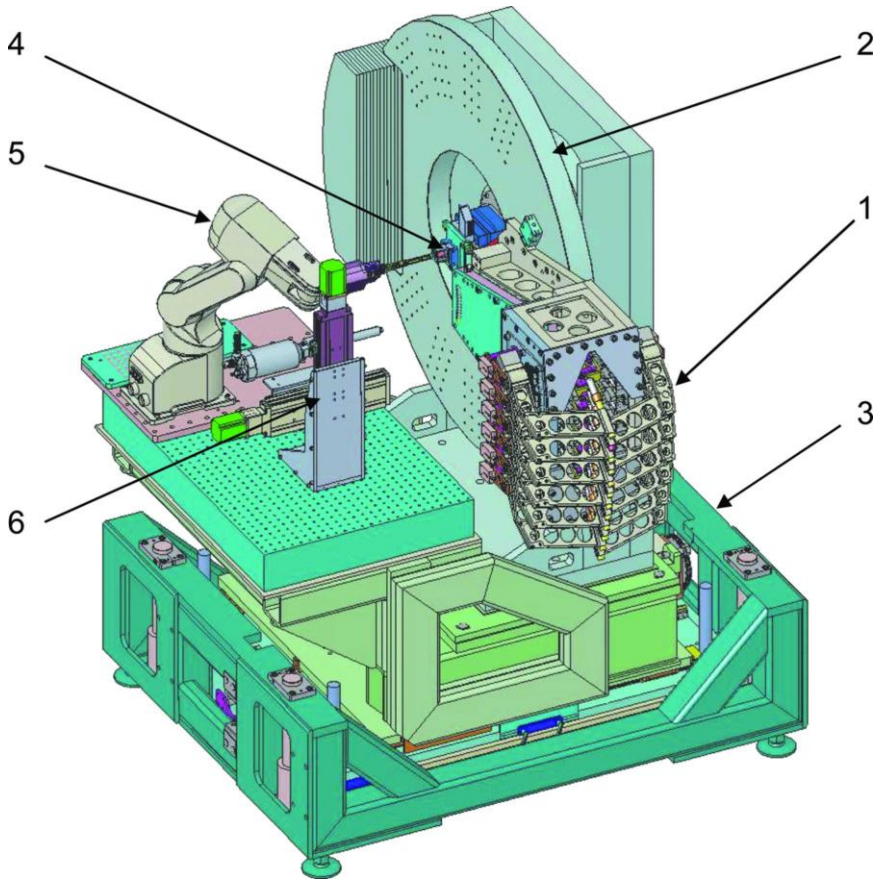

Figure 1.13 A three-dimensional model of the high-resolution diffractometer with 12-analyzer detector system: (1) 12-analyzer detector system, (2) two-circle goniometer, (3) supporting table, (4) sample stages, (5) sample mounting robot, (6) stages for cryostream. Reproduced with permission of the International Union of Crystallography.[54]

There is a 2° separation between neighbouring analyzers, and the entire detector system is rotated around the sample in order to achieve simultaneous high-speed and high-resolution data collection. The angular coverage of the detector is 0.5 – 130 ° and the minimum step size is 0.0001 °. A typical mail-in scan is collected at approximately 0.41 Å (30 keV) for approximately 1 hour with a 2θ range from 0.5 – 50 ° and a step size of 0.001 °. Figure 1.13 shows a 3-dimensional model of the diffractometer found on the beamline 11-BM-B.

17-BM-B is a rapid acquisition powder diffractometer, which is well suited for *in-situ*, *in-operando*, and parametric X-ray diffraction and pair distribution function analysis. It accommodates a wide range of sample environments including flow cells, cryosystems, and high pressure cells, among others. The X-rays produced by the bending magnet source are monochromated using a Si (311) monochromator and focused to 500 x 500 μm at the sample. Pinholes are often used to cut down the beam to smaller sizes to match the sample stage or environment. The monochromator allows the wavelength to be tuned from 0.46 Å to 0.24 Å (27 – 51 keV). That, coupled with a 2D area detector which can be moved from 200 – 1300 mm from the sample allows for a large range of d-spacings to be explored. Typical acquisition times range from 0.1 – 30 s depending on how well the sample diffracts. Diffraction rings from a calibrant are collected on the 2D area detector, as is shown on Figure 1.14 (left) for LaB_6. The known d-spacings of the calibrant are set in order to determine the detector distance, tilt of the detector, along with other parameters. Once calibrated, a typical 1D diffraction plot can be achieved by integrating around the rings, as is seen on figure 1.14 (right).

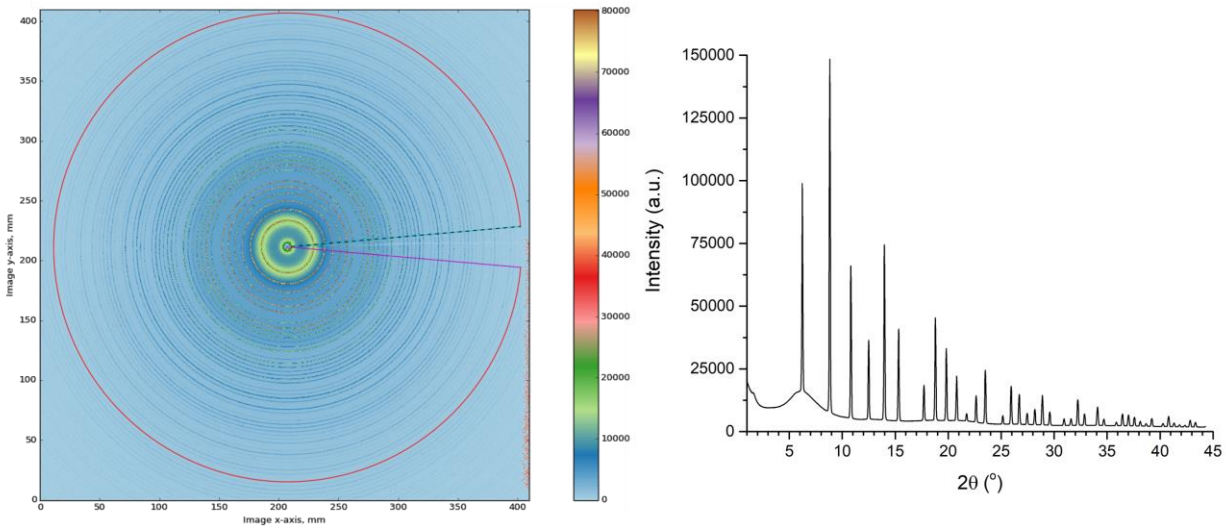

Figure 1.14: (left) 2D scan of LaB_6 using 17-BM-B. The diffraction rings can be seen, and integration area is shown. (right) 1D diffraction plot of LaB_6 after integration of rings.

1.4.1.3. Neutron Powder Diffraction (NPD)

1.4.1.3.1. General

Neutron powder diffraction uses the same principles as X-ray diffraction; however there are a few changes required due to the interaction with the nucleus rather than the electron cloud. One of these differences is that the scattering factors are not 2θ dependent and remain constant over the entire range of diffraction angles. Furthermore, the scattering functions are not proportional to the atomic number, allowing for contrast between neighbouring elements as well as light elements, even when heavier elements are present. Finally, scattering functions are also different for different isotopes of the same element. Interaction with unpaired electrons also allows for magnetic diffraction which is used in order to determine magnetic structures. Magnetic diffraction, although a very useful technique for materials chemists, was not used in this thesis and will not be discussed in detail.

The structure factor for neutron diffraction is similar to that for X-rays (eq. 1.7); however, rather than using the X-ray form factor, the scattering length b is used. This leads to the nuclear structure factor equation:

$$F_{hkl} = \sum_{j=1}^{n} g^j t^j(s) b^j \, e^{2\pi i(hx^j + ky^j + lz^j)} \qquad \text{(eq. 1. 9)}$$

Where b^j is the scattering length of the j^{th} ion or atom in the unit cell, and all other symbols are defined in (eq. 1.7). The scattering length of the neutron-nucleus system describes the strength and the character of the interaction of neutrons with different nuclei. Neutrons can also interact with matter by being absorbed. It is therefore important when dealing with neutron diffraction to know the probabilities of both scattering and absorption occurring. In order to describe these probabilities, neutron cross sections are used. They are typically expressed in units of barns (10^{-24} cm^2), while scattering lengths are described in units of fm. The scattering cross section is related to the scattering length using the equation:[56]

$$\sigma_c = 4\pi b_c^2 \qquad \text{(eq. 1. 10)}$$

Absorption cross sections (σ_{abs}) are measured directly and are used to describe the probability of absorption occurring. Reliable values for cross sections and scattering lengths are necessary for determining the viability of neutron experiments, and for interpretation of these experiment, and are tabulated in the literature.[56–59]

In contrast to X-rays and electrons, neutrons are not easily produced, therefore no small scale lab based neutron diffractometers are available. Neutrons are generated in large facilities using one of two methods (which are described in more detail below): by nuclear fission, in continuous wavelength sources; or by the spallation process, found in spallation sources.

1.4.1.3.2. Continuous Wavelength Sources

Continuous wavelength sources (reactor sources) use nuclear fission to produce neutrons. A thermal neutron is absorbed by ^{235}U, forming ^{236}U, which decays into ^{144}Ba, ^{89}Kr, gamma rays, and three neutrons. These neutrons are either absorbed by another ^{235}U to continue the nuclear reaction, or are liberated and used for diffraction. Neutrons produced in this way are very high energy, on the order of MeV, and need to be slowed before they can be used for diffraction. Moderators are used for this purpose, the temperature of the moderator controls the speed and therefore the wavelength distribution of the neutrons. Room temperature H_2O or D_2O are commonly used as moderators, giving neutron wavelengths in the range of angstroms. Specific wavelengths can be selected with monochromators.

Examples of continuous wavelength sources are the Institut Laue-Langevin (ILL), in Grenoble France; and the former Canadian Neutron Beam Centre (CNBC), at the Canadian Nuclear Laboratories in Chalk River, ON, Canada. In this thesis diffractograms were collected on the 800 wire medium resolution powder neutron diffractometer at C2, found at the former CNBC.

The C2 diffractometer uses neutrons from the 135 MW NRU reactor at the CNBC. At the sample, the beam can be up to 3.656” high and 2.625” wide, but is often masked to smaller sizes. The monochromator take-off angle is variable from 0 - 120°, and many monochromators are available (Be, Cu, Ge, graphites,Si). The wavelength can be varied from 1 Å to 4 Å, and typically the (531) reflection of Si is used. A curved 800-wire BF_3 position sensitive detector with a wire spacing of 0.1° allows for 80° of scattering angle to be measured simultaneously. The detector can be moved in 0.01° steps to increase data density. Furthermore, the detector can be positioned in high- or low-angle settings allowing for a 2θ range of 120°.

1.4.1.3.3. Spallation Sources

Spallation sources are pulsed neutron sources which differ from continuous wavelength sources in many ways. In this method, protons are accelerated using a Linac (and typically kept in a storage ring) before being collided into a heavy metal target at regular intervals. This causes many neutrons to be released (spalled or knocked out) with various energies.[49] Rather than using a monochromator to select a wavelength, a packet of the neutrons is used consisting of many wavelengths, and therefore energies and speeds. As the packet leaves the target towards the diffractometer the neutrons will spread out as a function of their velocities (the faster neutrons will arrive at the sample before the slower neutrons). Therefore the resolution depends on the path length. The longer the path length, the more time the neutrons will have to spread out, and the higher the resolution will be. The compromise to this is that as the path length increases the flux decreases, and longer counting times are necessary. Because all the distances are known (target to sample, and sample to detector) and the time-of-flight can easily be measured the relationship between d-spacing and time-of-flight can be calculated (eq. 1.12), using Bragg's law (eq. 1.4) and the de Broglie relationship (eq. 1.11).[60]

$$\lambda = {ht}/{m_n L} \qquad \text{(eq. 1. 11)}$$

$$t = {m_n L 2 d sin\theta}/{h} \qquad \text{(eq. 1. 12)}$$

where: h is Planck's constant, m_n is the mass of a neutron, L is the total flight path, t is the time-of-flight, and θ is the angular detector position. In this type of neutron diffraction, the detectors are fixed at a known angle, the flight path is known, and the starting time of the neutron packet (or pulse) is known. Therefore, each time a neutron arrives at the detector the time is registered. Each detector receives a full diffractogram with every pulse, which is combined in order to give the final diffractogram, often reported with intensity on the y-axis and time-of-flight or d-spacing on the x-

axis. The peak flux found in spallation sources is typically higher than that of reactor sources, but the peak shapes of spallation diffractograms are much more difficult to model.

Examples of spallation neutron sources include the Spallation Neutron Source (SNS), at Oak Ridge National Lab (ORNL), Oak Ridge, TN, USA and ISIS, at the Science & Technology Facilities Council (STFC) Rutherford Appleton Laboratory, Didcot Oxford, UK. This thesis includes data collected from POWGEN (BL-11A), and NOMAD (BL1A) found at the SNS.

POWGEN is a high resolution general purpose diffractometer, which has a good balance of flux and resolution. As is shown in figure 1.15, it has a 60 m flight path from the liquid H_2 moderator to the sample and a series of choppers along the path to control the wavelength bandwidth. The initial chopper (T_0 chopper) cuts out the high energy neutrons which would increase the background, reducing the quality of data. Three other choppers along the beam path set the incident wavelength bandwidth and center wavelengths used throughout the experiment. These choppers prevent what is known as frame-overlap, where the fast neutrons from one pulse catch up to slow neutrons of the previous pulse. Typically, all pulses available at the SNS (60 Hz) are used for the experiments, however, the choppers can be used to eliminate pulses reducing the pulse frequency to 30, 20 or 10 Hz. This would allow for a wider wavelength bandwidth, at the expense of flux. The POWGEN instrument contains 40 detectors which are found around the sample at distances of 2.5 – 4.5 m. Data from all detectors are combined into a single dataset which cover the full range of d-spacings available. It is important to understand that different sections of the diffractogram are obtained from different detectors, and resolution differs between the detectors based on their positions. Therefore, it may be wise to analyze detectors in different groups, or omit them from the final diffractogram in order to gain better resolution at the expense of flux. Figure 1.15(ii) shows the detector layout for 2017. The resolution is best for the detectors in the plane of

the sample (detectors labelled 2). The shaded detectors are often omitted in order to increase resolution.

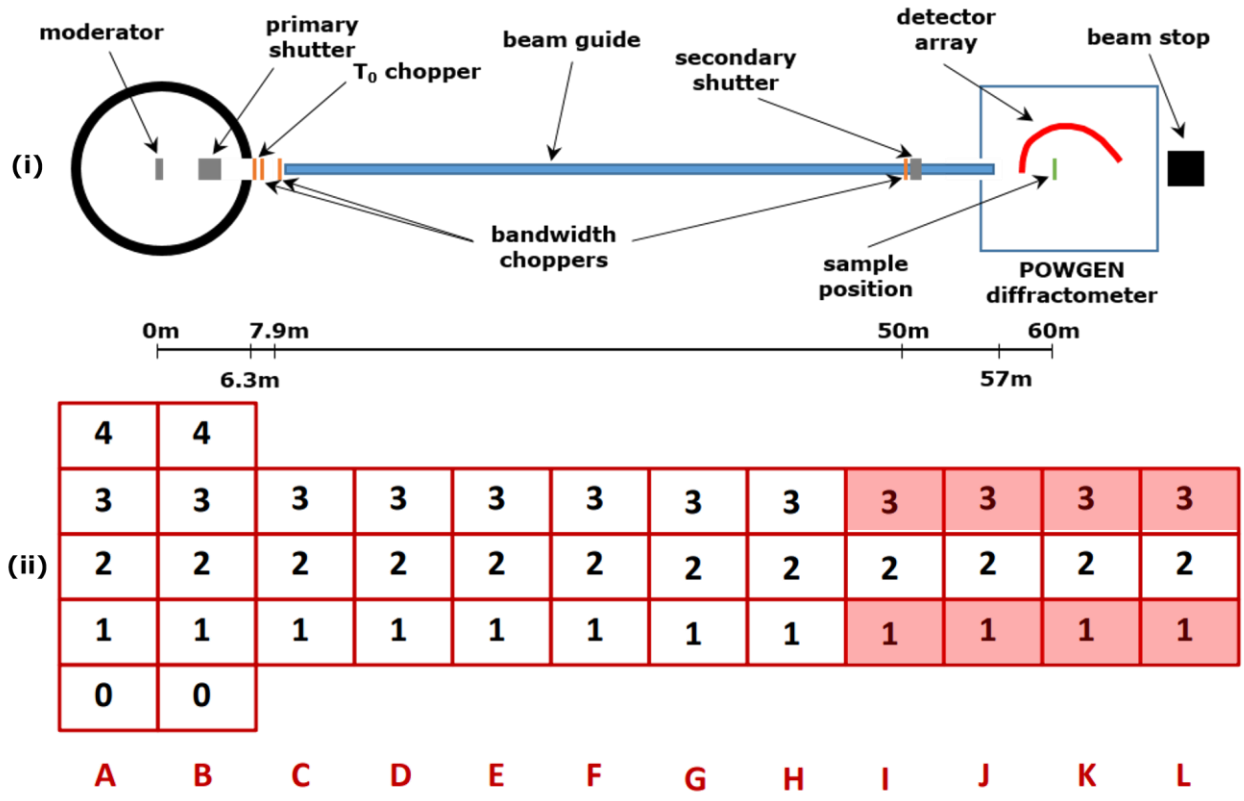

Figure 1.15: (i) Schematic of the POWGEN beamline annotated with the major components. (ii) Detector bank (as of 2017) showing the 40 detectors used for the POWGEN diffractometer. The shaded detectors are often omitted to increase resolution.

NOMAD is a high-flux, medium resolution time-of-flight neutron diffractometer which allows for the study of a variety of samples including liquids, glasses, polymers, nanocrystalline, and long-range ordered crystalline materials. NOMAD uses a liquid H_2 moderator, and with a moderator-to-sample distance of 19.5 m, this instrument boasts high flux allowing for small samples (100's of mgs) to be measured in typical neutron diffraction sample times (~1 hour). Furthermore, typical neutron sized samples (g-range) can be measured in minutes. This high flux

coupled with large angular detector coverage (3 – 175°), allows for small sample sizes, high-resolution pair distribution function analysis, and parametric studies. Neutrons from 0.1 – 3 Å are used for diffraction, limited by the fast neutrons from the next pulse. ^{3}He position sensitive detector tubes are arranged into groups of 8. Multiple 8-packs are used at the same angle to form banks. There are 6 detector banks arranged as shown in figure 1.16. Banks 1 and 6 use ½" detector tubes arranged into flat panels and are found at 2θ = 7° (bank 1) and 2θ = 154° (bank 6). All others use 1" detector tubes covering cylinder surfaces parallel to the beam.[61] Banks 2, 3, 4, and 5 are found at 2θ = 15°, 31°, 67°, and 122°, respectively.

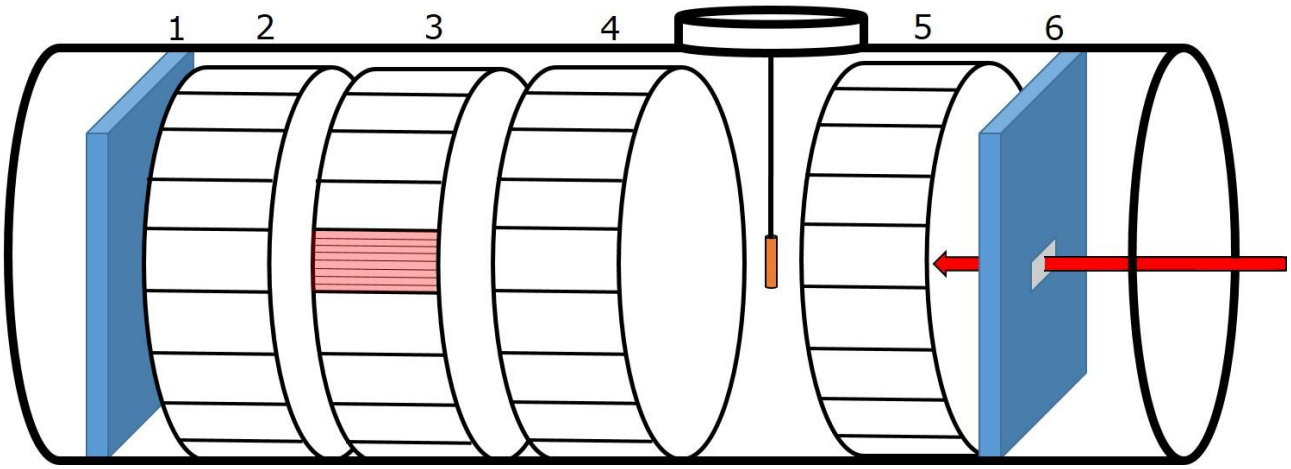

Figure 1.16: Schematic view of the detector arrangement around the NOMAD sample position. The neutron direction is indicated with a red arrow and the sample position is indicated with an orange cylinder. The figure is annotated with the bank numbers. Flat detector panels,1 (7 °) and 6 (154 °) are shown in blue. Banks 2 (15 °), 3 (31 °), 4 (67 °), and 5 (122 °) are shown as cylinders with panels which support 8-packs. The red shaded panel shows an illustration of an 8-pack in place.

1.4.1.4. In-situ Diffraction

Collecting diffraction data at elevated temperatures is becoming more and more common in the field of solid-state chemistry. The ability to analyze the structures of materials at elevated temperatures allows for the study of solid-state reactions, providing insight into mechanistic details

which are otherwise difficult to deduce. Furthermore, it allows for precision in transition temperatures, and the exploration of unquenchable or metastable phases. *In-situ* diffraction also allows materials with high temperature applications to be studied at their operating temperatures.

Typically, in-situ data is reported either as stacked plots, surface plots, or contour plots. In this thesis, *in-situ* high temperature powder diffraction experiments were carried out using laboratory X-ray instruments, synchrotron X-ray instruments, and neutron diffractometers.

Using the PANalytical X'Pert Pro diffractometer described in section 1.4.1.2.2, with an Anton Paar HTK2000 high temperature camera equipped with a platinum strip heater allows for measuring diffractograms at temperatures up to 1300 °C. The temperature of this furnace is accurate within ±5 °C at all temperatures. Samples are ground, and mounted directly on the platinum strip as thin layers using an acetone slurry. Sample height is adjusted with respect to room temperature data collected on the sample spinner stage. Figure 1.17 shows pictures of the HTK2000 furnace mounted on the diffractometer, both with its cover on and off. With this experimental set-up the temperature is increased (or decreased) in steps and diffraction data are collected at each temperature. Furthermore, different gases can be introduced into the furnace in order to study the effect of atmosphere while heating. This is particularly useful in studying oxidation using air or oxygen gas, reduction using carbon monoxide or hydrogen gas, and inert gases such as helium or nitrogen. Temperature increments, data acquisition times, beam optics, and atmospheric conditions are reported for each individual experiment in their respective chapters.

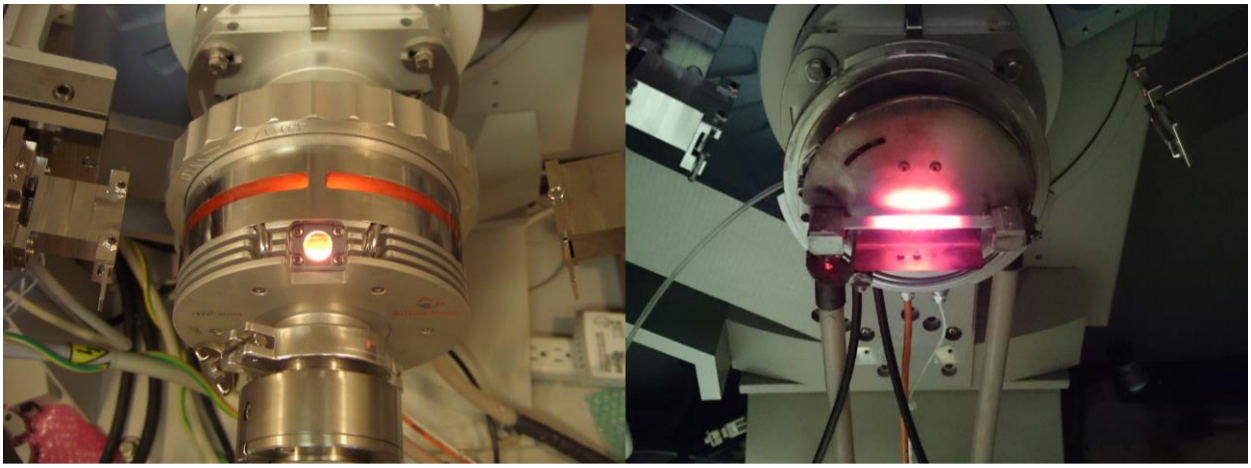

Figure 1.17: Pictures of the HTK2000 high-temperature furnace equipped with a Pt-strip heating element mounted to the PANalytical X'Pert Pro. Pictures are taken at elevated temperature (~1000 °C) with the cover on (left) and off (right).

In-situ synchrotron powder X-ray diffraction experiments were carried out at 17-BM-B at the APS. For these experiments, a Chupas flow-cell/furnace was used,[62] where Kanthal wire is coiled around a ceramic tube and power is provided to the resistive heaters by a DC power supply. Samples are loaded into a quartz capillary and plugged using quartz wool. A thermocouple is inserted near to the sample as shown in figure 1.18c and the X-rays are aligned near to the thermocouple to ensure maximum temperature accuracy. In order to increase powder averaging, the flow-cell is rocked during data collection. Using this experimental set-up, samples are heated continuously, and diffraction data is collected during this ramp. Data collection times and heating ramp rates vary based on the particular experiment and are reported where used. Typically Kanthal heating elements are able to reach temperatures around 1000 °C before breaking.

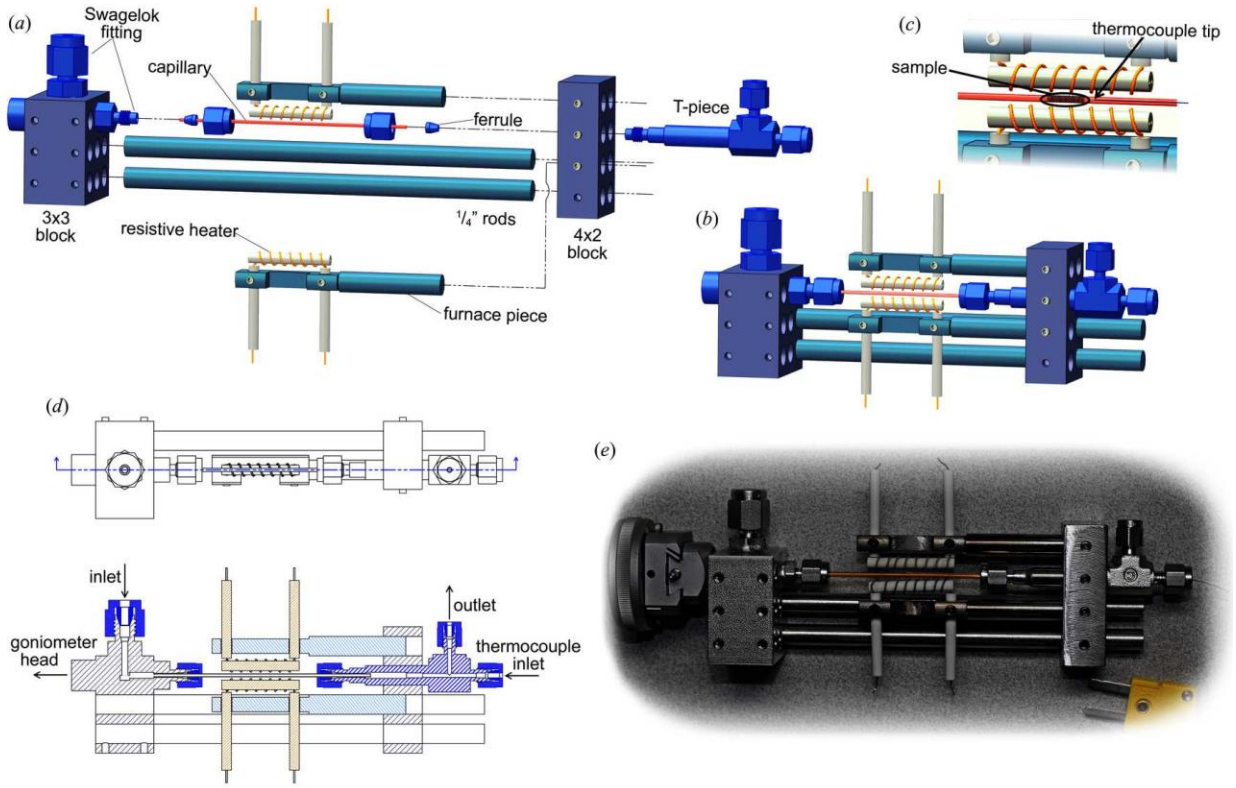

Figure 1.18 (*a*) An `exploded' representation of the flow-cell/furnace components, indicating how they fit together; (*b*) the fully assembled flow-cell/furnace; (*c*) an expanded view of the sample region, indicating the relative position of the sample and thermocouple tip within the furnace hot zone; (*d*) a top view of the flow-cell/furnace, with a corresponding cross section through the sample plane showing the gas/fluid path; (*e*) a photograph of the flow-cell/furnace mounted in a goniometer head. Heat shields have been omitted for clarity. Reproduced with permission of the International Union of Crystallography.[62]

Neutron *in-situ* diffraction experiments at the POWGEN diffractometer (SNS) used a traditional ILL furnace built with vanadium heating elements which allows for heating up to 1200 °C. The furnace was modified to have a vanadium window in order to allow penetration of the beam. The vacuum level of the ILL furnace is kept at approximately 2 x 10^{-5} torr throughout the experiment. Approximately 1 gram of sample is loaded into an ILL furnace vanadium sample can and mounted on to a sample stick. The sample stick is lowered into the furnace which is aligned to the height of the neutron beam. Heating is ramped up continuously throughout the experiment, while data are being collected by all detectors simultaneously. Data is binned post experiment using the

MANTID software[63] which allows for data binning based on time, temperature, or a number of other experimental details. Ramp rates and binning conditions are mentioned in individual chapters.

1.4.1.5. Data Analysis

A lot of effort is put into obtaining good diffraction data for any material synthesized; however, good data is only the first step in understanding the structure. Without good analysis techniques, the quality of data is essentially meaningless. There are many ways to analyze diffraction data; simple matching to a database, Le Bail fits, Pawley fits, pair distribution function (PDF) analysis, and the Rietveld method are a few of these techniques. In this section we will discuss in detail the Rietveld method, which was the method used for final analysis of all materials in this thesis.

1.4.1.5.1. Rietveld Method

The Rietveld method is the method of choice for the analysis of powder diffraction data. It is named after Hugo M. Rietveld who developed and first applied the method on neutron powder diffraction data.[64,65] Using the Rietveld method, parameters describing the crystal structure are refined by fitting a simulated diffractogram to a measured one. In this method, a simulated pattern is generated, based on a crystallographic structure model, and compared at each point with the collected pattern. The parameters describing the structure are then tweaked and once again compared to the experimental data. The best fit is found using a least squares minimization of the residual[66]

$$M = \sum_{i=1}^{N} w_i [y_i(obs.) - y_i(calc.)]^2 \qquad \text{(eq. 1. 13)}$$

where: y_i(obs.) is the measured intensity at point i in the diffractogram, y_i(calc.) is the calculated intensity, and w_i is the weight where

$$w_i = \frac{1}{y_i(obs.)} \quad \text{(eq. 1. 14)}$$

and the sum is over all the data points (N) in the diffractogram.[67] In order to successfully model the crystal structure of the sample, refinement of instrumental and sample dependent parameters is necessary (note: some parameters may have both a sample and instrumental contribution). Parameters can also be divided into those which are refined for each phase, and global parameters. Some examples of global parameters include: zero point (instrumental), asymmetry (instrumental), background (both), absorption (both), and specimen displacement (instrumental). Structural parameters which are refined for each phase include: scale factor, lattice parameters, preferred orientation, crystallite size and strain, positional coordinates, thermal parameters, and occupancies for each symmetry-equivalent site in the unit cell. This is by no means an exhaustive list of parameters, nor are all parameters listed refinable in each Rietveld refinement. Understanding these parameters is important in order to ensure that they make both chemical and physical sense. This is especially important when Rietveld refinements are performed on multiple diffractograms simultaneously. When completing simultaneous multi-histogram refinements, instrumental parameters for each instrument must be refined individually, while the structural parameters must be constrained to be the same.

Typically, many Bragg reflections contribute to the calculated intensity y_i(calc.) at any given point, i, in the calculated pattern. The calculated intensity at each point is determined by the structure factor, $|F_{hkl}|^2$, and modified by other parameters; summing the contribution of each reflection within range (this range is set by the user). This calculated intensity is given by:[66]

$$y_i(calc.) = s\sum_{hkl} L_{hkl}|F_{hkl}|^2 \phi P_{hkl} A + y_{bi} \quad \text{(eq. 1. 15)}$$

where:

s is the scale factor;

L_{hkl} is a term which contains the Lorentz, polarization, and multiplicity factors;

Φ is the profile function, which describes the peak shape;

P_{hkl} is the preferred orientation of the crystals;

A is an absorption factor, which depending on instrument geometry may or may not be constant; and

y_{bi} is the background intensity at the i^{th} step.

There are many different criteria of fit used to estimate the agreement between the calculated and measured diffractograms. However, care must be taken in order to ensure that the values received for each parameter are both physically possible and make chemical sense. Some common criteria of fit include:

profile R factor,

$$R_P = \frac{\sum_i |y_i(obs.) - y_i(calc.)|}{\sum_i y_i(obs.)}; \quad \text{(eq. 1. 16)}$$

weighted profile R factor,

$$R_{wP} = \sqrt{\left[\frac{\sum_i w_i |y_i(obs.) - y_i(calc.)|^2}{\sum_i w_i y_i^2(obs.)}\right]}; \quad \text{(eq. 1. 17)}$$

Bragg R factor,

$$R_B = \frac{\sum_k |I_k(obs.) - I_k(calc.)|}{\sum_k I_k(obs.)}; \quad \text{(eq. 1. 18)}$$

expected R factor,

$$R_E = \sqrt{\left[\frac{N-P}{\sum_i w_i y_i^2(obs.)}\right]}; \text{ and} \quad \text{(eq. 1. 19)}$$

goodness of fit,

$$\chi^2 = \frac{R_{WP}}{R_E} \ . \qquad \text{(eq. 1. 20)}$$

I_k is the integrated intensity of the k^{th} reflection, N is the number of data points, and P is the number of refined parameters.[67] It is noted that R_B is somewhat biased in favor of the model due to the use of integrated intensities deduced by the model rather than each data point individually. However, it is the R-factor that is most comparable to the conventional R-values used for single-crystal refinements and depends only on the structural parameters, not the profile parameters.[66] The R_{wP} is arguably the most meaningful of the R's due to its similarity to (eq. 1.13) which is the residual being minimized. The quality of the fit is most often reported using χ^2, which correlates R_{wP} and R_E and should therefore approach unity. It is important to note, however, that some characteristics of the data (background, signal to noise, etc.) can affect the values of some of these factors. For that reason, all of these factors, as well as the difference plot and chemical intuition all need to be used for successful Rietveld refinements. A comprehensive guideline for structure refinements using the Rietveld method has been formulated by the International Union of Crystallography on Powder Diffraction, and is an invaluable tool for all scientists who must conduct Rietveld refinements for their research.[68]

There are many programs which allow for the refinement of crystal structures from diffraction data. The two programs that were used in this thesis are FullProf.2k[69] and TOPAS-Academic Version 5.[70]

1.4.2. Thermal Analysis

Characterizing materials using thermal analysis techniques is beneficial for understanding their high temperature structures and properties. It allows researchers to understand solid-state

reactions, phase transitions, and decompositions. The three main techniques in thermal analysis include thermogravimetric analysis (TGA), differential scanning calorimetry (DSC), and differential thermal analysis (DTA).[10] Many modern instruments allow for these techniques to be measured simultaneously.

1.4.2.1. Thermogravimetric Analysis (TGA)

TGA is a fairly straightforward technique where the mass of a sample is monitored as a function of time, temperature, or both. Typically, the sample is heated at a constant rate in a controlled atmosphere and the mass change can be used to quantitatively calculate compositional changes. For example, samples can be heated in flowing oxygen in order to monitor oxidation. As the sample is oxidized a gain in mass will be seen due to the oxygen uptake of the sample. Typical sample sizes are in 10's to 100's of mg, and typical plots are mass vs. temperature; however, mass vs. time plots are also sometimes reported.

1.4.2.2. Differential Thermal Analysis (DTA)

In DTA the temperature of a sample and a reference (often an empty sample holder is used) are both monitored throughout the experiment. A constant heating (or cooling) rate is applied, and the same power is input to both the sample and the reference. The temperature difference between the sample and the reference is measured and reported (either in °C or in μV). The difference is plotted against the temperature inside the furnace, often of the heating block. If the heat capacities are the same, the result will be a flat line, while any differences will result in peaks. The qualitative analysis of the resulting peaks allow for the determination of the temperature of the transition and whether it is exothermic or endothermic.

1.4.2.3. Differential Scanning Calorimetry (DSC)

DSC is similar to DTA in that it is also a differential technique, measuring both a sample and a reference as they are heated at a constant rate. There are two main types of DSC instruments, heat flux DSC, and power compensated DSC. In a power compensated DSC the power applied to the sample and reference in order to keep them heating (or cooling) at the same rate is measured. In a heat flux DSC the temperature of the sample and reference are allowed to vary and the difference in heat flow is measured. Typically, reported plots are heat flow vs. temperature. The main advantage to using DSC is that measuring the heat flow between the reference and the sample allows for quantitative analysis, resulting in the calculation of enthalpies of transitions.

1.4.2.4. Linseis Thermowage L81/1550 Thermal Balance

Throughout this thesis, a Linesis Thermowage L81/1550 thermal balance (Linseis Messgeraete GmbH, Selb, Germany) in vertical measurement mode was used for TGA measurements. A schematic of this balance can be seen in figure 1.19. A compensation weighing system is used, where electromagnets on each side of the fulcrum keep all components stationary during the

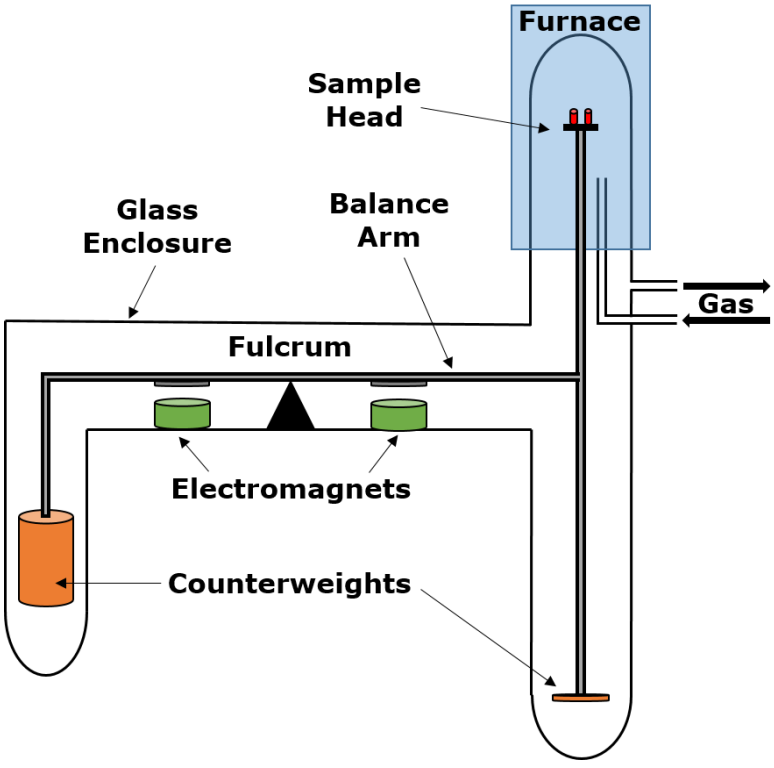

Figure 1.19: Schematic of the Linseis L81 Thermal Balance

measurement. The current applied to the electromagnets is converted to mass change. The top loading thermobalance is loaded with 50 – 100 mg of sample in alumina crucibles (shown in red). Typical measurements were carried out with a heating rate of 10 °C/min under oxidative or reducing atmospheres. All experiments were corrected for buoyancy and used an empty alumina crucible as a reference. X-ray diffraction was used to identify the products of all measurements. Specific details of the experimental setups can be found in each of the individual chapters.

References

(1) DiSalvo, F. J. Solid-State Chemistry: A Rediscovered Chemical Frontier. *Science* **1990**, *247* (4943), 649–655.

(2) Parkinson, B. The Emerging Art of Solid-State Synthesis. *Science* **1995**, *270* (5239), 1157–1158.

(3) Sanjaya Ranmohotti, K. G.; Josepha, E.; Choi, J.; Zhang, J.; Wiley, J. B. Topochemical Manipulation of Perovskites: Low-Temperature Reaction Strategies for Directing Structure and Properties. *Adv. Mater.* **2011**, *23* (4), 442–460.

(4) Stein, A.; Keller, S. W.; Mallouk, T. E. Turning Down the Heat: Design and Mechanism in Solid-State Synthesis. *Science* **1993**, *259* (5101), 1558–1564.

(5) Danks, A. E.; Hall, S. R.; Schnepp, Z. The Evolution of "sol–gel" Chemistry as a Technique for Materials Synthesis. *Mater. Horiz.* **2016**, *3* (2), 91–112.

(6) Hench, L. L.; West, J. K. The Sol-Gel Process. *Chem. Rev.* **1990**, *90* (1), 33–72.

(7) Kitchen, H. J.; Vallance, S. R.; Kennedy, J. L.; Tapia-Ruiz, N.; Carassiti, L.; Harrison, A.; Whittaker, A. G.; Drysdale, T. D.; Kingman, S. W.; Gregory, D. H. Modern Microwave Methods in Solid-State Inorganic Materials Chemistry: From Fundamentals to Manufacturing. *Chem. Rev.* **2014**, *114* (2), 1170–1206.

(8) Rabenau, A. The Role of Hydrothermal Synthesis in Preparative Chemistry. *Angew. Chem., Int. Ed.* **1985**, *24* (12), 1026–1040.

(9) Feng, S.; Xu, R. New Materials in Hydrothermal Synthesis. *Acc. Chem. Res.* **2001**, *34* (3), 239–247.

(10) White, M. A. *Properties of Materials*; Oxford University Press: New York, New York,

USA, 1999.

(11) *CRC Handbook of Chemistry and Physics: Special Student Edition*, 77th Ed.; Lide, D. R., Ed.; CRC Press, 1996.

(12) Schneider, S. J. *Compilation of the Melting Points of the Metal Oxides*; National Bureau of Standards, 1963.

(13) Lussier, J. A.; Shafi, S. P.; Donaberger, R. L.; Bieringer, M. Platinum Uptake and Ba_2CePtO_6 Formation during in Situ $BaCe_{(1-x)}M_{(x)}O_{(3-\delta)}$ (M = La, In) Formation. *Inorg. Chem.* **2014**, *53* (16), 8809–8815.

(14) Zayat, M.; Levy, D. Blue $CoAl_2O_4$ Particles Prepared by the Sol-Gel and Citrate-Gel Methods. *Chem. Mater.* **2000**, *12* (9), 2763–2769.

(15) Lotgering, F. K. Topotactical Reactions with Ferrimagnetic Oxides Having Hexagonal Crystal Structures. *J. Inorg. Nucl. Chem.* **1959**, *9* (2), 113–123.

(16) Tassel, C.; Kageyama, H. Square Planar Coordinate Iron Oxides. *Chem. Soc. Rev.* **2012**, *41* (6), 2025–2035.

(17) Rudorff, W. Inclusion of Base Metals in Graphite and in Metallic Chalcogenides of the Type MeX_2. *Chimia (Aarau).* **1965**, *19*, 489–499.

(18) Perejon, A.; Hayward, M. A. Reductive Lithium Insertion into B-Cation Deficient Niobium Perovskite Oxides. *Dalton Trans.* **2015**, *44* (23), 10636–10643.

(19) Kobayashi, Y.; Hernandez, O. J.; Sakaguchi, T.; Yajima, T.; Roisnel, T.; Tsujimoto, Y.; Morita, M.; Noda, Y.; Mogami, Y.; Kitada, A.; et al. An Oxyhydride of $BaTiO_3$ Exhibiting Hydride Exchange and Electronic Conductivity. *Nat. Mater.* **2012**, *11* (6), 507–511.

(20) Yajima, T.; Takeiri, F.; Aidzu, K.; Akamatsu, H.; Fujita, K.; Yoshimune, W.; Ohkura, M.;

Lei, S.; Gopalan, V.; Tanaka, K.; et al. A Labile Hydride Strategy for the Synthesis of Heavily Nitridized $BaTiO_3$. *Nat. Chem.* **2015**, *7* (12), 1017–1023.

(21) Clemens, O.; Slater, P. R. Topochemical Modifications of Mixed Metal Oxide Compounds by Low-Temperature Fluorination Routes. *Rev. Inorg. Chem.* **2013**, *33*, 105–117.

(22) Tsujimoto, Y.; Yamaura, K.; Hayashi, N.; Kodama, K.; Igawa, N.; Matsushita, Y.; Katsuya, Y.; Shirako, Y.; Akaogi, M.; Takayama-Muromachi, E. Topotactic Synthesis and Crystal Structure of a Highly Fluorinated Ruddlesden-Popper-Type Iron Oxide, $Sr_3Fe_2O_{5+x}F_{2-X}$ (X ~ 0.44). *Chem. Mater.* **2011**, *23* (16), 3652–3658.

(23) Tsujimoto, Y.; Tassel, C.; Hayashi, N.; Watanabe, T.; Kageyama, H.; Yoshimura, K.; Takano, M.; Ceretti, M.; Ritter, C.; Paulus, W. Infinite-Layer Iron Oxide with a Square-Planar Coordination. *Nature* **2007**, *450* (7172), 1062–1065.

(24) Hayward, M. A.; Rosseinsky, M. J. Anion Vacancy Distribution and Magnetism in the New Reduced Layered Co(II)/Co(I) Phase $LaSrCoO_{(3.5-X)}$. *Chem. Mater.* **2000**, *12* (8), 2182–2195.

(25) Hayward, M. A.; Green, M. A.; Rosseinsky, M. J.; Sloan, J. Sodium Hydride as a Powerful Reducing Agent for Topotactic Oxide Deintercalation: Synthesis and Characterization of the nickel(I) Oxide $LaNiO_2$. *J. Am. Chem. Soc.* **1999**, *121* (38), 8843–8854.

(26) Hayward, M. A. The Hydride Anion in an Extended Transition Metal Oxide Array: $LaSrCoO_3H_{0.7}$. *Science* **2002**, *295* (5561), 1882–1884.

(27) Tsujimoto, Y.; Tassel, C.; Hayashi, N.; Watanabe, T.; Kageyama, H.; Yoshimura, K.; Takano, M.; Ceretti, M.; Ritter, C.; Paulus, W. Infinite-Layer Iron Oxide with a Square-

Planar Coordination. *Nature (London, U.K.)* **2007**, *450* (7172), 1062–1065.

(28) Kageyama, H.; Watanabe, T.; Tsujimoto, Y.; Kitada, A.; Sumida, Y.; Kanamori, K.; Yoshimura, K.; Hayashi, N.; Muranaka, S.; Takano, M.; et al. Spin-Ladder Iron Oxide: $Sr_3Fe_2O_5$. *Angew. Chem., Int. Ed.* **2008**, *47* (31), 5740–5745.

(29) Hernden, B. C.; Lussier, J. A.; Bieringer, M. Topotactic Solid-State Metal Hydride Reductions of Sr_2MnO_4. *Inorg. Chem.* **2015**, *54* (9), 4249–4256.

(30) Schaak, R. E.; Mallouk, T. E. Perovskites by Design: A Toolbox of Solid-State Reactions. *Chem. Mater.* **2002**, *14* (4), 1455–1471.

(31) Nguyen, S. D.; Kim, S. H.; Halasyamani, P. S. Synthesis, Characterization, and Structure-Property Relationships in Two New Polar Oxides: $Zn_2(MoO_4)(SeO_3)$ and $Zn_2(MoO_4)(TeO_3)$. *Inorg. Chem.* **2011**, *50* (11), 5215–5222.

(32) Tan, G.; Zhao, L. D.; Kanatzidis, M. G. Rationally Designing High-Performance Bulk Thermoelectric Materials. *Chem. Rev.* **2016**, *116* (19), 12123–12149.

(33) Finch, R. J. Structure and Chemistry of Zircon and Zircon-Group Minerals. *Rev. Mineral. Geochem.* **2003**, *53* (1), 1–25.

(34) Zhang, H.-S.; Kang, F.; Zhao, Y.-J.; Peng, M.; Lei, D. Y.; Yang, X.-B. The Role of Oxygen Defects in a Bismuth Doped $ScVO_4$ Matrix: Tuning Luminescence by Hydrogen Treatment. *J. Mater. Chem. C* **2017**, *5* (2), 314–321.

(35) Garg, A. B.; Errandonea, D.; Rodríguez-Hernández, P.; Muñoz, A. $ScVO_4$ under Non-Hydrostatic Compression: A New Metastable Polymorph. *J. Phys.: Condens. Matter* **2017**, *29* (5), 55401.

(36) Chi, F.; Qin, Y.; Hu, F.; Wei, X.; Chen, Y.; Duan, C.; Yin, M. Efficient Red-Emitting Phosphor $ScVO_4$ Doped with Bi^{3+} and Eu^{3+} for near-Ultraviolet-Activated Solid-State

Lighting. *J. Mater. Sci.* **2017**, *52*.

(37) Cong, H.; Zhang, H.; Yao, B.; Yu, W.; Zhao, X.; Wang, J.; Zhang, G. $ScVO_4$: Explorations of Novel Crystalline Inorganic Optical Materials in Rare-Earth Orthovanadate Systems. *Cryst. Growth Des.* **2010**, *10* (10), 4389–4400.

(38) *World Energy Outlook 2017*; 2017.

(39) S. C. Singhal. Solid Oxide Fuel Cells: An Overview,. *Prepr. Pap.-Am. Chem. Soc., Div. Fuel Chem.* **2004**, *49* (2), 478–479.

(40) Mahato, N.; Banerjee, A.; Gupta, A.; Omar, S.; Balani, K. Progress in Material Selection for Solid Oxide Fuel Cell Technology: A Review. *Prog. Mater. Sci.* **2015**, *72*, 141–337.

(41) Bove, R. Solid Oxide Fuel Cells: Principles, Designs and State-of-the-Art in Industries BT - Recent Trends in Fuel Cell Science and Technology; Basu, S., Ed.; Springer New York: New York, NY, 2007; pp 267–285.

(42) Basu, R. N. Materials for Solid Oxide Fuel Cells BT - Recent Trends in Fuel Cell Science and Technology; Basu, S., Ed.; Springer New York: New York, NY, 2007; pp 286–331.

(43) Skinner, S. J.; Kilner, J. A. Oxygen Ion Conductors. *Mater. Today* **2003**, *6* (3), 30–37.

(44) Goodenough, J. B. Oxide-Ion Electrolytes. *Annu. Rev. Mater. Res.* **2003**, *33* (1), 91–128.

(45) Goodenough, J. B. Ceramic Technology: Oxide-Ion Conductors by Design. *Nature* **2000**, *404* (6780), 821–823.

(46) Kilner, J. A. Fast Oxygen Transport in Acceptor Doped Oxides. *Solid State Ionics* **2000**, *129* (1), 13–23.

(47) Butler, V.; Catlow, C. R. A.; Fender, B. E. F.; Harding, J. H. Dopant Ion Radius and Ionic Conductivity in Cerium Dioxide. *Solid State Ionics* **1983**, *8* (2), 109–113.

(48) Minervini, L. Defect Cluster Formation in M_2O_3-Doped CeO_2. *Solid State Ionics* **1999**,

116 (3–4), 339–349.

(49) Pecharsky, V.; Zavalij, P. *Fundamentals of Powder Diffraction and Structural Characterization of Materials, Second Edition*; Springer Science + Business Media Inc., 2005.

(50) Cromer, D. T.; Mann, J. B. X-ray Scattering Factors Computed from Numerical Hartree–Fock Wave Functions. *Acta Crystallogr. Sect. A* **1968**, *24* (2), 321–324.

(51) Brown, P. J.; Fox, A. G.; Maslen, E. N.; O'Keefe, M. A.; Willis, B. T. M. Intensity of Diffracted Intensities. In *International Tables for Crystallography*; International Union of Crystallography: Chester, England, 2006; pp 554–595.

(52) Balerna, A.; Mobilio, S. *Synchrotron Radiation: Basics, Methods and Applications*; Mobilio, S., Boscherini, F., Meneghini, C., Eds.; Springer-Verlag, 2015.

(53) Wang, J.; Toby, B. H.; Lee, P. L.; Ribaud, L.; Antao, S. M.; Kurtz, C.; Ramanathan, M.; Von Dreele, R. B.; Beno, M. A. A Dedicated Powder Diffraction Beamline at the Advanced Photon Source: Commissioning and Early Operational Results. *Rev. Sci. Instrum.* **2008**, *79* (8), 1–7.

(54) Lee, P. L.; Shu, D.; Ramanathan, M.; Preissner, C.; Wang, J.; Beno, M. A.; Von Dreele, R. B.; Ribaud, L.; Kurtz, C.; Antao, S. M.; et al. A Twelve-Analyzer Detector System for High-Resolution Powder Diffraction. *J. Synchrotron Radiat.* **2008**, *15* (5), 427–432.

(55) Toby, B. H.; Huang, Y.; Dohan, D.; Carroll, D.; Jiao, X.; Ribaud, L.; Doebbler, J. A.; Suchomel, M. R.; Wang, J.; Preissner, C.; et al. Management of Metadata and Automation for Mail-in Measurements with the APS 11-BM High-Throughput, High-Resolution Synchrotron Powder Diffractometer. *J. Appl. Crystallogr.* **2009**, *42* (6), 990–993.

(56) Börner, H.; Brown, J.; Carlile, C. J.; Cubitt, R.; Currat, R.; Dianoux, A. J.; Farago, B.;

Hewat, A. W.; Kulda, J.; Lelièvre-Berna, E.; et al. *Neutron Data Booklet*, 2nd ed.; Old City Publishing: Philadelphia, PA, USA, 2003.

(57) Sears, V. F. Neutron Scattering Lengths and Cross Sections. *Neutron News* **1992**, *3* (3), 26–37.

(58) Rauch, H.; Waschkowski, W. 6 Neutron Scattering Lengths. In *Low Energy Neutrons and their Interaction with Nuclei and Matter. Part 1*; Schopper, H., Ed.; Springer-Verlag: Berlin/Heidelberg, 2000; pp 1–29.

(59) Koester, L.; Rauch, H.; Seymann, E. Neutron Scattering Lengths: A Survey of Experimental Data and Methods. *Atomic Data Nucl. Data Tables* **1991**, *49* (1), 65–120.

(60) Willis, B. T. M. Crystallography with a Pulsed Neutron Source. *Z. Kristallogr.* **1994**, *209* (5), 385.

(61) Neuefeind, J.; Feygenson, M.; Carruth, J.; Hoffmann, R.; Chipley, K. K. The Nanoscale Ordered MAterials Diffractometer NOMAD at the Spallation Neutron Source SNS. *Nucl. Instruments Methods Phys. Res. Sect. B* **2012**, *287*, 68–75.

(62) Chupas, P. J.; Chapman, K. W.; Kurtz, C.; Hanson, J. C.; Lee, P. L.; Grey, C. P. A Versatile Sample-Environment Cell for Non-Ambient X-Ray Scattering Experiments. *J. Appl. Crystallogr.* **2008**, *41* (4), 822–824.

(63) Arnold, O.; Bilheux, J. C.; Borreguero, J. M.; Buts, A.; Campbell, S. I.; Chapon, L.; Doucet, M.; Draper, N.; Ferraz Leal, R.; Gigg, M. A.; et al. Mantid — Data Analysis and Visualization Package for Neutron Scattering and μSR Experiments. *Nucl. Instruments Methods Phys. Res. Sect. A* **2014**, *764*, 156–166.

(64) Rietveld, H. M. Line Profiles of Neutron Powder-Diffraction Peaks for Structure Refinement. *Acta Crystallogr.* **1967**, *22* (1), 151–152.

(65) Rietveld, H. M. A Profile Refinement Method for Nuclear and Magnetic Structures. *J. Appl. Crystallogr.* **1969**, *2* (2), 65–71.

(66) Young, R. A. *The Rietveld Method*; Oxford University Press: New York, New York, USA, 1995.

(67) Albinati, A.; Willis, B. T. M. The Rietveld Method. In *International Tables for Crystallography*; International Union of Crystallography: Chester, England, 2006; pp 710–712.

(68) Mccusker, L. B.; Dreele, R. B. Von; Cox, D. E.; Loue È R D, D.; Scardi, P. Rietveld Refnement Guidelines. *J. Appl. Crystallogr.* **1999**, *32*, 36–50.

(69) Rodriguez-Carvajal, J. FullProf.2K. Full Prof 2K V. 4.40 2013.

(70) Coelho, A. A. TOPAS Academic. 2015.

Chapter 2. Order/Disorder and *in-situ* Oxide Defect Control in the Bixbyite Phase $YPrO_{3+\delta}$ ($0 \leq \delta < 0.5$)

Joey A. Lussier [a,b], Kevin M. Szkop [a,], Arzoo Z. Sharma [a,c], Christopher R. Wiebe [a,c,d,e] and Mario Bieringer [a,b]

[a] Department of Chemistry, University of Manitoba, Winnipeg, MB, R3T 2N2, Canada

[b] Manitoba Institute for Materials, University of Manitoba, Winnipeg, MB, R3T 2N2, Canada

[c] Department of Chemistry, University of Winnipeg, Winnipeg, MB, R3B 2E9, Canada

[d] Department of Physics and Astronomy, McMaster University, Hamilton, ON, L8S 4M1, Canada

[e] Canadian Institute for Advanced Research, Toronto, ON, M5G 1Z8, Canada

First Published in Inorganic Chemistry, 2016, 55, 2381 – 2389

DOI: 10.1021/acs.inorgchem.5b02746

Preface

This publication was the first of three articles written on the $Y_{2-x}Pr_xO_{3+\delta}$ system, a series of materials which has garnered some interest due to its implications on solid oxide fuel cell electrolyte materials. The article focuses on the 1:1 Y:Pr compound, where the importance of understanding synthesis to rationally design materials, and the order/disorder and defect control of these materials is discussed in detail. The structure of both the reduced and oxidized materials are reported, and a novel cation site-split model is presented. The manuscript was published by Inorganic Chemistry on February 15th, 2016.

Contributions

Joey A. Lussier and Kevin M. Szkop synthesized the samples used for this research. Arzoo Z. Sharma performed and analyzed the magnetic measurements, whereas all other measurements and analysis were completed by Joey A. Lussier. The manuscript was written by Joey A. Lussier and Mario Bieringer, with edits from all other authors.

2.1. Abstract

The $YPrO_{3+\delta}$ system is a nearly ideal model system for the investigation of oxide defect creation and annihilation in oxide ion conductor related phases with potential applications as solid-state electrolytes in solid oxide fuel cells. The formation, structure, high temperature reactivity, and magnetic susceptibility of phase pure $YPrO_{3+\delta}$ ($0 \leq \delta \leq 0.46$) are reported. The topotactic reduction and oxidation of the $YPrO_{3+\delta}$ system was investigated by powder X-ray *in-situ* diffraction experiments and revealed bixbyite structures (space group: *Ia*-3) throughout the series. Combined neutron and X-ray data clearly show oxygen uptake and removal. The research provides a detailed picture of the $Y^{3+}/Pr^{3+}/Pr^{4+}$ sublattice evolution in response to the redox chemistry. Upon oxidation cation site splitting is observed where the cation in the (*¼,¼.¼*) position migrates along the body diagonal to the (*x,x,x*) position. Any oxygen in excess of $YPrO_{3.0}$ is located in the additional *16c* site without depopulating the original *48e* site. The *in-situ* X-ray diffraction data and thermal gravimetric analysis have revealed the reversible topotactic redox reactivity at low temperatures (below 400 °C) for all compositions from $YPrO_3$ to $YPrO_{3.46}$. Magnetic susceptibility studies were utilized in order to further confirm praseodymium oxidation states. The linear relation between the cubic unit cell parameter and oxygen content allows for the straightforward determination of oxygen stoichiometry from X-ray diffraction data. The different synthesis strategies reported in this paper are rationalized with the structural details and the reactivity of $YPrO_{3+\delta}$ phases and provide guidelines for the targeted synthesis of these functional materials.

2.2. Introduction

The rich diversity of inorganic solid-state materials originates from the compositional and structural tunability of those phases. In addition to the composition and the underlying structure type, local structural features including anion and cation order/disorder as well as defect distributions control the properties of those extended phases. Reactivity studies provide guidance for the rational design of functional materials and choice of synthetic pathways by extending the structure–property relationships to structure-reactivity relationships. Oxide defect fluorite phases are commonly employed as oxide ion conductors. The close relation between the cubic bixbyite (c-Mn_2O_3) and fluorite (CaF_2) phases can illustrate the creation and annihilation of oxide defects during oxidation and reduction while the remainder of the structure adjusts to the evolving oxide sublattices. The mobility of oxide anions in defect fluorites highlights the structure property relation for oxide ion conductivity.[1] The fluorite structure crystallizes in space group *Fm*-3*m* (#225) and is based on a face-centered cubic (fcc) cation lattice (*4a* site) surrounded with anions located in the tetrahedral holes (*8c* site) resulting in cubic MX_8 coordination.[2] A schematic of the fluorite structure can be seen in figure 2.1. Fluorite phases can tolerate anion vacancies and thus give access to oxide defect phases of composition $MO_{2-\delta}$, known as defect fluorites.[3] These defect fluorites can be created via doping with lower valent cations (e.g. $Zr_{(1-x)}Y_xO_{2-\delta}$) where the oxide defect concentration is directly related to the dopant and its concentration. Alternatively a redox active cation in the fluorite structure permits to adjust the oxide defect concentrations. Because the reduction and oxidation can be followed by *in-situ* experiments, a deeper understanding of the creation and annihilation of oxide defects can be gained from this approach. Large concentrations

of fully disordered oxide defects can be accommodated in fluorite phases such as 12.5% defects in $ScVO_{3.5}$, $ScTiO_{3.5}$ and $InVO_{3.5}$.[4–6] Increasing the vacancy concentrations further causes oxide defect ordering. The resulting anion ordered cubic bixbyite structure (25% defects) is closely related to the anion disordered defect fluorite structure. Bixbyite phases crystallize in space group *Ia*-3 (#206) with the cations on the *8b* and *24d* sites and the anions occupy the general position *48e*.[7] The bixbyite structure is illustrated in figure 2.1. Notably the cation sublattices in the bixbyite and fluorite structures have the same topologies.[8] Consequently, topotactic reductions and oxidations provide straightforward reaction pathways. The structural similarities of the cation lattices are indicated in figure 2.1.

We are reporting the synthesis, reactivity, structural and magnetic characterization of $YPrO_{3+\delta}$ ($0 \leq \delta \leq 0.46$). For ABO_3 systems different cation and anion ordered and disordered structures can be realized including a diverse range of perovskites,[9–11] A-M_2O_3,[12] B-M_2O_3,[13,14] C-M_2O_3 (bixbyite),[9,15] and corundum,[16] among others. Ionic radii ratios often decide over the thermodynamically stable structure types and thus serve as a first guide for choosing

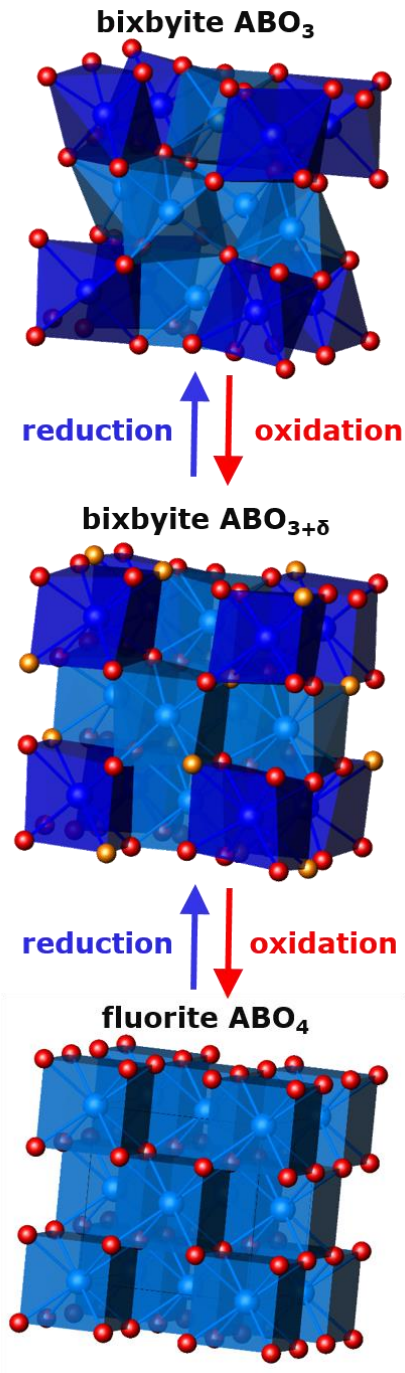

Figure 2.1 Illustration of the cubic bixbyite structure (space group: *Ia*-3) of $YPrO_3$ (top) and the topotactically oxidized product $YPrO_{3+\delta}$ (centre). Blue = Y/Pr sites (dark blue = *8b*, light blue = *24d* sites), red = oxygen (*48e* site), orange = oxygen/defects (*16c* site). The structure at the bottom illustrates the potentially fully oxidized fluorite structure. Blue = Y/Pr sites (*4a* site) and red = oxygen (*8c* site).

the appropriate ions.[17] For similar A and B radii an A/B cation disordered structure is expected. For the cations Y^{3+} and Pr^{3+} the bixbyite structure is expected with Y^{3+} and Pr^{3+} disordered on the *8b* and *24d* sites.

Previously, Kimmel et al.[18] reported that $YCeO_3$ and $YNdO_3$ form phase pure bixbyite structures, while the target material $YPrO_3$ was reported as a biphasic sample with preferential phase separation into an yttrium-rich bixbyite-like phase and a praseodymium-rich fluorite-like phase. This finding will be addressed with our results. Rajendran et al.[19] however, synthesized and reported electrical conductivity data for a phase pure 1:1 mixture of yttrium and praseodymium, $YPrO_{3.339}$.[20] No structural details were published and neutron diffraction studies were not utilized. Consequently oxygen positions could not be accurately determined.

The $YPrO_{3+\delta}$ system was chosen as a promising candidate for the systematic investigation of oxide defect creation and annihilation for ion conduction applications. The main objective of the present investigation is the synthesis and comprehensive characterization of phase-pure $YPrO_{3+\delta}$. Defects can be controlled by low temperature topotactic reductions and oxidations while maintaining the cation sublattices and avoiding potential phase separation.

Topotactic chemistry is utilized to access compounds that cannot be prepared by standard high-temperature methods. This technique entails low-temperature manipulations of host materials.[21] Because the cation lattice remains largely unchanged, and only anion sublattice manipulations are required, the bixbyite-fluorite system is an ideal candidate for topotactic reactions. Shafi et al. and Lundgren et al. have utilized topotactic reactions to shed light on the redox chemistry of similar bixbyite and fluorite systems, including scandium vanadates,[4] titanates,[5] and indium vanadates.[6] Controlling defect structures via defect concentrations and understanding the stability of these compounds is crucial for the rational design of reliable ion conducting materials. Our interest in

this system is prompted by the potential for new oxide ion conductor phases and a better understanding of the bixbyite-fluorite structure and reactivity relationships.

2.3. Experimental

2.3.1. Synthesis

Bulk samples of $YPrO_{3+\delta}$ were prepared using stoichiometric amounts of calcined Y_2O_3 (Cerac, 99.999% purity) and Pr_6O_{11} (Alfa Aesar, 99.996% purity). Starting materials were dissolved in conc. HNO_3 and slowly added to molten citric acid monohydrate (CA, Aldrich, 99% purity). The gel was decomposed on a hotplate and subsequently fired at 600 °C overnight. The resulting dark green powder was ground in an agate mortar and heated in air in an alumina crucible for 12 hours at 900 °C and 12 hours at 1200 °C with intermediate grinding. The brown powder was a pure bixbyite phase with composition $YPrO_{3+\delta}$.

$YPrO_{3+\delta}$ was reduced at 1000 ˚C in flowing hydrogen (5% H_2 in N_2) for 12 hours. The resulting beige $YPrO_3$ powder was a pure bixbyite phase.

2.3.2. Characterization

2.3.2.1. Laboratory Powder XRD at Room Temperature

Room temperature powder X-ray diffraction was collected using a PANalytical X'Pert Pro diffractometer in Bragg-Brentano geometry (PANalytical B.V., Almelo, the Netherlands) equipped with a Cu anode (λ ($K\alpha_1$) = 1.540598 Å, and λ ($K\alpha_2$) = 1.544426 Å). The measurements were carried out using a 1° divergence slit, 10 mm mask, 0.04 rad Soller slits, Ni filter and an X'Celerator detector with 128 microstrips covering a total 2θ range of 2.122°. Samples were

mounted as thin layers (cast as acetone slurries) on a zero background sample holder (Si (510)) and measured on a spinning sample stage (1 Hz). Data were collected with 0.0167° steps covering a 2θ range from 10° to 140° at 200 s/step counting time for Rietveld refinements. The diffractometer line profiles and peak positions were confirmed with NIST standards LaB_6 SRM 660a and Si SRM 640b, respectively.

2.3.2.2. Synchrotron Powder XRD at Room Temperature

Room temperature high resolution synchrotron diffraction data were collected using beamline 11-BM at the Advanced Photon Source (APS), Argonne National Laboratory in Argonne, Illinois. The instrument is described elsewhere.[22] A Kapton capillary (ø = 0.8 mm) plugged with wax was used as a sample holder, and data were collected with an average wavelength of 0.41385 Å out to 50˚ in 2θ in 0.001˚ steps using a scan rate of 0.01˚/s. A mixture of NIST standard reference materials, Si (SRM 640c) and Al_2O_3 (SRM 676) is used to calibrate the instrument.

2.3.2.3. Neutron Powder Diffraction

Preliminary neutron powder diffraction data were collected at two facilities. (1) $YPrO_{3+\delta}$ diffractograms were collected on the 800 wire medium resolution powder neutron diffractometer at C2, Canadian Neutron Beam Centre (CNBC) at the Chalk River Laboratories in Chalk River, Ontario. Room temperature data were collected in a cylindrical vanadium sample can using two detector settings and wavelengths covering a d-spacing range from d = 0.78 Å to 19.4 Å (λ_1 = 1.33 Å: $2\theta_1$ = 37°–117°; λ_2 = 2.37 Å: $2\theta_2$ = 7°–87°). (2) $YPrO_3$ data were collected on the POWGEN diffractometer, SNS at Oak Ridge National Laboratory in Oak Ridge, Tennessee. Approximately 0.7 grams of sample was loaded into an 8 mm diameter cylindrical vanadium sample can. Using a

frame with a 1.333 Å centre wavelength the d-spacing range from 0.41 Å to 5.37 Å was collected using a slit width of 20 mm and a slit height of 35 mm. Data were collected for approximately one hour.

2.3.3. High-Temperature in-situ Powder X-ray Diffraction

High temperature *in-situ* powder X-ray diffraction experiments were carried out using the same diffractometer described in section 2.3.2.1, where samples were mounted as an acetone slurry directly on a 10 mm platinum resistive strip heater within a self-masking Anton Paar HTK2000 furnace (Anton Paar GmbH). Between room temperature and 1200 °C the furnace is reliable within 5 °C. Variable temperature X-ray diffractograms were collected in increments of 25 °C from 25 °C to 1200 °C and during cooling in 25 °C decrements to room temperature. Data were collected with 0.0167° steps covering $18° \leq 2\theta \leq 72°$ with 100 s/step counting time for a total of 45 minutes at each temperature.

2.3.4. Thermogravimetric Analysis

Thermogravimetric analysis (TGA) was collected using a Linseis Thermowaage L 81/1550 Thermal Balance. Using a heating rate of 10 ˚C/min samples were heated to 1000 ˚C in flowing oxygen or flowing 5% H_2 - 95% N_2. All experiments were corrected for buoyancy and were conducted in alumina crucibles with an empty crucible as the reference. All products were identified using powder X-ray diffraction.

2.3.5. Rietveld Refinements

All Rietveld refinements were carried out using the *FullProf.2k*[23] software package. The crystallographic structures were refined simultaneously against powder synchrotron X-ray and time-of-flight neutron diffraction data. Up to 36 parameters were optimized including background coefficients, peak shapes and asymmetries, unit cell parameters, atomic positions, and temperature factors (both isotropic and anisotropic). The yttrium to praseodymium ratio was constrained to 1:1 for all refined structures allowing to freely distribute over the cation positions. Oxygen occupancies were fixed based on results from thermal gravimetric analysis. Oxygen positions, and occupancies of the two oxygen sites were refined only for samples where neutron powder diffraction was collected. All refinements based on laboratory powder X-ray (PANalytical) diffraction data only were completed by first fixing sample parameters based on synchrotron/neutron refinements in order to establish instrumental parameters, followed by fixing these established instrumental parameters in order to accurately and consistently analyze unit cell parameters and atomic position changes as a function of temperature (2.6) or oxygen content (2.7).

2.3.6. Magnetic Measurements

DC magnetic susceptibility measurements were carried out on 10 to 15 mg powder samples between 1.8 K and 400 K using the Vibrating Sample Magnetometer (VSM) option of a Dynacool Physical Property Measurement System (PPMS) from Quantum Design. The zero field cooled (ZFC) data were collected by heating in fine steps and stabilizing at each temperature up to 400 K in a magnetic field of 0.1 T after the sample was cooled in a zero field to 1.8 K. The field cooled (FC) data were obtained similarly after cooling the sample from room temperature to 1.8 K in a 0.1 T field. $YPrO_{3.00}$ was also measured from base temperature to 50 K in a 1 T field.

2.4. Synthesis and $YPrO_{3+\delta}$ Formation

The high temperature solid-state synthesis of $YPrO_{3+\delta}$ in oxidizing and reducing atmospheres did not result in single phase products. In contrast, the lower temperature sol-gel citric acid method resulted in a phase pure $YPrO_{3+\delta}$ bixbyite phase. Figure 2.2 compares the powder X-ray diffractograms of the final products of these three attempts. The reductive solid-state synthesis yielded a mixture of Pr_2O_3, Y_2O_3, and $Pr^{3+/4+}$ oxides. The lack of reactivity is rationalized with the limited mobility of the large Pr^{3+} (r(VI) = 0.99 Å) cation. Using an oxidative route with the smaller Pr^{4+} (r(VI) = 0.85 Å)[24] cation is more promising due to the increased ion mobility during the reaction. The oxidative solid-state synthesis yielded multiphasic products of poor crystallinity. The powder diffractogram (black pattern in figure 2.2) shows the presence of multiple bixbyite and/or fluorite phases suggesting incomplete cation mixing. Extended annealing did not improve the sample quality. At elevated temperatures Pr^{4+} reduction is observed in air and in addition sample decomposition is evident above 1200 ˚C. This effect will be elaborated upon and further discussed in section 2.6. It was therefore concluded that phase pure $YPrO_{3+\delta}$ is not accessible via traditional high temperature solid-state oxide reactions.

The red powder diffraction pattern in figure 2.2 describes the product of the citric acid sol-gel synthesis after annealing at 900 ˚C and 1200 ˚C in air. The product is highly crystalline (D > 1000 Å) single phase $YPrO_{3+\delta}$. All Bragg peaks indicated with red tick marks are consistent with the cubic bixbyite structure (space group: *Ia*-3). The oxygen stoichiometry was determined by thermal gravimetric analysis and revealed the composition $YPrO_{3.43(2)}$. Structural details will be discussed in section 2.5.2. Single phase $YPrO_{3+\delta}$ is already present after decomposition of the gel at 500 ˚C in air with typical crystalline domain sizes of approx. 70 Å. Figure 2.3 illustrates the temperature

dependent crystalline domain growth of the poorly crystalline $YPrO_{3+\delta}$ sol-gel product as investigated by *in-situ* powder X-ray diffraction. The contour plot shows the sharpening of the (222) peak with increasing temperature above 600 ˚C as illustrated with the decrease of the full width at half maximum (FWHM). Since the sample was processed at 600 ˚C (gel decomposition) prior to the *in-situ* experiment no variation of the FWHM is observed below that temperature. The initial amorphous $YPrO_{3+\delta}$ sample is assumed to form a nano-crystalline precursor during the initial gel decomposition below 600 °C. $YPrO_{3.43(2)}$ is the precursor for the fully reduced phase $YPrO_{3.00}$ which is discussed in section 2.5.1.

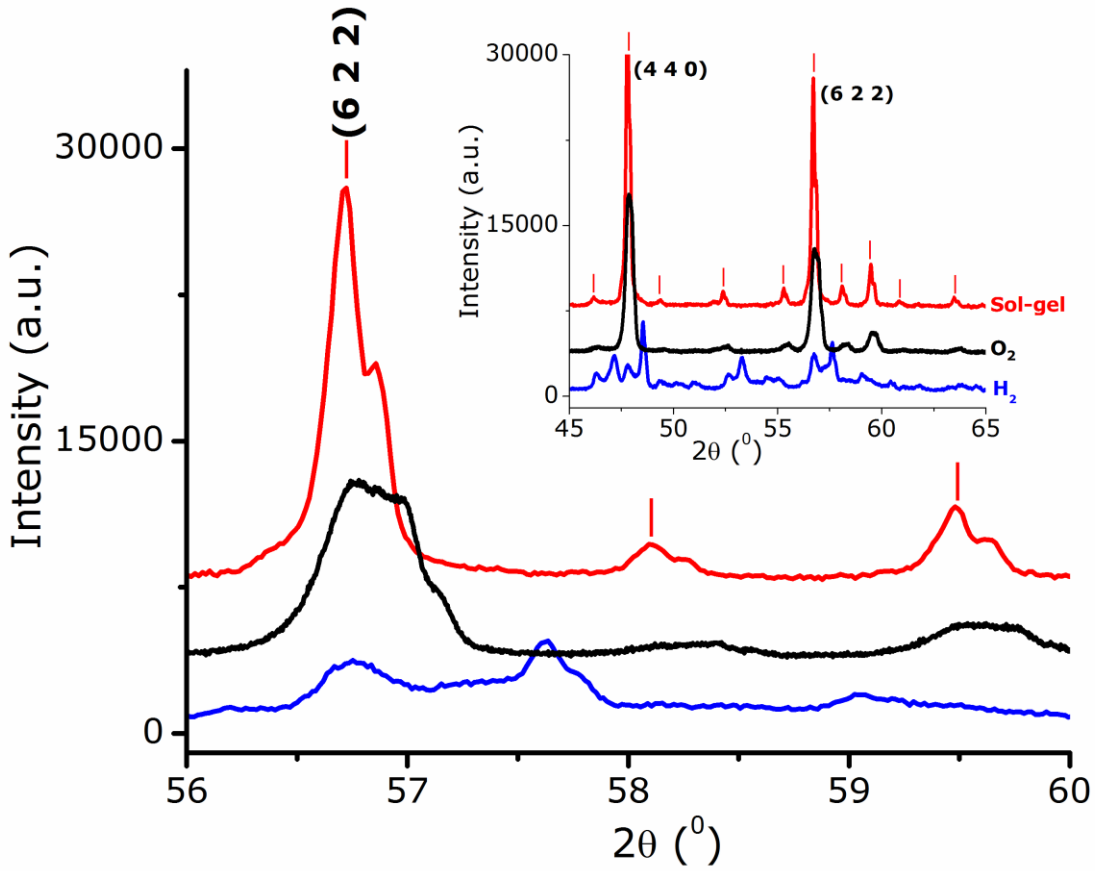

Figure 2.2 Room temperature powder X-ray diffractograms of three synthesis attempts of $YPrO_{3+\delta}$. Blue pattern: Y_2O_3 + Pr_2O_3 in 3% H_2 at 1450 ˚C for 24 hours, the insert highlights the multiphasic nature of that sample. Black pattern: $3Y_2O_3$ + Pr_6O_{11} in air at 1600 ˚C for 18 hours. Red pattern: $YPrO_{3+\delta}$ obtained via citric acid method followed by annealing in air at 900 ˚C and 1200 ˚C for 12 hours. The red tick marks indicate peaks (Cu-Kα_1 positions) belonging to the $YPrO_{3+\delta}$ bixbyite phase (space group: *Ia*-3).

2.5. Structure of $YPrO_3$ and $YPrO_{3+\delta}$

2.5.1. $YPrO_{3.00}$

$YPrO_3$ was obtained from $YPrO_{3.43(2)}$ (as synthesized) by reduction in 5% hydrogen flow at 1000 ˚C. The fully reduced $YPrO_3$ phase crystallizes in the cubic bixbyite structure (space group: *Ia-3, #206*) with a = 10.87857(7) Å. The structure was fully refined using powder X-ray and neutron diffraction data simultaneously with 32 parameters. Figure 2.4 shows the Rietveld plot for the $YPrO_{3.00}$ refinement. The Y^{3+} and Pr^{3+} cations are fully disordered on the *8b* and *24d* sites and form together a distorted cubic close packed cation sublattice. The Y^{3+}/Pr^{3+} on the *8b* site forms a regular octahedron with (Y/Pr)-O bond lengths of (2.345(1) Å) and the Y^{3+}/Pr^{3+} on the *24d* site shows distorted octahedral coordination with 2 bonds each at 2.396(1) Å, 2.335(1) Å, and 2.291(1) Å and a resulting octahedral distortion index Δ_{oct} = 0.00034. ($\Delta_{polyhedra} = \frac{1}{n}\sum_{i=1}^{n}[(d_i - \langle d\rangle)/\langle d\rangle]^2$). Table 2.1 lists all atomic positions and Table 2.2 lists selected bond distances for the $YPrO_3$ structure. The structure of $YPrO_{3.00}$ agrees well with the structure of Y_2O_3[25] with a similar octahedral distortion index Δ_{oct} = 0.00031 for the *24d* site in Y_2O_3.

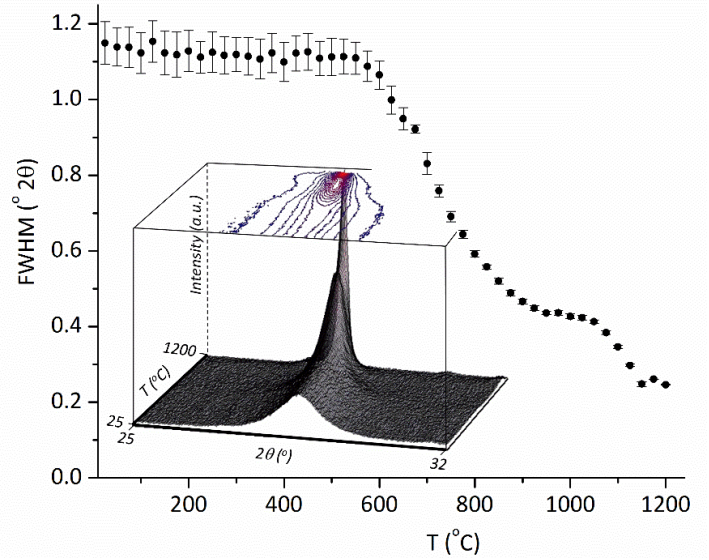

Figure 2.3 Evolution of the FWHM of the (222) peak for the $YPrO_{3+\delta}$ sol-gel sample as a function of temperature during annealing. The insert shows the sharpening of the (222) peak as a surface and contour plot.

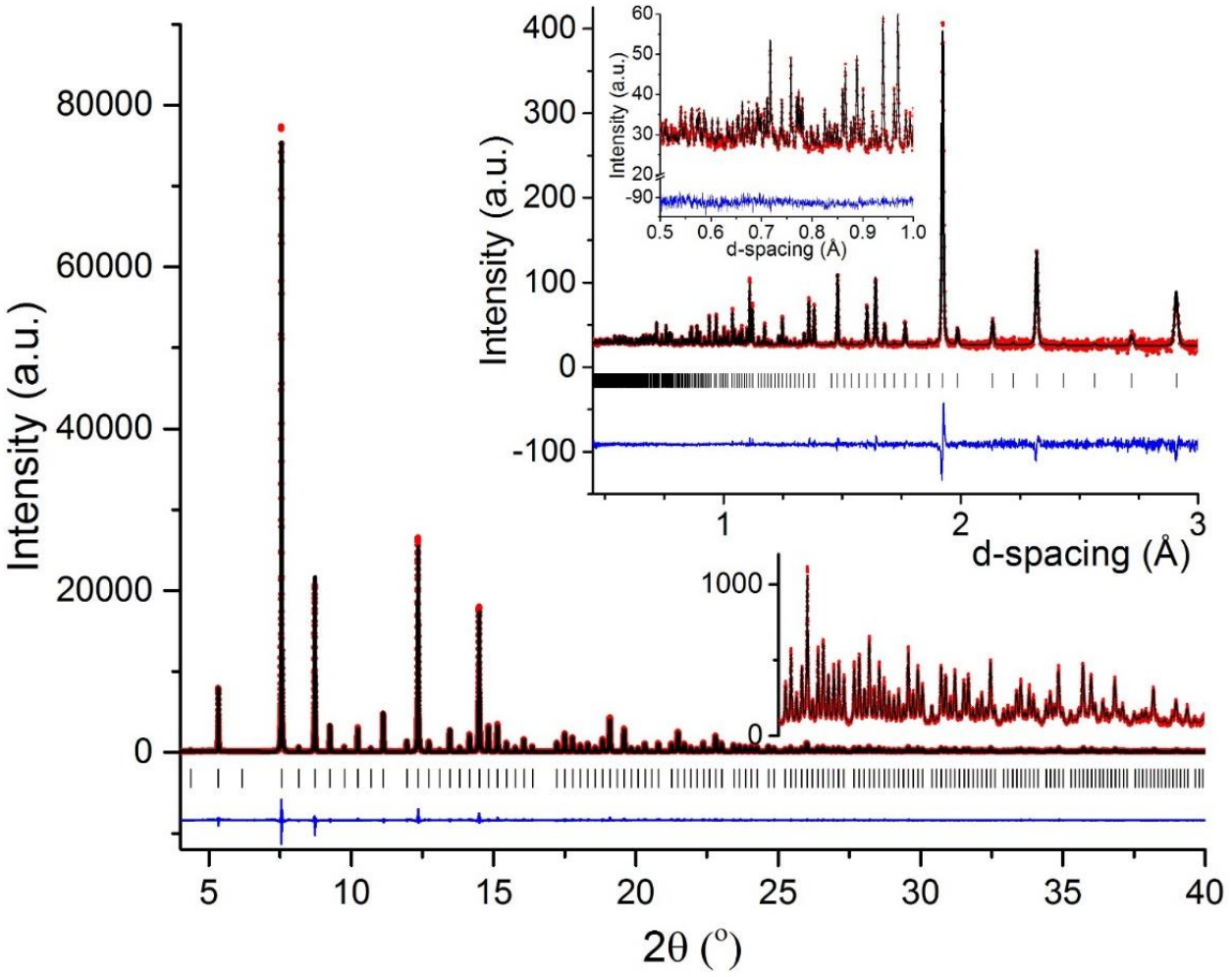

Figure 2.4 Rietveld plots for the refinement of the cubic bixbyite phase $YPrO_{3.00}$. (a-1) synchrotron X-ray data, (a-2) synchrotron X-ray data for $25^{\circ} \leq 2\theta \leq 40^{\circ}$ with 20 fold intensity magnification, (b-1) time of flight neutron diffraction data, (b-2) time of flight neutron diffraction data zoom. Red symbols = observed data, black line = fit, blue line = difference, tick marks = Bragg positions. All crystallographic information can be found in table 2.1

.

Table 2.1 Structural parameters for the cubic bixbyite phases (space group: $Ia\bar{3}$ (#206)) of $YPrO_{3.00}$, $YPrO_{3.43(2)}$ using Y/Pr on the 8*b* site, and $YPrO_{3.43(2)}$ using Y/Pr on the *16c* site. Values were obtained from simultaneous Rietveld Refinement against synchrotron powder X-ray diffraction data and time-of-flight powder neutron data measured at room temperature.

Composition		**$YPrO_{3.00}$**	**$YPrO_{3.43(2)}$ (Anisotropic)**	**$YPrO_{3.43(2)}$ (Site Disorder)**
Space Group		$Ia\bar{3}$ (#206)	$Ia\bar{3}$ (#206)	$Ia\bar{3}$ (#206)
Unit Cell	*a* (Å) V (Å^3)	10.87857 (7) 1287.406 (14)	10.763521(45) 1246.9903(90)	10.763521 (45) 1246.9903 (90)
Y/Pr (*8b*) (*¼, ¼, ¼*)	Occupancy (%): Y Pr B_{iso} (Å^2) β(11)/ β(22)/ β(33) β(12)/ β(13)/ β(23)	 51 (3) 49 (3) 0.408 (11)	 45 (7) 55 (7) 0.00426 (48) 0.00386 (38)	
Y/Pr (*16c*) (*x, x, x*)	*x/a* Occupancy (%) Y Pr β(11)/ β(22)/ β(33) β(12)/ β(13)/ β(23)			0.23810 (45) 49 (1) 51 (1) 0.00049 (50) 0.00034 (35)
Y/Pr (*24d*) (*x, 0, ¼*)	*x/a* Occupancy (%): Y Pr B_{iso} (Å^2)	-0.03021 (13) 50 (1) 50 (1) 0.367 (34)	-0.01751 (23) 52 (3) 48 (3) 0.80 (6)	-0.01740 (22) 50 (1) 50 (1) 0.82 (7)
O (*48e*) (*x, y, z*)	*x/a* *y/b* *z/c* Occupancy (%) B_{iso} (Å^2)	0.39017 (82) 0.15084 (82) 0.38033 (82) 100 0.520 (121)	0.3829 (18) 0.1454 (17) 0.3801 (20) 100 (2) 1.07 (20)	0.3826 (18) 0.1456 (16) 0.3800 (20) 100 (5) 1.08 (19)
O (*16c*) (*x, x, x*)	*x/a* Occupancy (%) B_{iso} (Å^2)		0.8875 (44) 42 (2) 1.07 (20)	0.8867 (44) 42 (5) 1.08 (19)
χ^2:	Neutron (T.O.F.)[a] X-ray (λ=0.4138 Å)[b]	1.65 1.58	1.95 2.76	1.93 2.66

[a]Neutron T.O.F range: 10280 – 110417 μs, 5936 data points

[b]X-ray λ=0.4138 Å, 3.75° ≤ 2θ ≤ 49.99°, Δ2θ = 0.001°, 46240 data points

Table 2.2 Bond distances and distortion parameters for the cubic bixbyite phases (space group: $Ia\bar{3}$ (#206)) of $YPrO_{3.00}$, $YPrO_{3.43(2)}$ using Y/Pr on the *8b* site, and $YPrO_{3.43(2)}$ using Y/Pr on the *16c* site. Values were obtained from simultaneous Rietveld Refinement against synchrotron powder X-ray diffraction data and time-of-flight powder neutron data measured at room temperature.

		$YPrO_{3.00}$	**$YPrO_{3.43(1)}$ (Anisotropic)**	**$YPrO_{3.43(1)}$ (Site Disorder)**
Y/Pr (*8b*) (¼, ¼, ¼)	Y/Pr – O bond lengths	6 * 2.345(1) Å	6 * 2.297(3) Å 2 * 2.563(6) Å	
	Bond distortion Δ (average bond length used)	Δ_{oct} = 0.00000 (2.345 Å)	Δ_{oct} = 0.00000 (2.297 Å) Δ_7 = 0.00160 (2.335 Å) Δ_{cub} = 0.00239 (2.363 Å)	
Y/Pr (*16c*) (*x, x, x*)	Y/Pr – O bond lengths			3 * 2.396(3) Å 3 * 2.207(3) Å 1 * 2.327(6) Å 1 * 2.770(6) Å
	Bond distortion Δ (average bond length used)			Δ_{oct} = 0.00170 (2.302 Å) Δ_7 = 0.00146 (2.305 Å) Δ_{cub} = 0.00545 (2.363Å)
Y/Pr (*24d*) (*x, 0, ¼*)	Y/Pr – O bond lengths	2 * 2.396(1) Å 2 * 2.335(1) Å 2 * 2.291(1) Å	2 * 2.368(3) Å 2 * 2.358(3) Å 2 * 2.246(3) Å 2 * 2.370(6) Å	2 * 2.368(3) Å 2 * 2.361(3) Å 2 * 2.246(2) Å 2 * 2.373(6) Å
	Bond distortion Δ (average bond length used)	Δ_{oct} = 0.00034 (2.341 Å)	Δ_{oct} = 0.00057 (2.324 Å) Δ_7 = 0.00053 (2.330 Å) Δ_{cub} = 0.00049 (2.335 Å)	Δ_{oct} = 0.00057 (2.325 Å) Δ_7 = 0.00054 (2.332Å) Δ_{cub} = 0.00051 (2.337Å)

2.5.2. $YPrO_{3.43(2)}$

$YPrO_{3.43(2)}$ crystallizes in the cubic bixbyite structure (space group: *Ia*-3, *#206*). The structure was refined simultaneously against powder X-ray and time of flight powder neutron diffraction data using 35 parameters. The Y^{3+} and $Pr^{3+/4+}$ cations are fully disordered on the *8b* and *24d* sites. The additional oxide anions (beyond $O_{3.00}$) occupy the *16c* (*x, x, x*) site partially. The coordination polyhedra for both cation sites change from octahedral to cubic (with oxide defects). The initial Rietveld refinement using neutron diffraction data revealed a fully occupied *48e* site and a partially filled *16c* site for the oxide anions. The refinement did not indicate any redistribution of oxide anions from the *48e* to the *16c* position. Our refinements clearly confirm the assumption made by Rajendran et al.[20] and Kimmel et al.[18] that the additional oxygen is located in the *16c* site (*x, x, x*). We report for the first time the actual value of x = 0.8867(44). This is in good agreement with the results of Gabbitas et al.[26] for the $CeO_2 – Y_2O_3$ system, and Withers et al.[27] for ZrO_2 with R_2O_3 (R=Ho, Dy, Tb. and Gd). When the refinement was allowed to proceed with independent oxygen occupancies, a fully occupied *48e* site and a partially filled *16c* with an oxygen stoichiometry in close agreement with the thermal gravimetric oxygen stoichiometry of $YPrO_{3.43(2)}$ was revealed. During the final refinements the oxygen stoichiometry was constrained to $YPrO_{3.43}$ based on the TGA results obtained from the reduction to $YPrO_{3.00}$ in 5% hydrogen.

An abnormally large isotropic temperature factor was observed for Y^{3+} and $Pr^{3+/4+}$ cations on the *8b* site. All other sites had reasonable temperature factors. Refining the anisotropic temperature factors for the *8b* position reveals a large ellipsoidal component along the [111] direction pointing towards the additional oxide anions located in the *16c* site. The bonds between the *8b* cations and *16c* oxides (d = 2.563(6) Å) are significantly longer than the remaining bonds (d = 2.297(3) Å). Figure 2.5a illustrates the Y/Pr (*8b* site) coordination and its thermal ellipsoid, the crystallographic

details are reported in table 2.1 and bond lengths in table 2.2. Alternatively, the cations on the *8b* position at (¼, ¼, ¼) can be described with site splitting using the *16c* position (*x, x, x*). Using the site split model with $x = 0.23810(45)$ results in a marginally smaller χ^2 value with reasonable anisotropic temperature factors. Figure 2.5b shows the bonding and thermal ellipsoids for the site splitting (note that there is a 50% occupancy of the upper and lower illustration). For both models the *Ia*-3 symmetry constrains the anisotropic displacement parameters to be ellipsoids along the body diagonal. In the first model a very large ellipsoid is derived, whereas with the site disorder model more reasonable smaller thermal ellipsoids are refined. The site disorder model generates a local electron density minimum at the *8b* (¼, ¼, ¼) position, whereas a maximum is present at the *8b* site for the other model. It is not surprising to find a larger ellipsoid for the incorrect model in order to correctly model the electron density at the actual cation positions. The site disorder model agrees well with the X-ray and neutron diffraction data.

It should be noted that the oxide ions on the *16c* site do not show abnormally large temperature factors or any indication of additional site splitting. Consequently, the Y/Pr cations are situated in enlarged cavities whereas the anions are located in well-defined crystallographic positions. The rigid oxide lattice and the preferential occupancy of the *48e* oxide site suggest limited oxide ion conductivity for the $YPrO_{3+\delta}$ phases.

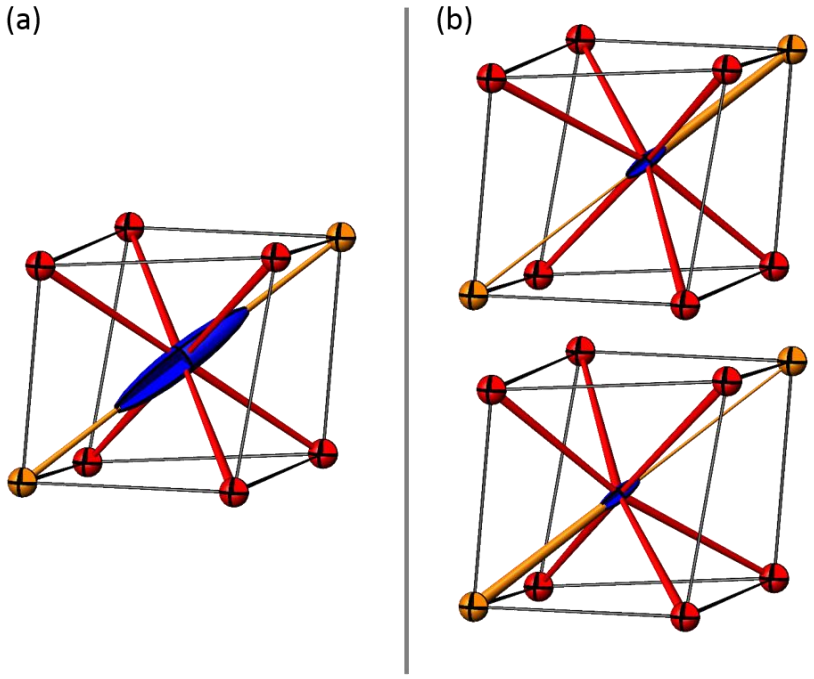

Figure 2.5 Y/Pr disorder and thermal parameters for $YPrO_{3.43}$. (a) Average structure with a large anisotropic displacement parameter for Y/Pr (blue ellipsoid) directed toward the *16c* oxygen positions (orange). (b) Disordered model with Y/Pr(1) on the *16c* site showing both possible Y/Pr locations along the body diagonal (upper and lower illustrations in (b)). The split site has 50% occupancy. Red ellipsoids = oxygen *8b* site, orange ellipsoids = oxygen *16c* site. Shorter bond distances are indicated with thicker bonds.

2.6. In-Situ Diffraction of Redox Processes

In-situ powder X-ray diffraction experiments permit to follow oxygen uptake and loss in $YPrO_{3+\delta}$ by following the unit cell parameter evolution as a function of temperature and atmosphere. $YPrO_{3.43(2)}$ was oxidized in flowing oxygen and reduced in 5% H_2 (balance N_2). X-ray diffractograms were collected every 25 °C up to 1200 °C and unit cell dimensions were determined with the Rietveld method using the bixbyite structure model. During oxidation the smaller Pr^{4+} cation (Pr^{3+}(*r*(VI) = 0.99 Å), Pr^{4+}(*r*(VI) = 0.85 Å)[24] causes a bixbyite unit cell dimension decrease despite the additional uptake of oxygen. Consequently, decreasing cell constants indicate oxidation and increasing cell constants relate to reduction.

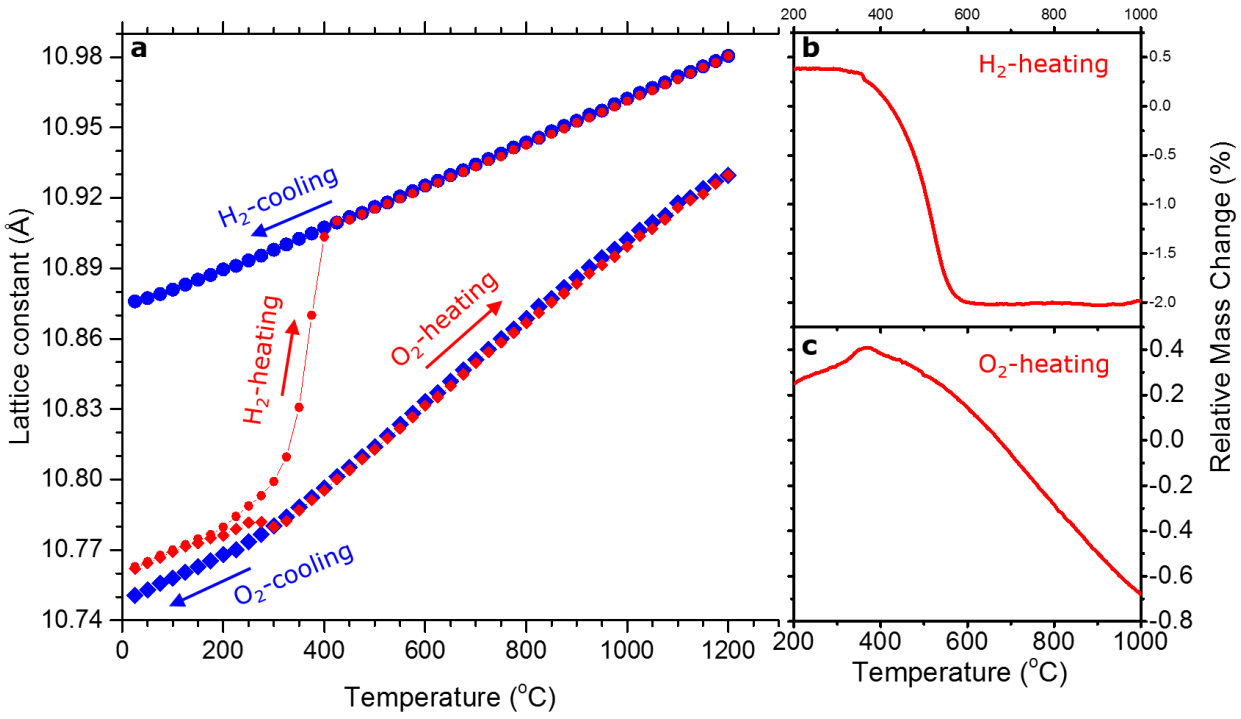

Figure 2.6 (a) Unit cell parameter evolution during oxidation in O_2 and reduction in 5% H_2 in N_2 measured as *in-situ* powder X-ray diffractogram using $YPrO_{3.43(2)}$.as the starting material at room temperature. All unit cell parameters were obtained from Rietveld refinements. Heating during oxidation = red solid diamonds, cooling in oxygen = blue solid diamonds. Reductive heating in 5% H_2 in N_2 = red solid circles and cooling in 5% H_2 in N_2 = blue solid circles. Error bars are smaller than the symbols and are typically in the range of 10^{-3} Å. Panel (b) is the TGA trace during reduction in 5% H_2 in N_2. In panel (c) the TGA trace during oxidation of $YPrO_{3.43(2)}$ in oxygen flow clearly shows the initial oxygen uptake followed by oxygen loss above 400 ˚C.

Figure 2.6 shows the cubic lattice constant evolution for both experiments. The red diamonds in figure 2.6a show that when heated in flowing oxygen, after the initial thermal expansion $YPrO_{3.43(2)}$ picks up additional oxygen between 250 ˚C and 300 ˚C (decrease in lattice constants) which is also confirmed with the thermogravimetric data (figure 2.6c). Above 300 ˚C the sample undergoes gradual reduction indicated by the increased slope and confirmed by TGA. During cooling in flowing oxygen (blue diamonds in figure 2.6a) the sample oxidizes gradually until 300 ˚C is reached. Below that temperature only lattice contraction is observed. The starting material was prepared in air (~20% O_2 rather than 100% O_2 as was used here) and was slightly oxidized in

pure oxygen to approximately $YPrO_{3.46}$. The reduction (red circles) of $YPrO_{3.43(2)}$ begins at 200 ˚C and is completed at 425 ˚C with the formation of $YPrO_{3.00}$. Upon further heating and final cooling (blue circles) $YPrO_{3.00}$ shows reversible linear thermal expansion and contraction. The reduction of $YPrO_{3.43(2)}$ is confirmed by the TGA data in figure 2.6b. Note that the seemingly higher reaction temperatures observed for the TGA traces are due to significantly faster heating rates (10 ˚C/min). The red triangles in figure 2.7a show the *in-situ* powder X-ray diffraction oxidation of $YPrO_{3.00}$ in oxygen flow. Figure 2.7b shows the contour plot for the (222) and (400) diffraction peaks during heating, clearly showing large peak shifts above 200 ˚C. Following the initial thermal expansion $YPrO_{3.00}$ oxidizes between 200 ˚C and 300 ˚C as indicated by a rapid unit cell dimension decrease. Above 300 ˚C the sample slowly loses oxygen which agrees with the data shown in figure 2.6. The TGA trace during heating of $YPrO_{3.00}$ in oxygen flow is shown in figure 2.7c. The sample reversibly oxidizes during cooling (blue triangles) followed by thermal contraction below 300 ˚C. No accurate unit cell dimensions are available for the data at 250 ˚C and 275 ˚C during heating because of continuous oxygen uptake during the 45 minute X-ray data collection times. The two solid circles in figure 2.7a indicate average cell constants for those temperatures.

Figure 2.6 and figure 2.7 clearly show why the attempted oxidative synthesis did not result in a pure phase. Higher reaction temperatures are required for the diffusion of ions in the sample; however, at these elevated temperatures the average oxidation state of praseodymium decreases. This causes the same problems that are seen with the reductive synthesis. The citric acid sol-gel synthesis results in a phase pure product due to the shorter diffusion pathways in the nano-precursor phases, thus permitting lower reaction temperatures. In conclusion oxidation at high temperatures does not necessarily result in oxygen uptake. $YPrO_{3+\delta}$ only oxidizes at low

temperatures, therefore slow cooling between 400 ˚C and 200 ˚C is required for obtaining fully oxidized phases.

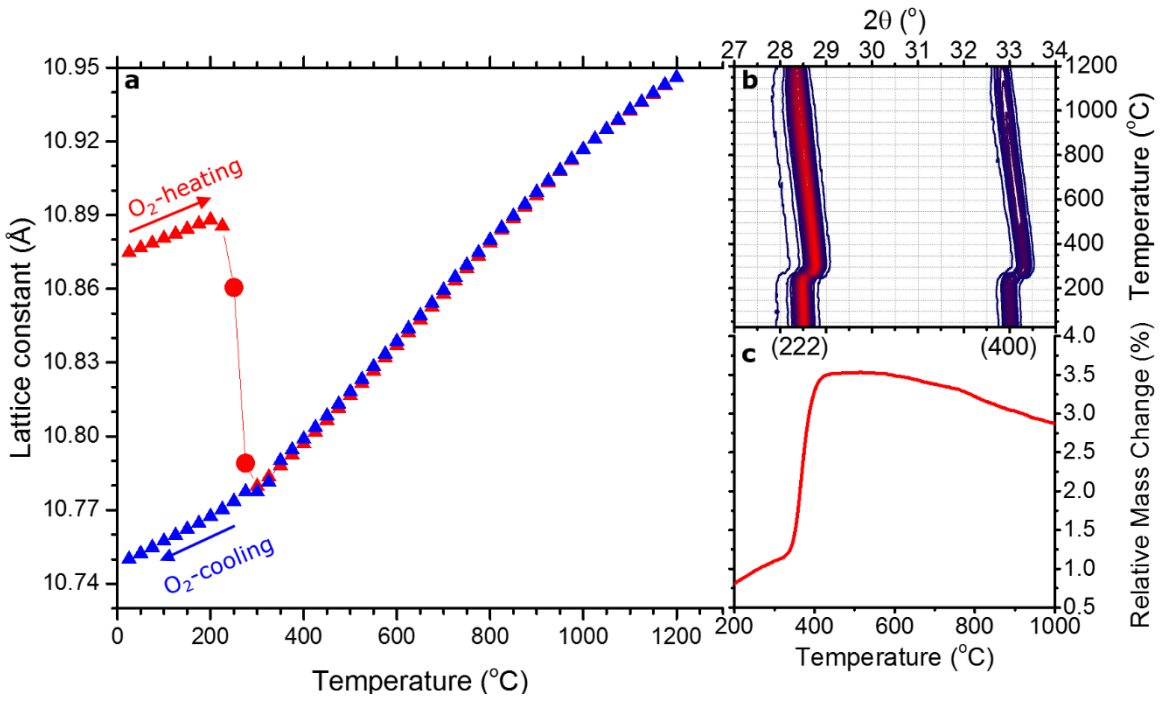

Figure 2.7 (a) Unit cell parameter evolution derived from *in-situ* powder X-ray diffraction during oxidation of the fully reduced form $YPrO_{3.00}$ in O_2. All unit cell parameters were obtained from Rietveld refinements. Oxidative heating = Red solid triangles, cooling in oxygen = blue solid triangles. The two solid circles indicate average cell constants while being oxidized during the X-ray data collection. Error bars are smaller than the symbols and are typically in the range of 10^{-3} Å. Panel (b) shows the contour plot for the (222) and (400) peaks during heating (blue = low intensity and red = high intensity). Panel (c) is the TGA trace during oxidation of $YPrO_{3.00}$ in O_2 flow indicating full oxidation to $YPrO_{3.46}$ followed by gradual reduction above 400 ˚C.

Kimmel et al.[18] quenched $YPrO_{3+\delta}$ in air producing biphasic samples. Those are most likely two bixbyite phases with differing oxygen content because the samples were cooled rapidly through the temperature range at which oxygen uptake occurs. This resulted in incomplete oxidation of the sample. Our results clearly demonstrate that solid-state reaction pathways and kinetics must be understood for the rational design of functional materials.

2.7. *Ex-Situ* Oxygen Control in $YPrO_{3+\delta}$ through Redox Chemistry

In-situ experiments showed the potential to form $YPrO_{3+\delta}$ with $0 \leq \delta \leq 0.46$ values. Varying δ was attempted in two ways; using an oxidative pathway and using a reductive pathway. In order to maximize the amount of oxygen in the structure, the final heating of the sol-gel synthesis was cooled in flowing oxygen rather than in air. The product was found (via reductive thermal gravimetric analysis) to be $YPrO_{3.46(2)}$. This product has similar lattice parameters to that resulting from the *in-situ* oxidations shown in 2.6. The synthesis in approximately 3 bars of oxygen pressure resulted in similar results. This suggests that the formation of the fully oxidized $YPrO_{3.5}$ phase will require significantly higher oxygen pressure. Reductions at a variety of temperatures has allowed for partial reduction of $YPrO_{3.43(2)}$. The correlation between unit cell dimensions and oxygen content was obtained from powder X-ray diffraction and reductive TGA data, respectively. Figure 2.8 illustrates the linear relation between unit cell parameters and oxygen content (linear fit with $R^2 = 0.99809$), permitting to determine oxygen content from unit cell dimensions for $YPrO_{3+\delta}$.

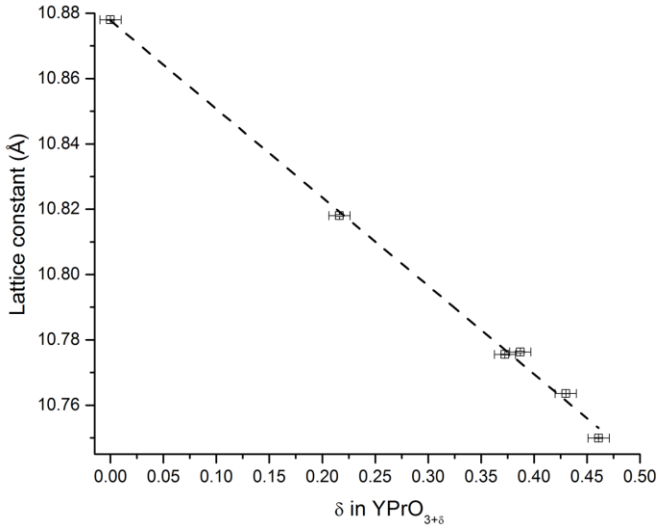

Figure 2.8 Illustration of the linear relation between the unit cell dimensions for $YPrO_{3+\delta}$ and oxygen stoichiometry. The oxygen stoichiometry was obtained from TGA data and the unit cell parameters were determined from powder X-ray diffraction based Rietveld analysis. The dashed line is a linear fit.

2.8. **Magnetism**

2.8.1. Magnetic Susceptibility

In figure 2.9 the fully reduced $YPrO_{3.00}$ shows splitting in the field cooled (FC) and zero-field cooled (ZFC) magnetic susceptibility data between 1.8 K and approximately 50 K for an applied field of 0.1 T. For a stronger magnetic field of 1 T the FC and ZFC data overlap completely and also follow the ZFC data in a 0.1 T field. The FC – ZFC divergence between 1.8 K and 50 K in a 0.1 T field is likely due to a very small impurity in the sample. The Weiss temperature, θ_{CW}, and effective moment, μ_{eff}, were extracted from the Curie-Weiss fit, $\chi = C/(T-\theta_{CW})$, at high temperature (from 80 K to 300 K). In this temperature range higher energy crystal field levels are populated by thermal excitations leading to a large Weiss temperature (θ_{CW} = -72.68 (1) K), this is commonly observed in rare-earth magnetic systems.[28,29] The effective moment μ_{eff} = 3.54(10) μ_B is in close agreement with the expected effective magnetic moment for Pr^{3+}.[30] The magnetic susceptibility data for the oxidized $YPrO_{3.43(2)}$ sample (Figure 2.10) show no divergence between the FC and

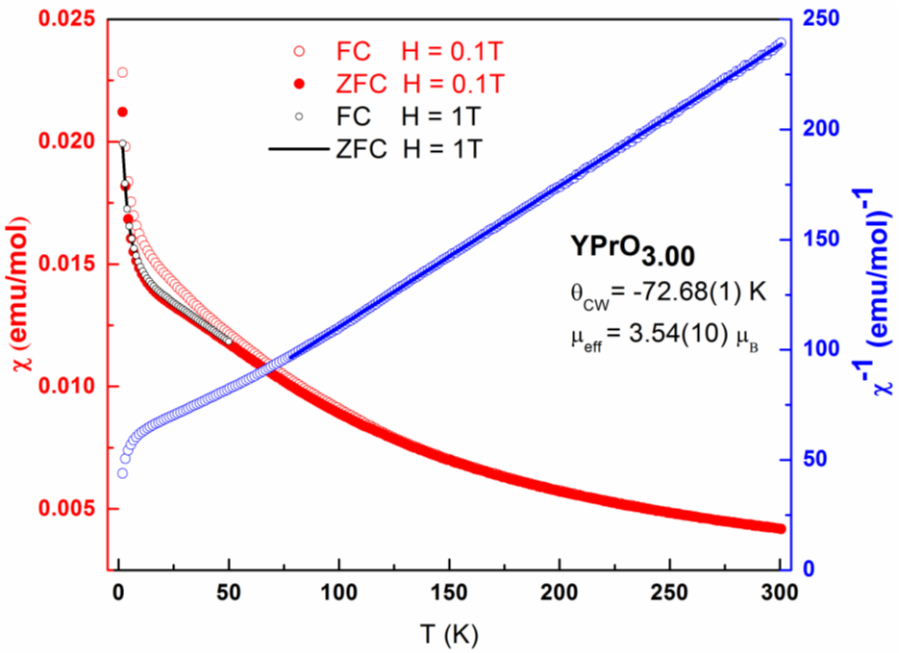

Figure 2.9 Magnetic susceptibility data for $YPrO_{3.00}$. The zero field cooled data (solid red circles) and field cooled data (open red circles) were measured in a 0.1 T field. The blue symbols show the inverse magnetic susceptibility data and the solid blue line is the fit to the Curie-Weiss law for the 0.1 T data between 80 K and 300 K. The solid black line (ZFC) and the open black circles (FC) and were measured in a field of 1 T.

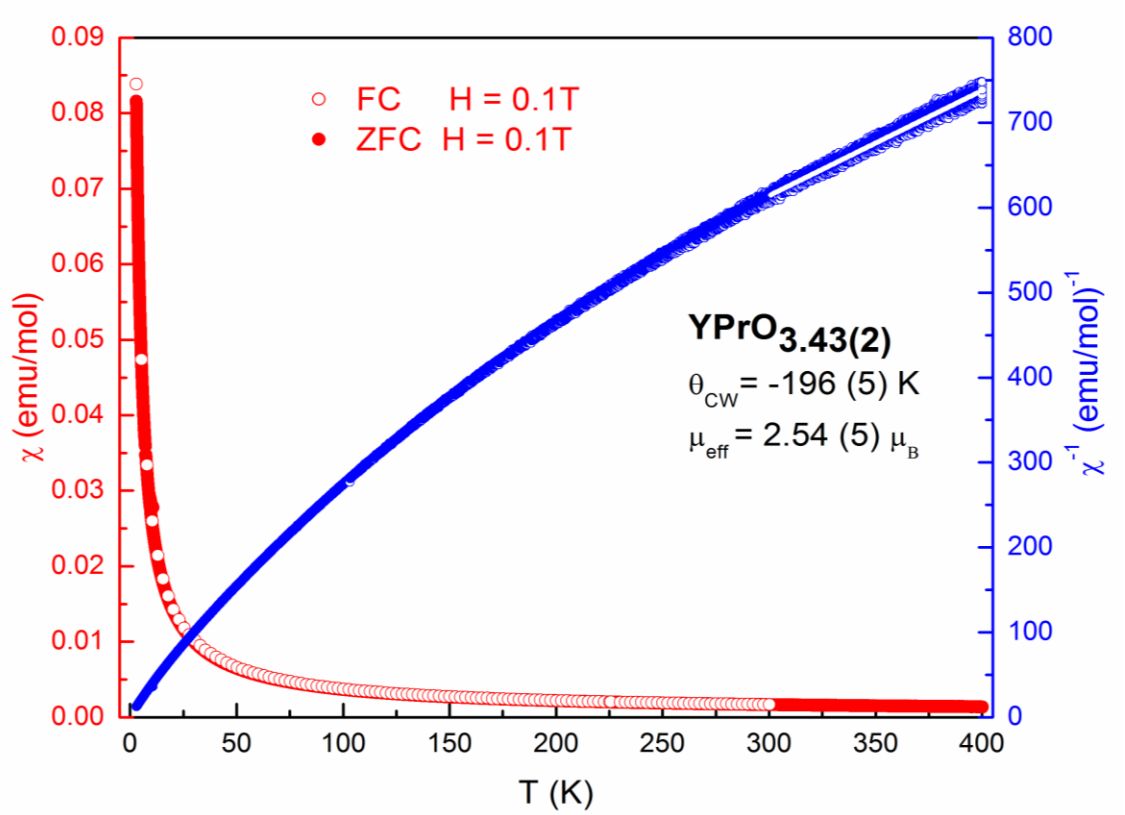

Figure 2.10 Magnetic susceptibility data for $YPrO_{3.43(2)}$. The zero field cooled data (solid red circles) and field cooled data (open red circles) were measured in a 0.1 T field. The blue symbols show the inverse magnetic susceptibility data and the solid blue line is the fit to the Curie-Weiss law for the 0.1 T data between 300 K and 400 K.

ZFC data in a 0.1 T field. This indicates the absence of a glassy or ferromagnetic cooperative state for the measured temperature range from 2 K to 400 K. An effective magnetic moment of μ_{eff} = 2.54 (5) μ_B and a Weiss-temperature θ_{CW} = -196 (5) K were determined from a Curie-Weiss fit between 300 and 400K. These results suggest a much lower effective magnetic moment than for the reduced $YPrO_{3.00}$ phase. This is in agreement with the lower expected effective magnetic moment of 2.54 μ_B for Pr^{4+}. It is noted that the measured effective magnetic moment of 2.54 (5) μ_B is slightly smaller than the expected value for $YPrO_{3.43(2)}$ due to the curvature of the data even at these high temperatures. The very high Weiss temperature, θ_{CW} = -196 (5) K, in $YPrO_{3+\delta}$ is due to crystal field effects, which can shift the measured Weiss temperature to higher

values due to electronic transitions. This is common in many rare earth magnetic systems as well.[31,32]

2.9. Conclusion

Phase pure $YPrO_{3.43(2)}$ was synthesized via a citric acid sol-gel method and subsequently reduced to $YPrO_3$. The structural details of the cubic bixbyite phases (space group: *Ia*-3) were obtained from synchrotron powder X-ray diffraction and time-of-flight powder neutron diffraction. Y and Pr are fully disordered on both cation sites in $YPrO_{3+\delta}$. Even the most oxidized samples do not form the high symmetry cubic fluorite phases (space group: *Fm*-3*m*); instead the bixbyite structure is found for the entire range of oxygen stoichiometries. We are reporting accurate oxygen atomic coordinates and provide details regarding the coordination in those bixbyite phases. Upon oxidation, cation site disorder is observed where the cations ($Y^{3+}/Pr^{3+/4+}$) in the *8b* site migrate to the partially occupied *16c* site. Thus the oxide sublattice provides a strong framework and the original *8b* site is an oversized cavity for Y^{3+} and Pr^{4+}. In contrast, no site disorder is observed for the *24d* cations. *In-situ* redox reactivity was investigated using high temperature X-ray diffraction and thermal gravimetric analysis. The *in-situ* diffraction data clearly show the reversible topotactic reduction and oxidation for the entire range of $0 \leq \delta \leq 0.46$. The redox chemistry occurs at fairly low temperatures (200 – 400 ˚C) with no indication of phase decomposition up to 1200 ˚C. The unit cell volume decreases during oxidation due to the smaller Pr^{4+} in comparison to Pr^{3+} ion. The lattice provides sufficient space to accommodate the additional oxygen without an overall lattice expansion. The linear relation between the cubic cell parameter and oxygen content, δ, provides an excellent calibration for the praseodymium oxidation state in $YPrO_{3+\delta}$. We report the bulk magnetic susceptibility data, effective magnetic moments and indicate the thermal population of

high crystal field states for the Pr^{3+} and Pr^{4+} containing $YPrO_{3+\delta}$ phases. This work clearly indicates that understanding the redox chemistry of solid-state materials is an important step toward the successful synthesis of functional materials.

References

(1) Goodenough, J. B. Ceramic Technology: Oxide-Ion Conductors by Design. *Nature* **2000**, *404* (6780), 821–823.

(2) Bevan, D. J. M.; Martin, R. L. The Role of the Coordination Defect: A New Structural Description of Four Fluorite-Related Sesquioxide Minerals, Bixbyite (Mn_2O_3), Braunite (Mn_7SiO_{12}), Braunite II ($CaMn_{14}SiO_{24}$), Parwelite ($Mn_{10}Sb_2As_2Si_2O_{24}$), and Their Structural Relationships. *J. Solid State Chem.* **2008**, *181* (9), 2250–2259.

(3) Martin, R. L. Structural Theory for Non-Stoichiometry. Part 1. Defect Fluorite-Type Structures: Lanthanoid Oxides MO_x with $1.7<x<2.0$. *Dalton Trans.* **1974**, *4*, 1335–1350.

(4) Shafi, S. P.; Lundgren, R. J.; Cranswick, L. M. D.; Bieringer, M. Formation, Structure and Magnetism of the Metastable Defect Fluorite Phases $AVO_{3.5+x}$ (A = In, Sc). *J. Solid State Chem.* **2007**, *180* (12), 3333–3340.

(5) Shafi, S. P.; Hernden, B. C.; Cranswick, L. M. D.; Hansen, T. C.; Bieringer, M. Topotactic Oxidation Pathway of $ScTiO_3$ and High-Temperature Structure Evolution of $ScTiO_{3.5}$ and $Sc_4Ti_3O_{12}$-Type Phases. *Inorg. Chem.* **2012**, *51* (3), 1269–1277.

(6) Lundgren, R. J.; Cranswick, L. M. D.; Bieringer, M. In Situ X-Ray Powder Diffraction, Synthesis, and Magnetic Properties of $InVO_3$. *J. Solid State Chem.* **2006**, *179* (12), 3599–3606.

(7) Geller, S. Structure of α-Mn_2O_3, $(Mn_{0.983}Fe_{0.017})_2O_3$ and $(Mn_{0.37}Fe_{0.63})_2O_3$ and Relation to Magnetic Ordering. *Acta Crystallogr.* **1971**, *27B* (4), 821–828.

(8) Shafi, S. P.; Kotyk, M. W.; Cranswick, L. M. D.; Michaelis, V. K.; Kroeker, S.; Bieringer, M. In Situ Powder X-Ray Diffraction, Synthesis, and Magnetic Properties of the Defect Zircon Structure $ScVO_{4-X}$. *Inorg. Chem.* **2009**, *48* (22), 10553–10559.

(9) Schneider, S. J.; Roth, R. S.; Waring, J. L. Solid State Reactions Involving Oxides of Trivalent Cations. *J. Res. Natl. Bur. Stand.* **1961**, *65A* (4), 345–374.

(10) Shannon, R. D. Synthesis of Some New Perovskites Containing Indium and Thallium. *Inorg. Chem.* **1967**, *6* (8), 1474–1478.

(11) Geller, S.; Bala, V. B. Crystallographic Studies of Perovskite-like Compounds. II. Rare Earth Alluminates. *Acta Crystallogr.* **1956**, *9* (12), 1019–1025.

(12) Roth, R. S.; Schneider, S. J. Phase Equilibria in Systems Involving the Rare-Earth Oxides . Part 1 . Polymorphism of the Oxides of the. *J. Res. Natl. Bur. Stand.* **1960**, *64A* (4), 309–316.

(13) Schneider, S. J.; Roth, R. S. Phase Equilibria in Systems Involving the Rare-Earth Oxides. Part II. Solid State Reactions in Trivalent Rare-Earth Oxide Systems. *J. Res. Natl. Bur. Stand.* **1960**, *64A* (4), 317–332.

(14) Chavan, S. V.; Achary, S. N.; Tyagi, A. K. XRD Investigations in the Nd_2O_3-Y_2O_3 System and Structural Studies of a Stabilized Monoclinic Phase. *J. Alloys Compd.* **2007**, *441* (1–2), 332–336.

(15) Reid, A. F.; Ringwood, A. E. High-Pressure Modification of $ScAlO_3$ and Some Geophysical Implications. *J. Geophys. Res.* **1975**, *80* (23), 3363–3370.

(16) Wells, A. F. *Structural Inorganic Chemistry*, 5th ed.; Clarendon Press: Oxford, 1984.

(17) Giaquinta, D. M.; zur Loye, H.-C. Structural Predictions in the ABO_3 Phase Diagram. *Chem. Mater.* **1994**, *6* (4), 365–372.

(18) Kimmel, G.; Zabicky, J.; Goncharov, E.; Mogilyanski, D.; Venkert, A.; Bruckental, Y.; Yeshurun, Y. Formation and Characterization of Nanocrystalline Binary Oxides of Yttrium and Rare Earths Metals. *J. Alloys Compd.* **2006**, *423* (1–2), 102–106.

(19) Rajendran, M.; Mallick, K. K.; Bhattacharya, A. K. Preparation and Characterization of $LnPrO_{(3+y)}$ (Ln = Y and Lanthanide) - a Series of Mixed Lanthanide Oxides. *Mater. Lett.* **1998**, *37* (1–2), 10–16.

(20) Rajendran, R.; Krishna, M. G.; Mallick, K. K.; Bhattacharya, A. K. Structure, Oxygen Stoichiometry and Electrical Conductivity of $LnPrO_{(3+y)}$ (Ln = Y and Lanthanide) Oxides. *Mater. Sci. Eng.* **1999**, *58B* (3), 215–220.

(21) Sanjaya Ranmohotti, K. G.; Josepha, E.; Choi, J.; Zhang, J.; Wiley, J. B. Topochemical Manipulation of Perovskites: Low-Temperature Reaction Strategies for Directing Structure and Properties. *Adv. Mater.* **2011**, *23* (4), 442–460.

(22) Wang, J.; Toby, B. H.; Lee, P. L.; Ribaud, L.; Antao, S. M.; Kurtz, C.; Ramanathan, M.; Von Dreele, R. B.; Beno, M. A. A Dedicated Powder Diffraction Beamline at the Advanced Photon Source: Commissioning and Early Operational Results. *Rev. Sci. Instrum.* **2008**, *79* (8), 1–7.

(23) Rodriguez-Carvajal, J. FullProf.2K. Full Prof 2K V. 4.40 2013.

(24) Shannon, R. D. Revised Effective Ionic Radii and Systematic Studies of Interatomic Distances in Halides and Chalcogenides. *Acta Crystallogr.* **1976**, *A32* (5), 751–767.

(25) Paton, M. G.; Maslen, E. N. A Refinement of the Crystal Structure of Yttria. *Acta Crystallogr.* **1965**, *19*, 307–310.

(26) Gabbitas, N.; Thompson, J. G.; Withers, R. L.; Rae, A. D. A Single Crystal X-Ray Study of the Fluorite-Related Solid Solutions of $CeO_{2-Y}O_{1.5}$. *J. Solid State Chem.* **1995**, *115* (1), 23–36.

(27) Withers, R. L.; Thompson, J. G.; Gabbitas, N.; Wallenberg, L. R.; Welberry, T. R. Microdomains, Solid Solutions and the Defect Fluorite to C-Type Sesquioxide Transition in CeO_2-$RO_{1.5}$ and ZrO_2-$RO_{1.5}$ Systems. *J. Solid State Chem.* **1995**, *120* (2), 290–298.

(28) Sharma, A. Z.; Silverstein, H. J.; Hallas, A. M.; Luke, G. M.; Wiebe, C. R. Structure and Magnetic Properties of New Be-Substituted Langasites $A_3Ga_3Ge_2BeO_{14}$ (A=Pr, Nd, and Sm). *J. Solid State Chem.* **2016**, *233*, 14–22.

(29) Hinatsu, Y.; Doi, Y.; Wakeshima, M. Antiferromagnetic Transitions of Osmium-Containing Rare Earth Double Perovskites Ba_2LnOsO_6 (Ln=rare Earths). *J. Solid State Chem.* **2013**, *206*, 300–307.

(30) Kittel, C. *Introduction to Solid State Physics*, 7th ed.; John Wiley and Sons, Inc.: Ann Arbor, MI, USA, 1996.

(31) Sharma, A. Z.; Silverstein, H. J.; Hallas, A. M.; Luke, G. M.; Wiebe, C. R. Sub-Kelvin Magnetic Order in $Sm_3Ga_5O_{12}$ Single Crystal. *J. Magn. Magn. Mater.* **2015**, *384*, 235–240.

(32) Hallas, A. M.; Arevalo-Lopez, A. M.; Sharma, A. Z.; Munsie, T.; Attfield, J. P.; Wiebe, C. R.; Luke, G. M. Magnetic Frustration in Lead Pyrochlores. *Phys. Rev. B: Condens. Matter*

Mater. Phys. **2015**, *91* (10), 104417.

Chapter 3. Oxygen Trapping and Cation Site-Splitting in $Y_{(2-x)}Pr_xO_{3+\delta}$ ($0.0 \leq x \leq 2.0$ and $\delta \leq 1.0$)

Joey A. Lussier [a,b], Graham Devitt [a], Kevin M. Szkop [a], Mario Bieringer [a,b]

[a] Department of Chemistry, University of Manitoba, Winnipeg, MB, R3T 2N2, Canada

[b] Manitoba Institute for Materials, University of Manitoba, Winnipeg, MB, R3T 2N2, Canada

First Published in Journal of Solid State Chemistry, 2016, 242, 126 – 132

DOI: http://dx.doi.org/10.1016/j.jssc.2016.03.017

Preface

This publication is a continuation of the work done in the previous chapter, and the second article published on the $Y_{2-x}Pr_xO_{3+\delta}$ system. It expands the study to include the full solid solution from Y_2O_3 to Pr_2O_3. Varying the Y:Pr ratio allows for control of oxide defects concentrations and the exploration of the effect of these defects on the bixbyite and fluorite structures. Namely, a focus on understanding the response of the cations to differing amounts of anion vacancies is presented. This is of particular interest for solid-state electrolyte applications and comments on this are made throughout the manuscript. This manuscript was accepted by the Journal of Solid State Chemistry on March 9th, 2016.

Contributions

Joey A. Lussier, Graham Devitt, and Kevin M. Szkop, were all responsible for the synthesis of the materials and data collection. Analysis was completed by Joey A. Lussier, and the manuscript was written by Joey A. Lussier and Mario Bieringer.

3.1. Abstract

The reduction and oxidation of the solid solution $Y_{2-x}Pr_xO_{3+\delta}$ ($0.0 \leq x < 2.0$ and $\delta \leq 1.0$) is investigated with emphasis on potential solid-state electrolyte applications in solid oxide fuel cells. The fully reduced solid solution $Y_{2-x}Pr_xO_3$ ($0.0 \leq x < 2.0$) crystallizes in the bixbyite structure (*Ia-3*). The oxidized solid solution $Y_{2-x}Pr_xO_{3+\delta}$ ($0.0 \leq x < 1.4$) forms bixbyite phases (*Ia-3*) whereas $Y_{2-x}Pr_xO_{3+\delta}$ ($1.4 \leq x < 2$) compositions form fully disordered defect fluorite structures (*Fm-3m*) with variable oxide defect concentrations. The two cation positions are investigated in detail using synchrotron powder X-ray and time of flight neutron diffraction data. In the bixbyite structures the *8c* cation site splits into the *16c* cation site and the *24d* cation position migrates toward the ideal fluorite coordination upon oxidation. Reductive in-situ diffraction experiments reveal the co-existence of the fluorite and bixbyite structure only in a narrow temperature range. During oxidation of the bixbyite phase a new *16c* oxide anion site is populated. The impact of the *16c* oxide site population on the cation sublattice is being discussed.

3.2. Introduction

Transition metal and rare-earth oxide phases span a broad range of structural motives and extended structure types. Combining this structural diversity with redox active cations can be utilized for materials design. In addition, the chosen synthesis methods decide over the product structures. Oxide defect structures are widely employed for ion conductors and find applications as solid-state oxide electrolytes in solid-state oxide fuel cells (SOFCs).[1] Oxide ion conductors are ideally designed from high symmetry oxide structures with a sufficient number of oxide defects that are fully disordered. The activation energies for oxide migration between equivalent sites needs to be minimized in order to increase ion mobility in these solid-state electrolytes.[2] Ion mobility is inhibited by the presence of ordered oxide defects in extended solids through the introduction of non-equivalent oxide sites. A deeper understanding of the formation and annihilation of oxide defects can be gained from following oxidation and reduction of good defect host structures. The cubic bixbyite structure (figure 3.1) is an ordered defect oxide structure, with cations completely disordered on the fully occupied *8b* and *24d* sites with 25% oxide defects with respect to the oxide defect free fluorite parent structure.[3] The oxide anions are found in the fully occupied *48e* site. Commonly 5% to 10% oxide defects are expected to optimize oxide ion conduction in defect fluorite structures.[2] The cubic fluorite structure crystallizes in space group *Fm-3m* with one cation site (*4a*) and one anion site (*8c*).[3] Consequently a mixed cation system of composition $A'_{(2-x)}A''_xO_{4-y}$ must be cation disordered. Additionally, the oxide defects must also be disordered to maintain *Fm-3m* symmetry. If an initial bixbyite structure is oxidized to a defect fluorite structure an order/disorder transition is expected for the oxide/defect sublattice. Figure 3.1 illustrates the relation between the bixbyite structure and the fluorite structure.

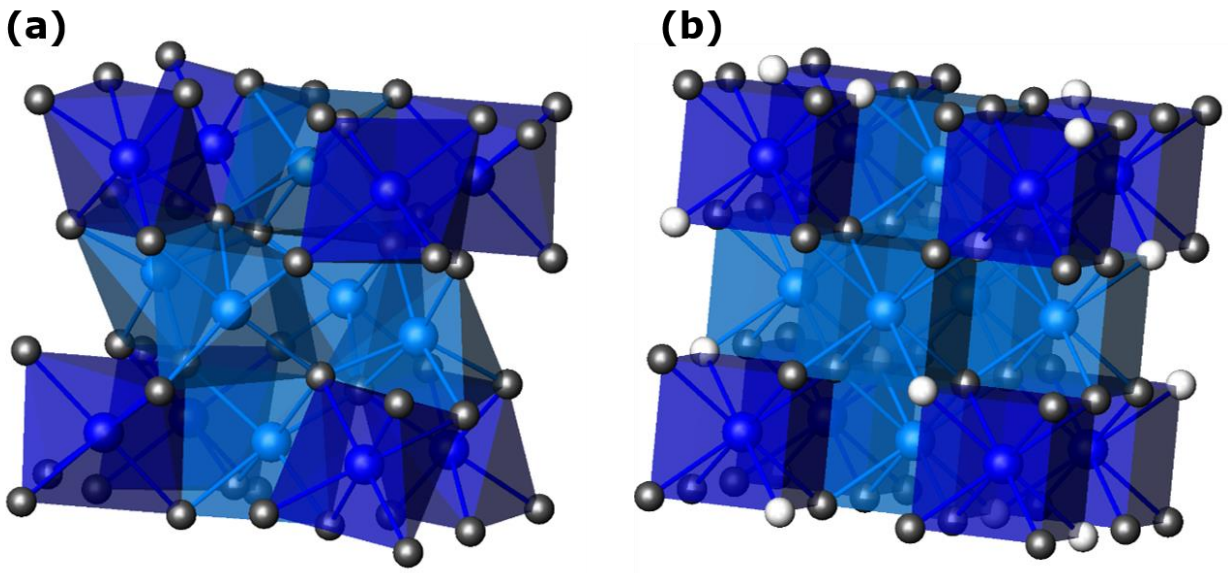

Figure 3.1 Relation between bixbyite and fluorite structures with fcc cation lattices and anions located in tetrahedral holes. (a) Cubic bixbyite structure in space group *Ia*-3. Dark blue = *8b* cation site, light blue = *24d* cation site, grey = *48e* anion site. (b) Cubic fluorite structure in space group *Fm*-3*m* with all cations (light and dark blue) on the *4a* site and all anions (grey and white) on the *8c* site. The white anions can be thought of as inserted into the bixbyite structure raising the cation coordination from 6 to 8. Note that the cations in the bixbyite structure form a slightly distorted fcc lattice.

This work explores the transition into the ordered and disordered defect structures as a function of reduction and oxidation, respectively. A sufficient amount of A"$^{4+}$ cations is required in order to reach a sufficient oxygen composition for the formation of the disordered defect fluorite structure.

The $Y_{(2-x)}Pr_xO_{3+\delta}$ system is an excellent candidate to follow the structural evolution as a function of A' and A" cation ratio and addition of extra oxygen. Previously the $Y_{(2-x)}Pr_xO_3$ phases have been reported as thin films prepared by molecular beam epitaxy as fully reduced bixbyites.[4–7] Kimmel et al. reported a biphasic gap for the $Y_{(2-x)}Pr_xO_{3+\delta}$ system for bulk materials with $1 \leq x \leq 1.33$.[8] In a recent study $YPrO_{3+\delta}$ has been reported as a single phase bixbyite and it has been shown[9] that oxygen addition to $YPrO_3$ causes the *8b* cation site to split from the ideal position into a half occupied *16c* position. The additional oxygen is added to a newly created *16c* site without

affecting the occupancy of the original *48e* site. No order/disorder transition is seen during the oxidation from $YPrO_3$ to $YPrO_{3.43(2)}$. A schematic of the oxidation of the ABO_3 bixbyite to $ABO_{3+\delta}$ is shown in figure 3.2. The $Y_{(2-x)}Pr_xO_{3+\delta}$ ($0.0 \leq x \leq 2.0$, and $0 \leq \delta \leq 1.0$) system is ideal for the investigation of defect annihilation and formation. We are reporting here that the $Y_{(2-x)}Pr_xO_{3+\delta}$ system can be oxidized at low temperatures and forms a solid solution for $0 \leq x \leq 2$ for partially and fully oxidized samples without any biphasic region. The reduction – oxidation reactions are also fully reversible. Furthermore, the synthesis of the x = 1 material reported by Lussier et al.[9] is well understood, employing a sol-gel synthesis utilizing the citrate method. Understanding the oxygen loss at high temperatures led to a reliable synthesis method for the full solid solution. Slow-cooling results in monophasic samples. In contrast quenching samples[8,10,11] potentially results in multiphasic products with variable oxygen

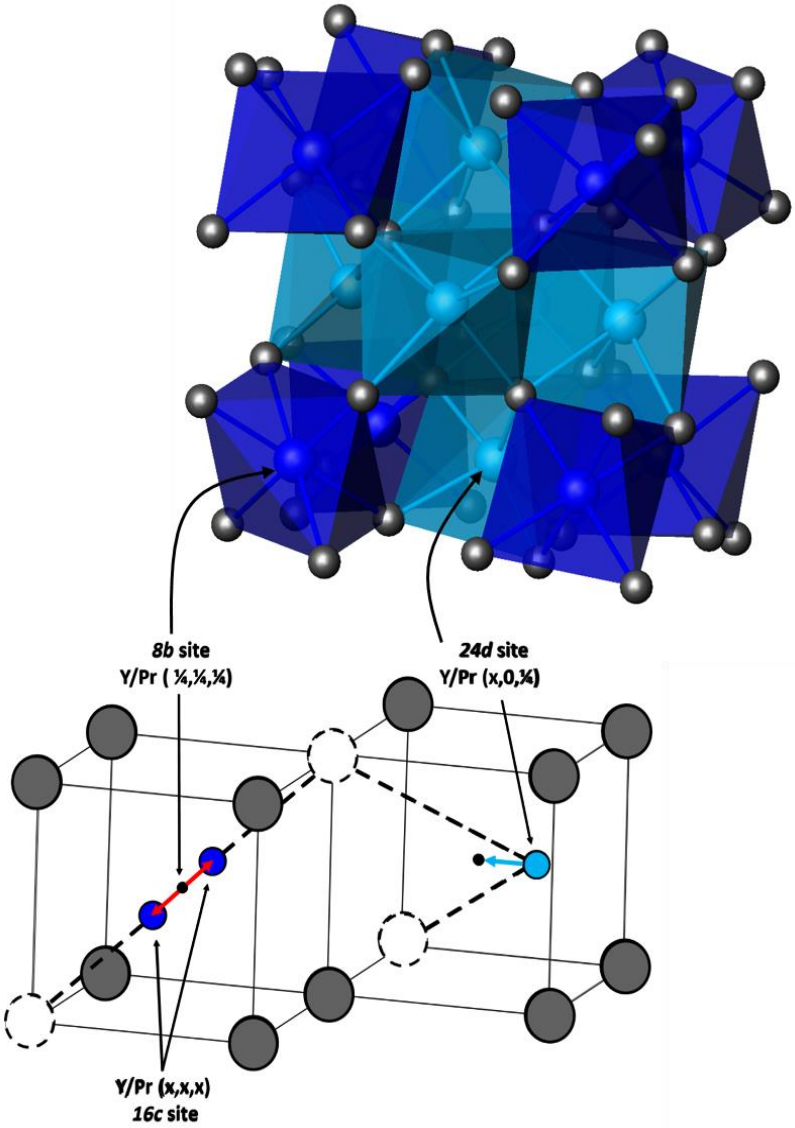

Figure 3.2 Top: Illustration of the bixbyite structure emphasizing the *8b* (dark blue) and *24d* (light blue) cation sites and the oxide (grey) *48e* site. Bottom: Schematic relation between bixbyite A_2O_3 and its oxidized $A_2O_{3+\delta}$ structure. The oxygen positions are illustrated as an idealized cubic fluorite sublattice with the grey positions relating to the *48e* site. The white dashed positions show oxides and vacancies in the partially filled *16c* positions to accommodate the additional oxide anions. The splitting of the *8b* cation site into the *16c* (dark blue) positions and the migration of the *24d* cation position

stoichiometries. *In-situ* powder X-ray diffraction experiments can follow the oxygen uptake and the associated increase in symmetry from bixbyite to fluorite structures. The following detailed structural analyses are only possible because of the beneficial neutron scattering lengths (b(Y) = 7.75 fm, b(Pr) = 4.58 fm and b(O) = 5.803 fm)[12] in conjunction with high resolution synchrotron based x-ray scattering with good form factor contrast. Our simultaneous neutron/X-ray analysis reveals details of the cation and anion sublattices which leads to an in-depth understanding of oxygen distribution and possible cation site splitting.

3.3. Experimental

3.3.1. Synthesis

$Y_{2-x}Pr_xO_{3+\delta}$ samples were prepared from stoichiometric amounts of calcined Y_2O_3 (Cerac, 99.999% purity) and Pr_6O_{11} (Alfa Aesar, 99.996% purity). The starting materials were dissolved in concentrated nitric acid and slowly added to molten citric acid monohydrate (CA, Aldrich, 99% purity). The resulting gel was decomposed on a hotplate overnight, followed by heating to 600°C for 12 hours. The powder was then ground in an agate mortar and heated in air in an alumina crucible at 900°C and 1200°C for 12 hours each (with intermediate grinding), before being cooled slowly to room temperature.

$Y_{2-x}Pr_xO_3$ samples were prepared by reducing $Y_{2-x}Pr_xO_{3+\delta}$ in 5% H_2 (in N_2) flow for 12 hours between 800˚C and 1000˚C.

3.3.2. Powder X-ray Diffraction

3.3.2.1. Room Temperature Laboratory Diffraction

Room temperature powder X-Ray diffraction was carried out using a PANalytical X'Pert Pro diffractometer (PANalytical B.V., Almelo, the Netherlands) in Bragg-Brentano geometry using Cu-Kα radiation ($\lambda(K\alpha_1)$ = 1.540598Å, and $\lambda(K\alpha_2)$ = 1.544426Å), a diffracted beam Ni-filter and a 128 microstrip X'Celerator detector. The samples were mounted as thin layers from acetone slurries onto zero background sample holders (Si(510)) and measured on a PW3040/60 sample spinner stage at 1 revolution per second. Rietveld refinement quality data were collected with 2 hour diffraction data sets in the range of $20° \leq 2\theta \leq 145°$ with 0.0167° steps and 120 seconds per step counting time. Incident beam optics were chosen with 0.04 radians soller slits, 1° divergence slit, 10 mm mask and 2° anti scatter slit. The diffracted beam optics included a 3.4 mm anti scatter slit, 0.04 radian soller slits and a nickel filter. Diffractometer line profiles and peak positions were calibrated using NIST standards LaB_6 SRM 660a and Si SRM 640b.

3.3.2.2. High Temperature In-Situ Powder X-ray Diffraction

In-situ powder X-ray diffraction experiments were carried out using the same PANalytical X'Pert Pro diffractometer as in 2.2.1 equipped with an Anton Paar HTK2000 high temperature furnace attachment. The self-masking furnace uses a 10 mm wide Pt-strip heater and is controlled with a Eurotherm 2604 controller. All data were collected with Cu-Kα radiation ($\lambda(K\alpha_1)$ = 1.540598 Å, and $\lambda(K\alpha_2)$ = 1.544426 Å) using a diffracted beam Ni-filter. 37 minute diffraction data sets were collected over $15° \leq 2\theta \leq 80°$ in 0.0167° steps. The sample was mounted directly onto a platinum strip heater and heated from 25°C to 600°C under flowing 5% hydrogen gas (balance nitrogen). Diffraction patterns were collected every 50°C.

3.3.2.3. Synchrotron X-ray Diffraction

Room temperature high resolution synchrotron diffraction data were collected on $Y_{0.5}Pr_{1.5}O_{3+\delta}$, and $Y_{1.5}Pr_{0.5}O_{3+\delta}$ using beamline 11-BM at the Advanced Photon Source (APS), Argonne National Laboratory, in Argonne, Illinois. The instrument, which is described elsewhere[13] was calibrated using a mixture of NIST standard reference materials; Si (SRM 640c) and Al_2O_3 (SRM 676). Data were collected with an average wavelength of 0.41385Å using 0.001° steps and a scan rate of 0.01° per second. Diffraction data were collected in the range of $0.5° \leq 2\theta \leq 50°$ using a Kapton capillary (ø = 0.8mm) sample holder plugged with wax.

3.3.3. Powder Neutron Diffraction

Time-of-flight neutron Diffraction data were collected on the POWGEN diffractometer at the Spallation Neutron Source (SNS) at Oak Ridge National Laboratory (ORNL) in Oak Ridge, Tennessee. Approximately 0.7 grams of select samples ($Y_{0.5}Pr_{1.5}O_{3+\delta}$, and $Y_{1.5}Pr_{0.5}O_{3+\delta}$) were loaded into an 8mm diameter cylindrical vanadium sample can. A center wavelength of 1.333 Å was used covering a d-spacing from 0.41 Å to 5.37 Å. A slit width of 20 mm and a slit height of 35 mm were used and data were collected for approximately 1 hour each.

3.3.4. Thermal Gravimetric Analysis

Thermal gravimetric analysis (TGA) experiments were conducted using a Linseis Thermowaage L81/1550 thermal balance in vertical measurement arrangement. Samples with masses between 50 mg and 100 mg were placed in alumina crucibles and heated with a rate of 10°C per minute from 25°C to 1000°C in flowing 5% H_2 (balance N_2) in order to reduce them to

$Y_{2-x}Pr_xO_3$. X-ray diffraction was used to confirm reduction and the mass change was used in order to determine oxygen content of each sample (δ). Experiments were all corrected for buoyancy and used an empty alumina crucible as the reference.

3.3.5. Rietveld Refinements

Rietveld refinements were carried out using the *FullProf.2k*[14] software package. Simultaneous refinements against powder synchrotron X-ray and time-of-flight neutron data were carried out for $Y_{1.5}Pr_{0.5}O_{3.19(2)}$ and $Y_{0.5}Pr_{1.5}O_{3.53(2)}$ using equal weights for the X-ray and neutron data. Rietveld refinements against laboratory X-ray diffraction data were performed by first fixing parameters based on results from synchrotron/neutron refinements, allowing instrumental parameters to be established. In order to consistently refine unit cell parameters and atomic positions some parameters were fixed based on these results. Oxygen stoichiometries were not refined, the values determined using thermal gravimetric analysis results, and yttrium to praseodymium ratios were set to synthesized values.

3.4. Results and Discussion

3.4.1. $Y_{2-x}Pr_xO_{3+\delta}$ for $0 \leq x < 2$ Solid Solution Structures

The solid solution of $Y_{2-x}Pr_xO_{3+\delta}$ for $0 \leq x < 2$ was synthesized in air in intervals of $x = 0.1$ based on Lussier et al. [9] All samples prepared in air with $x \geq 1.4$ were obtained as phase-pure (based on X-ray diffraction) cubic fluorite structures (space group: *Fm-3m*, #225). For $x < 1.4$ phase pure bixbyite structures (space group: *Ia-3*, #206) were formed in air. The powder X-ray diffractograms

in figure 3.3 illustrate the gradual intensity losses for the (411), (332), (341) bixbyite (space group *Ia-3*) superstructure peaks as the praseodymium fraction is increased to x=1.4. For x ≥ 1.4 the bixbyite superstructure peaks are no longer present thus indicating the formation of fluorite structures. The yttrium and praseodymium cations are fully disordered over the 2 cation sites (*8b* and *24d* sites) in the bixbyite phases.

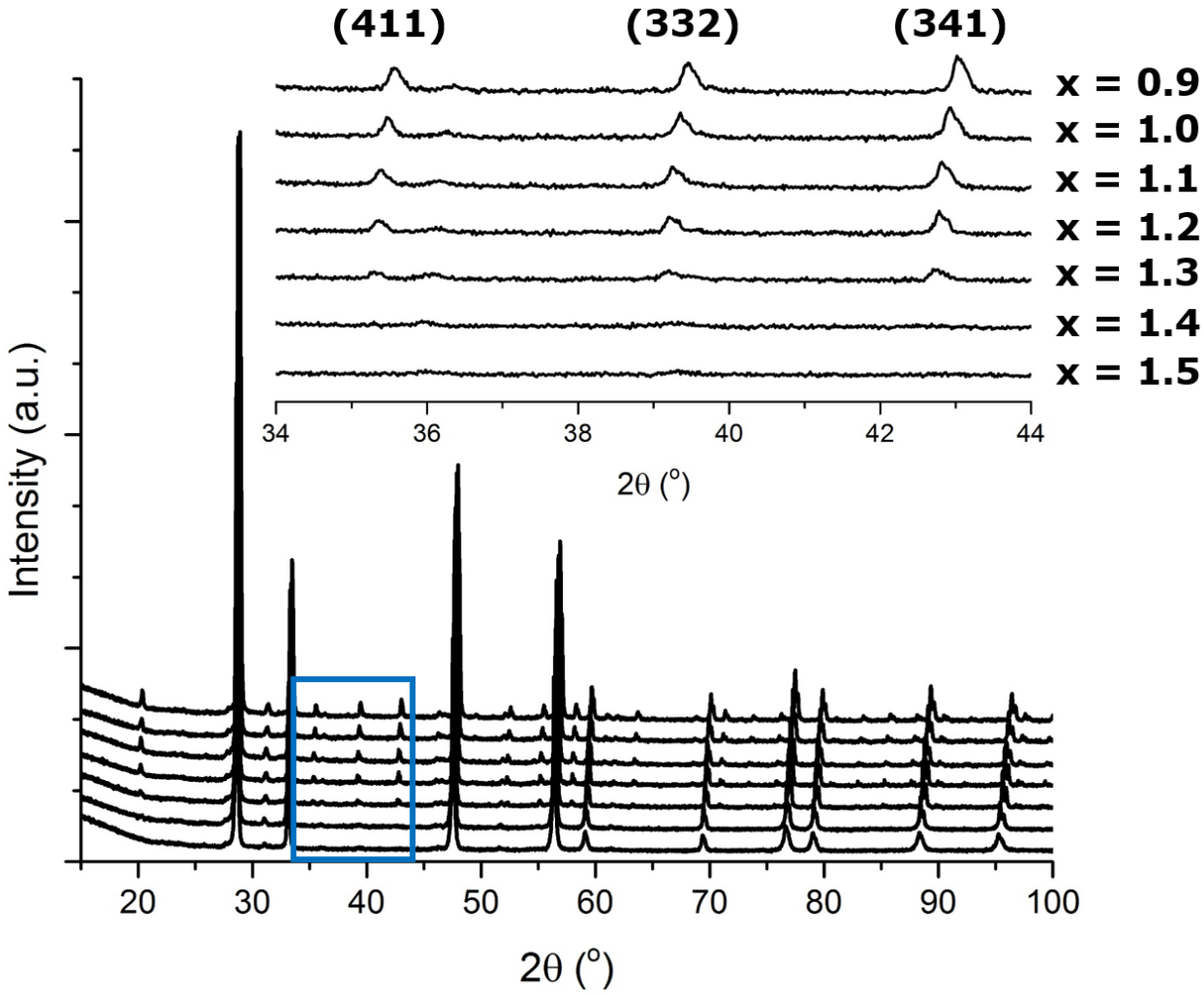

Figure 3.3 Room temperature powder X-ray diffractograms of $Y_{2-x}Pr_xO_{3+\delta}$. The insert emphasizes the disappearance of the bixbyite superstructure peaks with increasing praseodymium content.

Figure 3.4 shows the Rietveld plots of the synchrotron X-ray and time of flight neutron data for $Y_{1.5}Pr_{0.5}O_{3.19(2)}$. Table 3.1 summarizes the structural details of the bixbyite phase $Y_{1.5}Pr_{0.5}O_{3.19(2)}$ and the fluorite phase $Y_{0.5}Pr_{1.5}O_{3.53(2)}$. In agreement with the previously published $YPrO_{3.43(2)}$ structure[9] the $Y_{1.5}Pr_{0.5}O_{3.19(2)}$ bixbyite phase (*Ia-3*) shows a fully occupied oxygen *48e* site and a partially filled oxygen *16c* site. Yttrium and praseodymium are fully disordered over the two cation sites, namely the *24d* site and the *16c* split site (splitting of the original *8b* site). $Y_{0.5}Pr_{1.5}O_{3.53(2)}$ is a fully yttrium/praseodymium cation and oxygen/ vacancy disordered fluorite structure with no indication of any deviations from the high symmetry *(Fm-3m)* structure. In figure 3.5 representative Rietveld plots based on laboratory powder X-ray diffraction data for selected "as-prepared" and corresponding reduced $Y_{2-x}Pr_xO_{3+\delta}$ members are shown.

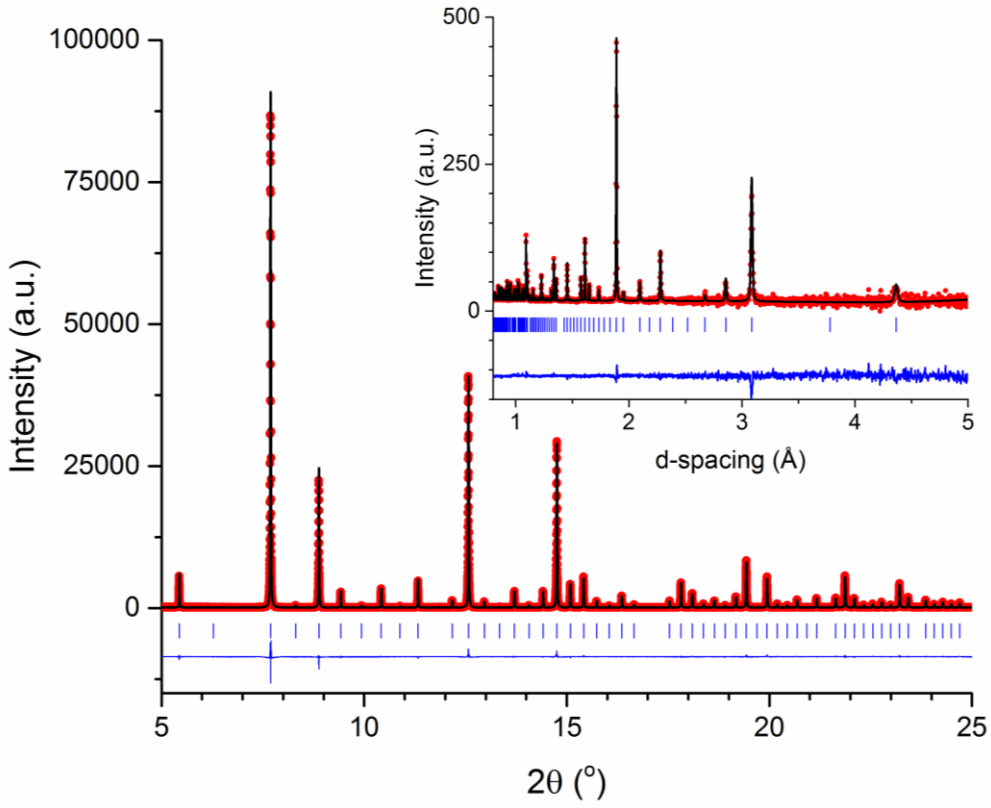

Figure 3.4 Rietveld plot of the simultaneous refinement of the $Y_{1.5}Pr_{0.5}O_{3.19(2)}$ structure using powder synchrotron X-ray (main) and time of flight neutron (insert) data.

Table 3.1 Room temperature structural parameters for the cubic bixbyite $Y_{1.5}Pr_{0.5}O_{3.19(2)}$ and the cubic defect fluorite $Y_{0.5}Pr_{1.5}O_{3.53(2)}$ phases, obtained from simultaneous Rietveld refinement against synchrotron powder X-ray diffraction and time-of-flight powder neutron data.

Composition		**$Y_{1.5}Pr_{0.5}O_{3.19(2)}$**	**$Y_{0.5}Pr_{1.5}O_{3.53(2)}$**
space group		$Ia\bar{3}$ (206)	$Fm\bar{3}m$ (225)
unit cell	a (Å) V (Å^3) Z V/Z (Å^3)	10. 68813(4) 1220.972(12) 16 76.3107(7)	5.42208 (3) 159.404(3) 2 79.702(2)
Y/Pr (*16c*) (x, x, x)	x/a β(11)/ β(22)/ β(33) β(12)/ β(13)/ β(23)	0.2414(2) 0.00142 (11) 0.00083 (10)	
Y/Pr (*24d*) (x, 0, ¼)	x/a B_{iso} (Å^2)	-0.02535 (23) 0.746 (35)	
O (*48e*) (x, y, z)	x/a y/b z/c Occupancy (%) B_{iso} (Å^2)	0.38696 (94) 0.14926 (88) 0.38042 (99) 101 (3) 0.86 (12)	
O (*16c*) (x, x, x)	x/a Occupancy (%) B_{iso} (Å^2)	0.8899 (53) 17 (3) 0.86 (12)	
Y/Pr (*4a*) (0, 0, 0)	B_{iso} (Å^2)		1.21(7)
O (*8c*) (¼,¼,¼)	Occupancy (%) B_{iso} (Å^2)		88 2.33 (40)
χ^2:	Neutron (T.O.F.)[a] X-ray (λ=0.4138 Å)[b]	2.50 1.36	3.66 4.76

[a]Neutron T.O.F range: 13200 – 110417 μs, 2663 data points
[b]X-ray λ=0.41385 Å, $3.75° \leq 2\theta \leq 49.99°$, $\Delta 2\theta = 0.001°$, 46240 data points

The volumes per formula unit, V/Z, as derived from Rietveld refinements for the solid solution $Y_{2-x}Pr_xO_{3+\delta}$ for $0 \leq x < 2$ are presented in figure 3.6. The volumes for the reduced samples ($Y_{2-x}Pr_xO_3$ for $0 \leq x < 2$) increases linearly with the praseodymium concentration as expected from the ionic radii of Pr^{3+}(VI) = 0.99 Å and Y^{3+}(VI)) = 0.9 Å[15] in agreement with Vegard's law. Y_2O_3[16] is stable as a bixbyite phase but Pr_2O_3[17] forms a trigonal structure. Since all reduced $Y_{2-x}Pr_xO_3$ samples were prepared from the oxidized bixbyite and fluorite phases by topotactic reduction in dilute hydrogen only reduced bixbyite phases were obtained.

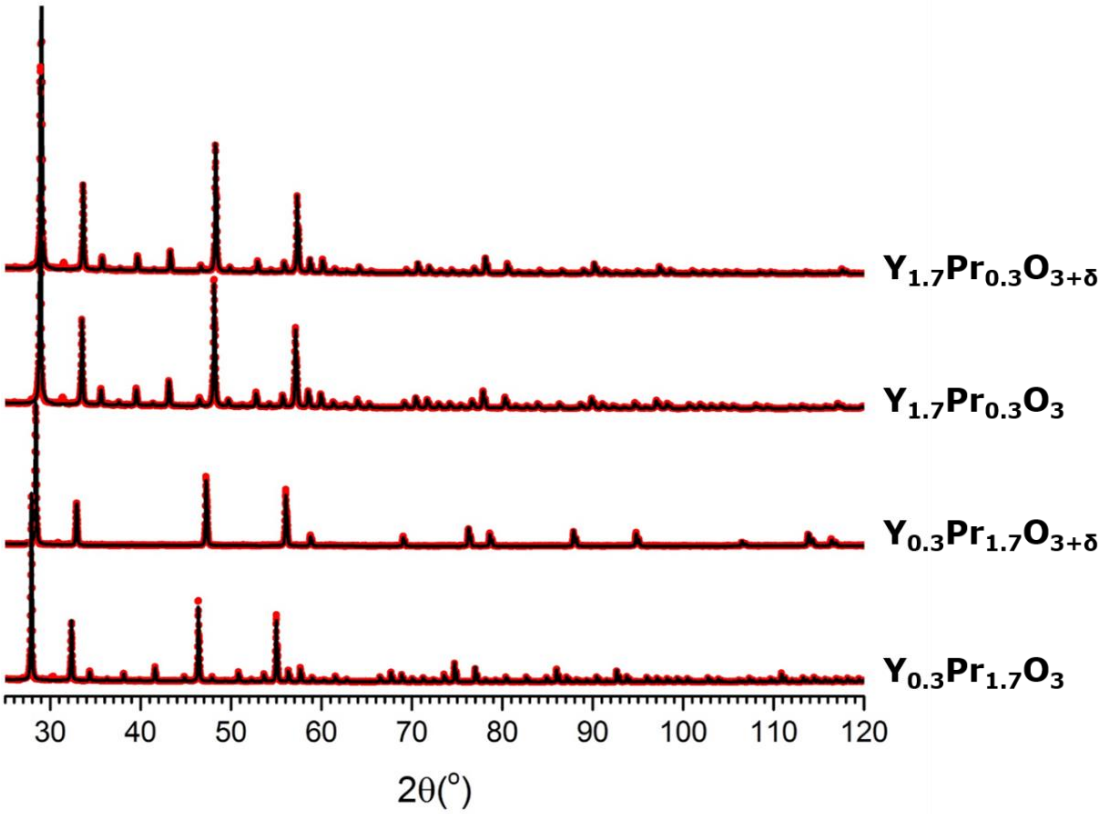

Figure 3.5 Example Rietveld refinement plots of $Y_{(2-x)}Pr_xO_{3+\delta}$ using laboratory based powder X-ray diffraction data.

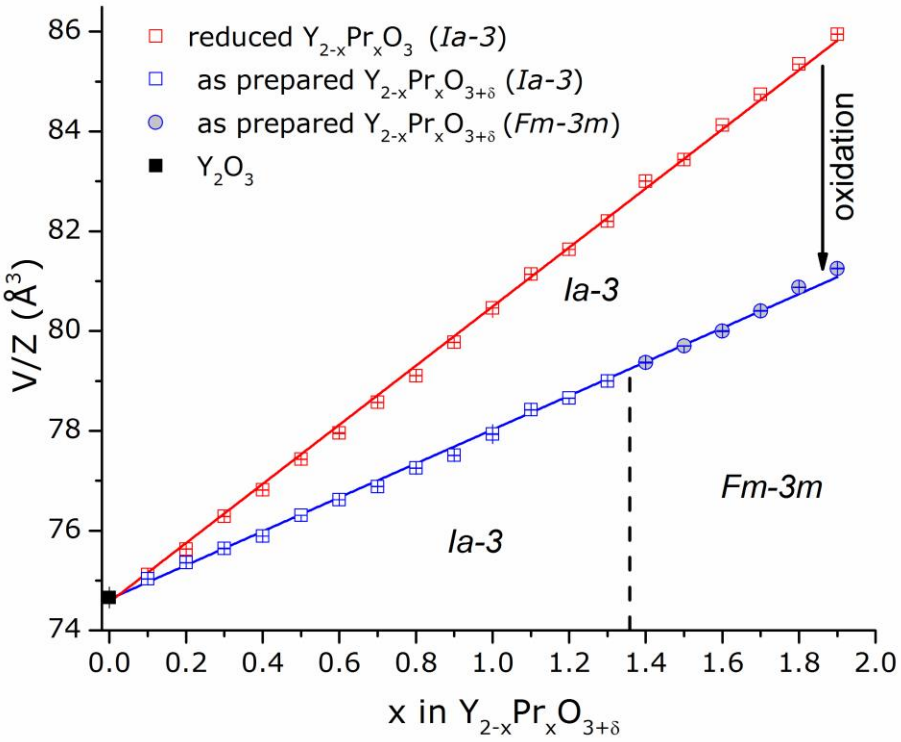

Figure 3.6 Volume per formula unit as a function of Pr content and oxygen content in $Y_{2-x}Pr_xO_{3+\delta}$. The volume decreases during oxidation but the additional oxygen compensates for the expected volume contraction as a function of praseodymium content.

The “as-prepared” samples are oxidized phases with +4 being the predominant oxidation state for praseodymium as determined by TGA and confirmed with magnetic measurements.[9] The oxidized samples also show a linear increase of V/Z as a function of the praseodymium concentration for the bixbyite and fluorite structures. Notably no discontinuity is observed at the bixbyite – fluorite boundary which agrees with the structural similarities of the bixbyite and fluorite structures. The volume evolution for the oxidized phases $Y_{2-x}Pr_xO_{3+\delta}$ for $0 \leq x < 2$ depends on the cation sizes and ratios as well as the oxygen stoichiometry. Based on the cation sizes ($r(Pr^{4+}(VI)) = 0.85$ Å $< r(Y^{3+}(VI)) = 0.9$ Å)[15] a volume contraction would be expected for larger praseodymium concentrations. This contraction is compensated for by the simultaneously increasing oxygen concentrations. This formula unit volume decrease during oxidation for fixed praseodymium concentrations is in contrast to the volume expansion during oxidation of the 3d-transition metal analogues $ScVO_{3+\delta}$, $InVO_{3+\delta}$ and $ScTiO_{3+\delta}$.[18–20]

3.4.2. Y/Pr *24d*-site Relaxation in Oxidized Bixbyite Phases

The (411), (332), (341) bixbyite superstructure peaks highlighted in figure 3.3 are very sensitive to the x-parameter of the *24d* site (x, 0, ¼). Figure 3.7 shows the refined x-coordinate for the *24d* position as a function of praseodymium content in $Y_{2-x}Pr_xO_{3+\delta}$ for $0 \leq x < 2$ as obtained from Rietveld refinements. Since no bixbyite superstructure peaks are measurable for $Y_{2-x}Pr_xO_{3+\delta}$ samples with $x > 1.4$ the *24d* cations are fixed to (0,0,¼). The crystal structure for $x = 1.4$ was refined using both a bixbyite and a fluorite setting and both values are shown on figure 3.7. As expected, the *24d* x-parameter increases towards the ideal fluorite position as Pr^{4+} replaces Y^{3+} which is accompanied by oxide addition to the *16c* position. The *24d* site x-coordinate increases nearly linearly from $Y_{1.9}Pr_{0.1}O_{3+\delta}$ to $Y_{0.8}Pr_{1.2}O_{3+\delta}$. From $Y_{0.8}Pr_{1.2}O_{3+\delta}$ to $Y_{0.6}Pr_{1.4}O_{3+\delta}$ a sudden shift

of the *24d* cations toward the ideal fluorite position is observed. This indicates a large sensitivity of the *24d* site close at the threshold between the bixbyite and the fluorite structure. It is noted that the unit cell dimension evolution does not show this behavior (figure 3.6). For comparison, the x-coordinates for the bixbyite *24d* positions of all reduced samples are also included in the figure, and show only a very small change with respect to the Pr concentration. All reduced samples crystallize in the bixbyite structure.

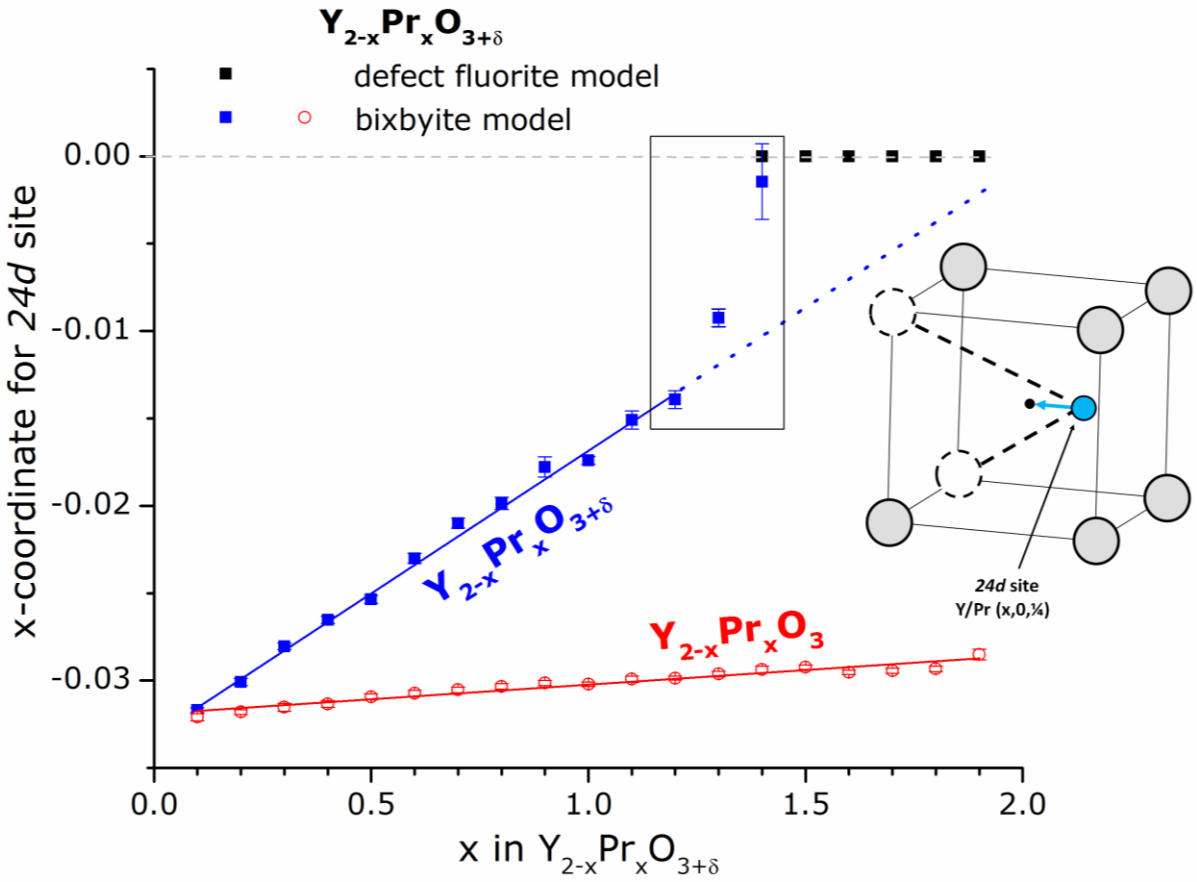

Figure 3.7 Evolution of the Y/Pr *24d* site x-coordinate in the bixbyite structure (*Ia-3*) as a function of Pr content. Blue symbols = $Y_{2-x}Pr_xO_{3+\delta}$ bixbyite (as prepared in air), black symbols = $Y_{2-x}Pr_xO_{3+\delta}$ fluorite (as prepared in air), red symbols = $Y_{2-x}Pr_xO_3$ bixbyite (fully reduced). The solid lines are linear fits to guide the eye and the dotted line is an extrapolation. The open rectangle emphasizes the regime with the largest deviation from the linear relation for $Y_{2-x}Pr_xO_{3+\delta}$. The insert illustrates the migration of the *24d* site towards the fluorite equivalent position (0,0,¼) with increasing praseodymium concentrations.

3.4.3. Site Splitting on the *8b* Cation Position

It has been shown that $YPrO_3$ is a bixbyite phase with Y/Pr disorder on the *8b* and *24d* sites; whereas, in the oxidized $YPrO_{3.43}$ the *8b* site undergoes site splitting by moving the disordered cations off the fully occupied *8b* position (¼,¼,¼) to the half occupied *16c* position (x,x,x), thus moving the cations closer to the additional oxide ions on the invoked *16c* site.[9] Here we are following the site splitting and quantify the shift from the *8b* (¼,¼,¼) to the *16c* (¼+Δx,¼+Δx,¼+Δx) position as a function of Pr^{4+} concentration. The *8b* cation position (¼,¼,¼), of all members of the solid solution up to x = 1.3, were allowed to freely refine into the *16c* position (x,x,x). Figure 3.8 shows the atomic coordinates for the *16c* split position against the Pr-stoichiometry. In pure Y_2O_3 yttrium is located at the ideal (¼,¼,¼) position. Site splitting is observed even with minimal praseodymium content ($Y_{1.9}Pr_{0.1}O_{3+\delta}$) with the largest site splitting being observed for $Y_{1.1}Pr_{0.9}O_{3+\delta}$. Addition of praseodymium beyond $Y_{1.1}Pr_{0.9}O_{3+\delta}$ results in less pronounced site splitting and at $Y_{0.6}Pr_{1.4}O_{3+\delta}$ and larger praseodymium fractions no site splitting is present. At x = 1.4 the cubic fluorite structure is formed. For a Y:Pr ratio of approximately 1:1 that the anion *16c* position will be almost half filled, which will pull the cation towards the filled position, and away from the hole.[9] For praseodymium richer samples more oxide anions are added which will fill the remaining vacancies on the *16c* anion site therefore pulling the cation back towards the ideal *8b* position. Therefore the shift back towards (¼,¼,¼) is expected, due to the higher probability of the cation being found coordinated to 8 oxide anions rather than 7.

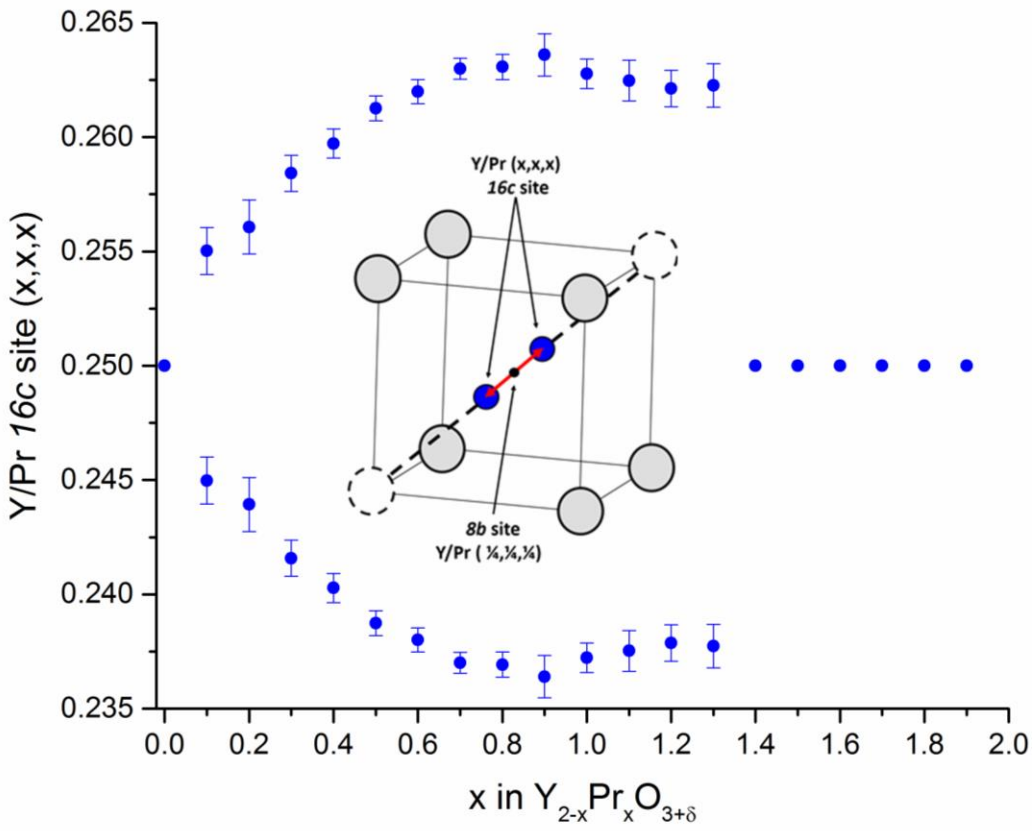

Figure 3.8 *8b* site splitting into *16c* as a function of praseodymium concentration. The insert illustrates the migration from the fully occupied *8b* site into the half occupied *16c* site. The Pr rich $Y_{2-x}Pr_xO_{3+\delta}$ members with x > 1.3 crystallize in the fluorite structure with no site-splitting.

3.4.4. *In-situ* Reduction of $Y_{0.1}Pr_{1.9}O_{3+\delta}$

A deeper understanding of the reduction of the fluorite phases can be gained from *in-situ* diffraction studies. The contour plot shown in figure 3.9 illustrates the structural changes of $Y_{0.1}Pr_{1.9}O_{3+\delta}$ during reduction in 5% hydrogen (balanced with nitrogen) while heating in 50˚C increments. The starting material (x = 1.9) is a cubic defect fluorite structure with no bixbyite superstructure peaks. Up to 300°C only thermal expansion is observed. Above 300 °C the diffraction peaks shift rapidly to higher d-spacings as the reduction occurs. Between 350 °C and 500 °C the defect fluorite structure is reduced to a bixbyite phase. Figure 3.10 emphasizes a

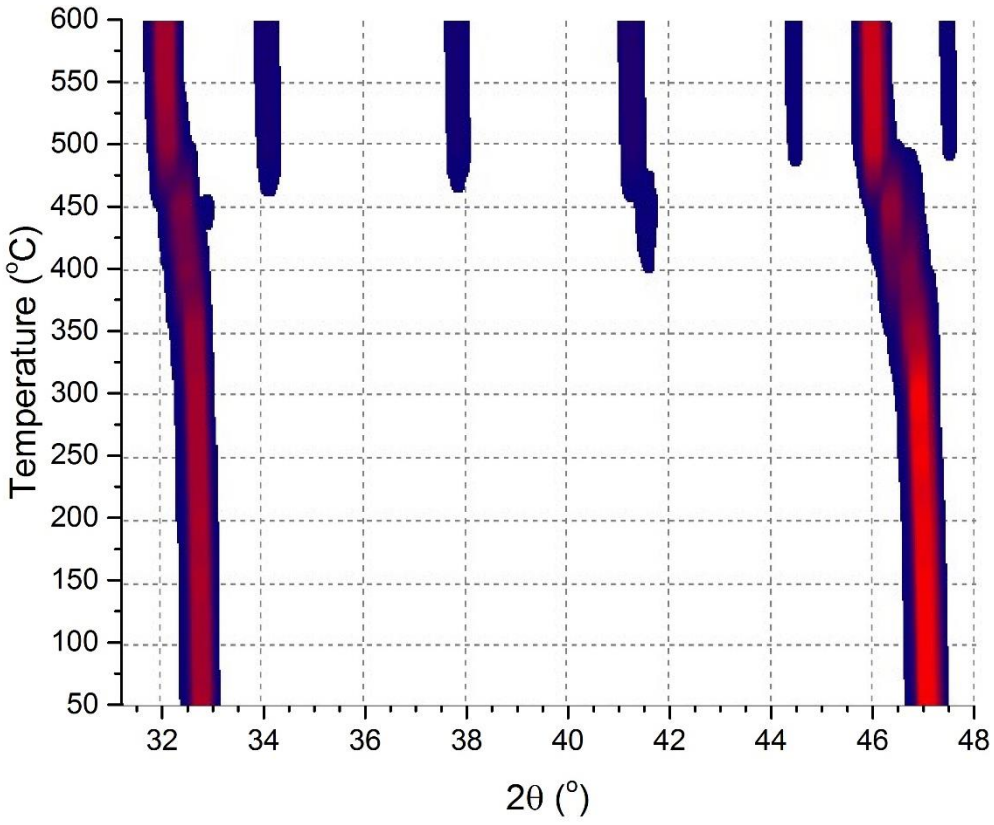

Figure 3.9 Contour plot of *in-situ* X-ray diffraction data during the reduction of $Y_{0.1}Pr_{1.9}O_{3+\delta}$ (fluorite) to $Y_{0.1}Pr_{1.9}O_3$ (bixbyite) in flowing 5% H_2 gas. The bixbyite phase starts to form at approximately 400˚C as indicated by the occurrence of the bixbyite superstructure peaks.

temperature dependent diffraction peak clearly illustrating the coexistence of 2 phases at 400˚C and 450˚C, namely a defect fluorite and a bixbyite structure. This is supported by the growth of a single set of bixbyite superstructure peaks at these temperatures. In contrast the main peaks that are common to the bixbyite and fluorite structures are double peaks. The reduction is completed at 500°C and only thermal expansion is observed beyond that temperature. Focusing on the (440) bixbyite and (220) fluorite peak in figure 3.10 reveals the transition at 400°C and 450°C. From these diffraction peaks one can begin to understand the reduction in a more mechanistic sense. The minimum oxygen content for $Y_{0.1}Pr_{1.9}O_{3+\delta}$ as a defect fluorite will first be realized, at which point the transition to a bixbyite structure will slowly commence. Once the defect fluorite structure is

depleted, the new oxygen-rich bixbyite will begin to lose oxygen until fully reduced. Comparing the reduction temperature to that found for $YPrO_3$[9] the onset and completion of the reduction occurs at similar temperatures. Because the bixbyite and fluorite structures are so closely related, despite a loss of symmetry and a slightly more pronounced structural change, the topotactic reduction can still occur at low temperatures.

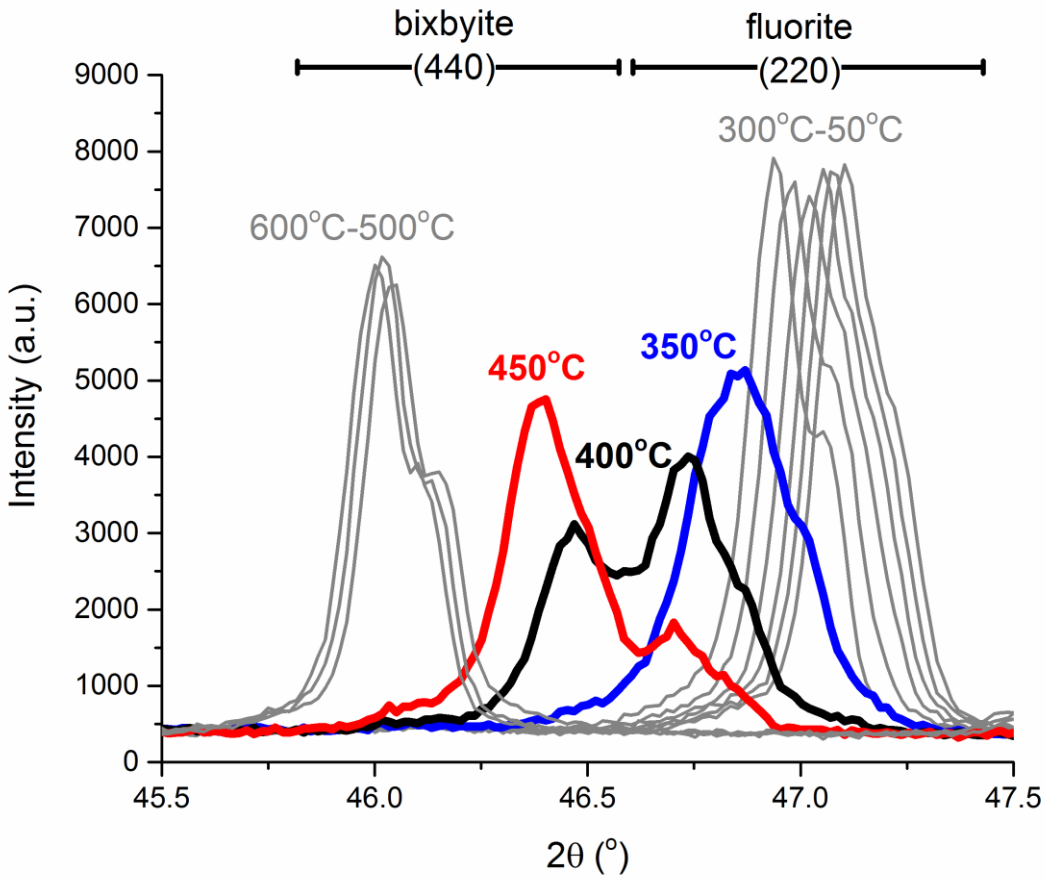

Figure 3.10 Selected powder X-ray diffraction peaks during *in-situ* reduction of $Y_{0.1}Pr_{1.9}O_{3+\delta}$ (fluorite) to $Y_{0.1}Pr_{1.9}O_3$ (bixbyite) in flowing 5% H_2 gas. The 350 to 450˚C data clearly illustrate the coexistence of 2 phases at the reductive structural transition.

3.5. Conclusions

The $Y_{(2-x)}Pr_xO_{3+\delta}$ ($0.0 \leq x < 2$ and $0 \leq \delta < 1$) solid solution is ideal for deciphering the bixbyite-fluorite oxidation and reduction mechanism. We have illustrated the cation site responses for the partially oxidized bixbyite phases $Y_{(2-x)}Pr_xO_{3+\delta}$ ($0.0 \leq x < 1.4$ and $0 \leq \delta < 0.53$) and the occurrence of fluorite phases for $Y_{(2-x)}Pr_xO_{3+\delta}$ ($1.4 \leq x < 2$ and $0.53 \leq \delta < 0.6$). The defect fluorite phases are fully disordered on the cation and anion sites. The bixbyite phases accommodate excess oxygen in the additionally invoked *16c* anion site in space group *Ia-3*. In response to this site preference, the *8b* cation site splits into a *16c* site in order to form seven nearly equal and one elongated bond. It is suggested that this will inhibit the oxide ion mobility despite the presence of oxide defects. The *24d* cation moves towards the ideal fluorite position as the samples become progressively more oxidized. It should be noted that all oxidized samples in the investigated series are single phase and that the formula unit volume increases linearly with the praseodymium content. The *in-situ* reductions only show coexisting fluorite and bixbyite phases in a narrow temperature range. $Y_{(2-x)}Pr_xO_{3+\delta}$ is an ideal model system for the investigation of oxide defect formation and annihilation.

References

(1) Fergus, J. W. Electrolytes for Solid Oxide Fuel Cells. *J. Power Sources* **2006**, *162* (1), 30–40.

(2) Goodenough, J. B. Ceramic Technology: Oxide-Ion Conductors by Design. *Nature* **2000**, *404* (6780), 821–823.

(3) Bevan, D. J. M.; Martin, R. L. The Role of the Coordination Defect: A New Structural Description of Four Fluorite-Related Sesquioxide Minerals, Bixbyite (Mn_2O_3), Braunite (Mn_7SiO_{12}), Braunite II ($CaMn_{14}SiO_{24}$), Parwelite ($Mn_{10}Sb_2As_2Si_2O_{24}$), and Their Structural Relationships. *J. Solid State Chem.* **2008**, *181* (9), 2250–2259.

(4) Giussani, A.; Zaumseil, P.; Seifarth, O.; Storck, P.; Schroeder, T. A Novel Engineered Oxide Buffer Approach for Fully Lattice-Matched SOI Heterostructures. *New J. Phys.* **2010**, *12* (9), 93005.

(5) Seifarth, O.; Dietrich, B.; Zaumseil, P.; Giussani, A.; Schroeder, T.; Storck, P. Integration of Strained and Relaxed Silicon Thin Films on Silicon Wafers via Engineered Oxide Heterostructures: Experiment and Theory. *IEEE Trans. Power Syst.* **1993**, *8* (3), 1366–1374.

(6) Seifarth, O.; Schubert, M. A.; Giussani, A.; Klenov, D. O.; Schmeier, D.; Schroeder, T. Single Crystalline $Pr_{2-x}Y_xO_3$ (x = 0-2) Dielectrics on Si with Tailored Electronic and Crystallographic Structure. In *Journal of Applied Physics*; American Institute of Physics (AIP), 2010; Vol. 108, p 103709.

(7) Niu, G.; Zoellner, M. H.; Zaumseil, P.; Pouliopoulos, A.; D'Acapito, F.; Schroeder, T.; Boscherini, F. X-Ray Diffraction and Extended X-Ray Absorption Fine Structure Study of

Epitaxial Mixed Ternary Bixbyite $Pr_xY_{2-x}O_3$ (x = 0–2) Films on Si (111). *J. Appl. Phys.* **2013**, *113* (4), 43504.

(8) Kimmel, G.; Zabicky, J.; Goncharov, E.; Mogilyanski, D.; Venkert, A.; Bruckental, Y.; Yeshurun, Y. Formation and Characterization of Nanocrystalline Binary Oxides of Yttrium and Rare Earths Metals. *J. Alloys Compd.* **2006**, *423* (1–2), 102–106.

(9) Lussier, J. A.; Szkop, K. M.; Sharma, A. Z.; Wiebe, C. R.; Bieringer, M. Order/Disorder and in Situ Oxide Defect Control in the Bixbyite Phase $YPrO_{3+\delta}$ ($0 \leq \delta < 0.5$). *Inorg. Chem.* **2016**, *55* (5), 2381–2389.

(10) Rajendran, M.; Mallick, K. K.; Bhattacharya, A. K. Preparation and Characterization of $LnPrO_{(3+y)}$ (Ln = Y and Lanthanide) - a Series of Mixed Lanthanide Oxides. *Mater. Lett.* **1998**, *37* (1–2), 10–16.

(11) Rajendran, R.; Krishna, M. G.; Mallick, K. K.; Bhattacharya, A. K. Structure, Oxygen Stoichiometry and Electrical Conductivity of $LnPrO_{(3+y)}$ (Ln = Y and Lanthanide) Oxides. *Mater. Sci. Eng.* **1999**, *58B* (3), 215–220.

(12) Sears, V. F. Neutron Scattering Lengths and Cross Sections. *Neutron News* **1992**, *3* (3), 26–37.

(13) Wang, J.; Toby, B. H.; Lee, P. L.; Ribaud, L.; Antao, S. M.; Kurtz, C.; Ramanathan, M.; Von Dreele, R. B.; Beno, M. A. A Dedicated Powder Diffraction Beamline at the Advanced Photon Source: Commissioning and Early Operational Results. *Rev. Sci. Instrum.* **2008**, *79* (8), 1–7.

(14) Rodriguez-Carvajal, J. FullProf.2K. Full Prof 2K V. 4.40 2013.

(15) Shannon, R. D. Revised Effective Ionic Radii and Systematic Studies of Interatomic Distances in Halides and Chalcogenides. *Acta Crystallogr.* **1976**, *A32* (5), 751–767.

(16) Heiba, Z. K.; Arda, L. X-Ray Diffraction Analysis of Powder and Thin Film of $(Gd_{1-x}Y_x)_2O_3$. *Cryst. Res. Technol.* **2008**, *43* (3), 282–288.

(17) Rudenko, V. S.; Boganov, A. G. Reduction Cycle MO_2 - M_2O_3 for Cerium, Praseodymium, and Terbium Oxides. *Inorg. Mater.* **1970**, *6* (12), 1893–1898.

(18) Shafi, S. P.; Lundgren, R. J.; Cranswick, L. M. D.; Bieringer, M. Formation, Structure and Magnetism of the Metastable Defect Fluorite Phases $AVO_{3.5+x}$ (A = In, Sc). *J. Solid State Chem.* **2007**, *180* (12), 3333–3340.

(19) Lundgren, R. J.; Cranswick, L. M. D.; Bieringer, M. In Situ X-Ray Powder Diffraction, Synthesis, and Magnetic Properties of $InVO_3$. *J. Solid State Chem.* **2006**, *179* (12), 3599–3606.

(20) Shafi, S. P.; Hernden, B. C.; Cranswick, L. M. D.; Hansen, T. C.; Bieringer, M. Topotactic Oxidation Pathway of $ScTiO_3$ and High-Temperature Structure Evolution of $ScTiO_{3.5}$ and $Sc_4Ti_3O_{12}$-Type Phases. *Inorg. Chem.* **2012**, *51* (3), 1269–1277.

Chapter 4. Structure Evolution and Reactivity of the $Sc_{(2-x)}VxO_{3+\delta}$ ($0 \leq x \leq 2.0$) System

Joey A. Lussier [a], Fabian J. Simon [a,†], Pamela S. Whitfield [b,‡], Kalpana Singh [c], Venkataraman Thangadurai [c], Mario Bieringer [a,d]

[a] Department of Chemistry, University of Manitoba, Winnipeg, MB, R3T 2N2, Canada

[b] Spallation Neutron Source, Oak Ridge National Laboratory, Oak Ridge, Tennessee 37830, USA

[c] Department of Chemistry, University of Calgary, Calgary, Alberta, T2N 1N4, Canada

[d] Manitoba Institute for Materials, University of Manitoba, Winnipeg, MB, R3T 2N2, Canada

[†] current address: Institute of Physical Chemistry & Center for Materials Research, Justus-Liebig-University Giessen, 35392 Giessen, Germany

[‡] Current address: Excelsus Structural Solutions, Park Innovaare, 5234 Villigen, Switzerland

First Published in Inorganic Chemistry, April 17th, 2018 Article ASAP

DOI: 10.1021/acs.inorgchem.8b00571

Preface

This manuscript, which was published by Inorganic Chemistry, explores the structural diversity of the $Sc_{2-x}V_xO_{3+\delta}$ system. In preliminary studies, $ScVO_{3+\delta}$ was found to be a good candidate for fast ion conduction, however, the low temperature oxidative transformation to $ScVO_4$ negatively impacts the ionic conductivity making this material a poor candidate for use as a solid-state electrolyte. In an attempt to find a more suitable candidate the full series was synthesized. This manuscript reports the synthesis, structure, and high temperature reactivity of the full series. It was accepted to Inorganic Chemistry and published online April 17th, 2018.

Contributions

Preliminary synthesis and oxidative studies of the scandium-rich ($x \leq 1.0$) portion of the series was explored by Fabian J. Simon. Synthesis of the full series, measurements, and analysis were completed by Joey A. Lussier. Pamela S. Whitfield helped with Rietveld refinements, and Kalpana Singh performed conductivity measurements. The manuscript was written by Joey A. Lussier and Mario Bieringer.

4.1. Abstract

Solid oxide fuel cells (SOFCs) are solid-state electrochemical devices, which directly convert chemical energy of fuels into electricity with high efficiency. Due to their fuel flexibility, low emissions, high conversion efficiency, no moving parts, and quiet operation, they are considered as a promising energy conversion technology for low carbon future needs. Solid-state oxide and proton conducting electrolytes play a crucial role in improving the performance and market acceptability of SOFCs. Defect fluorite phases are some of the most promising fast ion conductors for use as electrolytes in solid oxide fuel cells. We report the synthesis, structure, phase diagram, and high temperature reactivity of the $Sc_{2-x}V_xO_{3+\delta}$ ($0 \leq x \leq 2.00$) oxide defect model system. For all $Sc_{2-x}V_xO_{3.0}$ phases with $x \leq 1.08$ phase pure bixbyite-type structures are found, whereas for $x \geq 1.68$ phase pure corundum structures are reported, with a miscibility gap where $1.08 < x < 1.68$. Structural details obtained from the simultaneous Rietveld refinements using powder neutron and X-ray diffraction data are reported for the bixbyite phases, demonstrating a slight V^{3+} preference towards the *8b* site. In-situ X-ray diffraction experiments were used to explore the oxidation of the $Sc_{2-x}V_xO_{3.0}$ phases. In all cases $ScVO_4$ was found as a final product, accompanied by Sc_2O_3 for $x < 1.0$ and V_2O_5 when $x > 1.0$; however, the oxidative pathway varied greatly throughout the series. Comments are made on different synthesis strategies, including the effect on crystallinity, reaction times, rate limiting steps, and reaction pathways. This work provides insight into the mechanisms of solid-state reactions, and strategic guidelines for targeted materials synthesis.

4.2. Introduction

The AVO_3 (trivalent vanadium) and AVO_4 (pentavalent vanadium) systems where A represents trivalent cations (Sc, In, Y, and rare earths: La-Lu) have been of great interest to the scientific community due to their diverse physical and structural properties. The interesting electronic,[1,2] optical,[3,4] and magnetic[5–8] properties include low temperature magnetic field-dependent spin reversal,[9] multiferroicity,[10] and successive crystallographic and magnetic transitions.[11] Furthermore potential applications as secondary lithium ion batteries,[12] laser host materials,[13] and photocatalysts[14] have been proposed.

These V^{3+} based compounds crystallize mainly as either perovskites or bixbyite phases. The A^{3+} size dependent phase formations are in agreement with the commonly used Goldschmidt tolerance factor. When the ionic radius of A^{3+} is smaller than Lu^{3+}, a bixbyite is typically found, whereas Lu^{3+} and larger A^{3+} cations crystallize as perovskite phases.[15–17] AVO_4 materials with the small pentavalent vanadium cation (V^{5+}) tend to crystallize in the tetragonal zircon phase, isostructural with $ZrSiO_4$.

The scandium – vanadium – oxygen phase diagram shows a variety of structure types and oxygen compositions including bixbyites, fluorites, pyrochlores, and a Sc_2VO_5 phase.[18–23] The redox chemistry of these AVO_x compounds can be found in the literature[16,17,24,25] where the oxidation and reduction pathways of the AVO_3 bixbyite to AVO_4 zircon are described in detail. The redox chemistry is of particular interest due to the structural relationship between the bixbyite, fluorite, and zircon structures. Figure 1 shows these three structures and outlines the redox chemistry reported for the oxidation/reduction of $ScVO_3$ – $ScVO_4$.[16,24] The bixbyite structure crystallizes in space group *Ia-3* and can be described as a cubic ordered oxide defect structure and

is closely related to the fluorite structure. In the bixbyite structure the cations are typically fully disordered on the *8b* and 24*d* sites with a quarter of the oxide anions missing (with respect to the fluorite structure). The oxide anions are found in a fully occupied *48e* site. In the bixbyite structure all cations are 6-fold coordinated with oxide anions. The fluorite structure crystallizes in the cubic *Fm-3m* space group with only one cation site, *4a,* and one anion site, *8c*. The resulting AO_8 cubes form a 3-dimensional edge forming a checker board pattern. The defect fluorite structure is well known for its high ionic conductivity, which is a desirable property for solid-state electrolytes used in solid oxide fuel cells.[12,26] In contrast, the conductivity of corresponding zircon phases tend to be low. The tetragonal zircon structure crystallizes in the space group $I4_1/amd$, where the cations are ordered and found in either the *4a* site (larger cation), or *4b* site (smaller cation) and the anions are located in the *16h* site. In zircon phases the smaller cation forms tetrahedra, whereas the larger cation is bound to 8 anions, forming dodecahedra.

Notably when we deviate from the 1:1 cation ratio, the oxidation of scandium rich bixbyite phases will result in the formation of $ScVO_4$ zircon with Sc_2O_3 as a byproduct. In hydrogen $ScVO_4$ will reduce to $ScVO_3$ bixbyite. Only during prolonged heating at very high temperatures will $ScVO_3$ and the excess Sc_2O_3 form single phase scandium rich bixbyite structures again.

The rhombohedral corundum structure with the cations located in the *12c* and the anions in the *18e* sites consists of AO_6 octahedra. Here we will show that the corundum structure does not allow to be oxidized via a topotactic route. Instead the Sc-V-O corundum phase oxidizes directly to the zircon structure while expelling vanadium oxide phases. The reduction of $ScVO_4$ does not result in a corundum structure, the Sc:V ratio of 1:1 favors the formation of the $ScVO_3$ bixbyite phase instead during reduction.

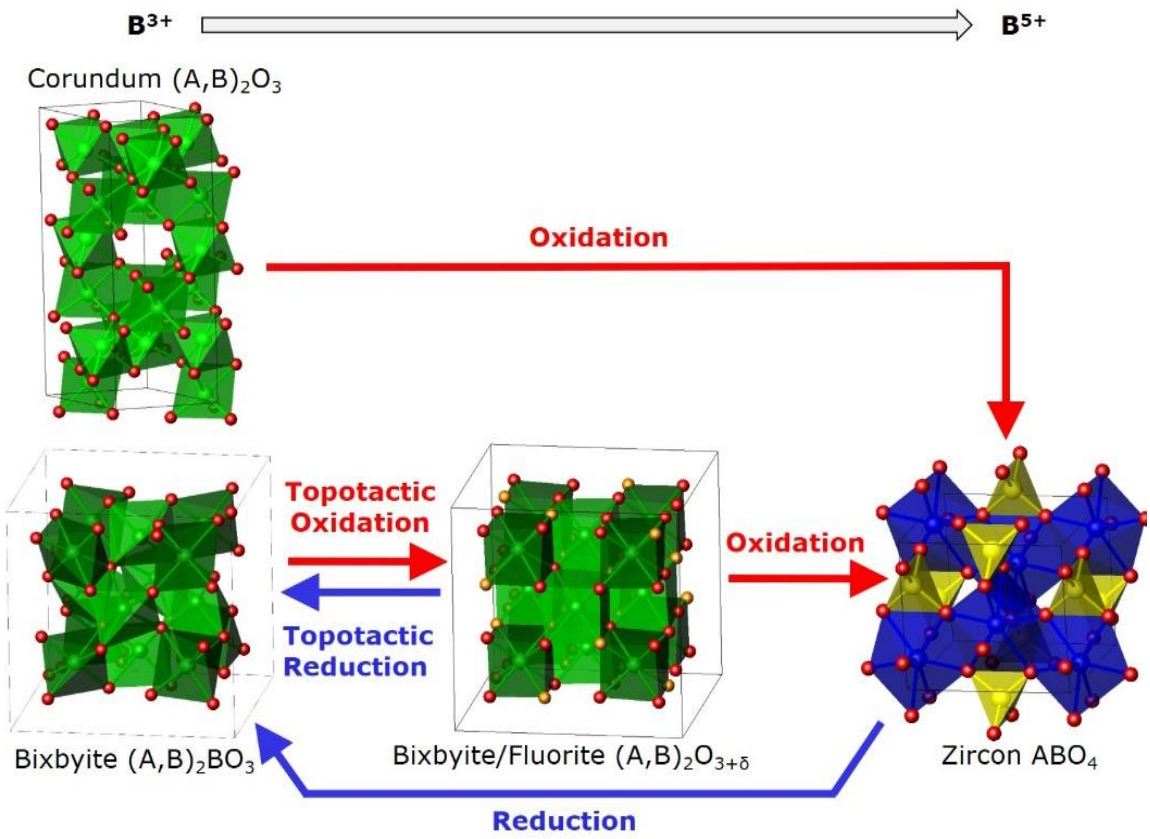

Figure 4.1: Illustration of the structures encountered in the $Sc_{2-x}V_xO_{3+\delta}$ system. (Note the reaction byproducts Sc_2O_3 and V_nO_m are not shown.). The corundum structures (top) $Sc_{2-x}V_xO_3$ ($x \geq 1.68$) crystallizes in space group R-3c and undergoes direct oxidation to the zircon structure (space group $I4_1/amd$). The cubic bixbyite structures $Sc_{2-x}V_xO_3$ ($x \leq 1.08$) (space group: Ia-3) oxidize topotactically to form either oxidized bixbyites ($x < 0.50$) or defect fluorite structures (space group: Fm-3m) $Sc_{2-x}V_xO_{3+\delta}$ ($x \leq 1.08$) (bottom, centre). Green = Sc^{3+}/V^{n+} sites, blue = Sc^{3+} sites, yellow = V^{n+} site, red = O^{2-} sites, orange = vacancy/ O^{2-} sites.

The scandium – vanadium – oxygen phase diagram shows a variety of structure types and oxygen compositions including bixbyites, fluorites, pyrochlores, and an Sc_2VO_5 phase [18–23]. The work reported in this article is a comprehensive study of the structural evolution and reactivity of the full $Sc_{2-x}V_xO_3$ series, covering the entire Sc:V compositional range.

4.3. Experimental

4.3.1. Synthesis

Bulk powder samples of $ScVO_3$ were prepared using a modified two-step synthesis developed by Shafi et al.[24,25] First, $ScVO_4$ was synthesized using stoichiometric amounts of Sc_2O_3 (Alfa Aesar: 99.99% or Synquest Laboratories 99.95%) and NH_4VO_3 (Cerac: 99.9%) which were ground in an acetone slurry using an agate mortar and pestle. Starting materials were then heated in air at 1000°C for 12 hours in an alumina crucible in order for following reaction to occur:

$$Sc_2O_3 + 2NH_4VO_3 \rightarrow 2ScVO_4 + 2NH_3 + H_2O \qquad \text{(eq. 4.1)}$$

Powder X-ray diffraction data identified the beige polycrystalline product as phase pure $ScVO_4$ before proceeding to the next step. The $ScVO_4$ phase was reduced to single phase dark brown $ScVO_3$ in flowing H_2 gas at 1100°C for 18 hours (eq. 4.2):

$$ScVO_4 + H_2 \rightarrow ScVO_3 + H_2O \qquad \text{(eq. 4.2)}$$

Phase pure V_2O_3 was obtained via reduction of V_2O_5 (Alfa Aesar, 99.9%) at 1100°C in H_2-flow for 18 hours. $Sc_{2-x}V_xO_3$ samples were prepared using stoichiometric amounts of Sc_2O_3 (Alfa Aesar, 99.9%) and V_2O_3 according to eq. 4.3, where x was varied in 0.25 increments between 0 and 1.50 and in 0.05 increments from 1.70 to 2.00. All samples were ground using an agate mortar and pestle, pelletized, and heated at 1500°C in dilute hydrogen (3-5% H_2, balance Ar) for multiple

heatings of 12-48 hours with intermediate grindings until phase pure samples were obtained (table 4.1 shows the heating times required).

$$(1- ½ x)\ Sc_2O_3 + ½ x\ V_2O_3 \rightarrow Sc_{2-x}V_xO_3 \qquad \text{(eq. 4.3)}$$

Table 4.1: List of heating times required in order to synthesize phase-pure samples of $Sc_{2-x}V_xO_3$.

x	Time Required
0.25	12-24 hrs
0.50	24-64 hrs
0.75	64 hrs
1.00	164 hrs
1.25	N/A
1.50	N/A
1.75	24-64 hours
1.90	< 12 hrs

4.3.2. Characterization

4.3.2.1 Powder X-ray Diffraction at Room Temperature

Room temperature powder X-ray diffraction data were collected using Cu Kα radiation (λ ($K\alpha_1$) = 1.540598 Å, and λ ($K\alpha_2$) = 1.544426 Å) on a PANalytical X'Pert Pro diffractometer in Bragg-Brentano geometry (PANalytical B.V., Almelo, the Netherlands). All measurements were carried out using a 1° divergence slit, 10 mm mask, and 0.04 rad soller slits for the primary beam and an antiscatter slit, a Ni filter, 0.04 rad soller slits and an X'Celerator detector (128 microstrip detector) for the diffracted beam. Samples were mounted as thin layers on a zero background sample holder (Si (510)) using acetone slurries. Measurements were conducted on a spinning sample stage at 1 Hz and data were collected with 0.0167° steps covering a 2θ range from 10° to 120° at 50 s/step counting time for Rietveld refinements. The diffractometer line profiles were

confirmed with NIST standard LaB_6 SRM 660a, and peak positions were confirmed with NIST standard Si SRM 640b.

4.3.2.2 Room Temperature Neutron Powder Diffraction

Neutron powder diffraction data were collected at room temperature using the POWGEN diffractometer, at the Spallation Neutron Source (SNS) at Oak Ridge National Laboratory in Oak Ridge, Tennessee. Approximately 2 grams of sample were loaded into an 8 mm diameter cylindrical vanadium sample can. Using frames with 1.066 Å and 2.665 Å center wavelengths, the d-spacing range from 0.276 Å to 10.5 Å were collected using a slit width of 20 mm and a slit height of 35 mm. Data were collected for approximately one hour per frame.

4.3.2.3 High-Temperature in-situ Powder X-ray Diffraction

High temperature *in-situ* powder X-ray diffraction experiments were carried out using the same diffractometer described in section 3.2.1, where samples were mounted as an acetone slurry directly on a 10 mm platinum resistive strip heater within a self-masking Anton Paar HTK2000 furnace (Anton Paar GmbH). Between room temperature and 1200°C the furnace is reliable within ±5°C. X-ray diffractograms were collected in increments of 25°C from 25°C to 1000°C and during cooling in 25°C decrements to room temperature. Data were collected in 0.0167° steps covering $20° \leq 2\theta \leq 70°$ with 100 s/step counting time over all 128 detector microstrips for a total of 45 minutes at each temperature.

4.3.2.4 Rietveld Refinements

All Rietveld refinements were carried out using the *Topas (version 5)* software. The crystallographic structures were refined simultaneously against powder X-ray and time-of-flight neutron diffraction data as described in sections 4.3.2.1 and 4.3.2.2, respectively. 62 parameters were refined including background coefficients, peak shapes and asymmetries, unit cell parameters, atomic positions, and isotropic temperature factors. Despite the lack of X-ray scattering contrast between scandium and vanadium, and the near zero neutron scattering length of vanadium, simultaneous X-ray and neutron refinements allow for the determination of scandium to vanadium ratios. This ratio was refined allowing the cations to freely distribute over all cation positions. Oxygen occupancies were fixed to be fully occupied. For all refinements based on laboratory powder X-ray diffraction data only, oxygen positions, and scandium/vanadium ratios and distributions were not refined. Samples with a small impurity of $Sc_2Si_2O_7$ (see section 4.2) were refined with this additional phase in order to characterize weight percentages. The parameters refined for this phase were limited to unit cell lengths and angles, and scale factors, all other parameters were set based on the work reported by Foord *et al.*[27]

4.4. Results and Discussion

4.4.1. Synthesis of $Sc_{2-x}V_xO_3$ ($0 \leq x \leq 2.00$)

The compositional series $Sc_{2-x}V_xO_3$ ($0 \leq x \leq 2.00$) was prepared according to equation 3 by direct solid-state reaction of Sc_2O_3 and V_2O_3 at 1500°C in 3% H_2 until no further reaction was observed.[15] Figure 2 compares the powder X-ray diffractograms of the final products, indicating

the formation of bixbyite phases for the Sc-rich compositions and corundum phases for the V-rich samples. Notably both reported phases are cation disordered structures, the cubic bixbyite structure shows a small site preference for the two different cations sites (*8b* and *24d*) whereas the corundum structure is fully disordered because only one cation site is accessible. The powder X-ray diffractograms in Figure 4.2b follow multiple heating steps at 1500°C for the nominal composition $ScVO_3$. During the initial stage of the reaction vanadium-doped Sc_2O_3 bixbyite and scandium-doped V_2O_3 corundum phases are formed. Additional heating cycles cause the bixbyite phase to slowly increase its vanadium content, whereas the scandium concentration remains constant in the corundum structure, while the phase fraction of the corundum phase decreased. This clearly shows that the corundum phase reaches scandium saturation within 12 hours and that this phase reacts further with the bixbyite phase. In particular, after 12, 24 and 64 hours the broad and distorted bixbyite peaks indicate multiple bixbyite phases with varying vanadium content to be present.

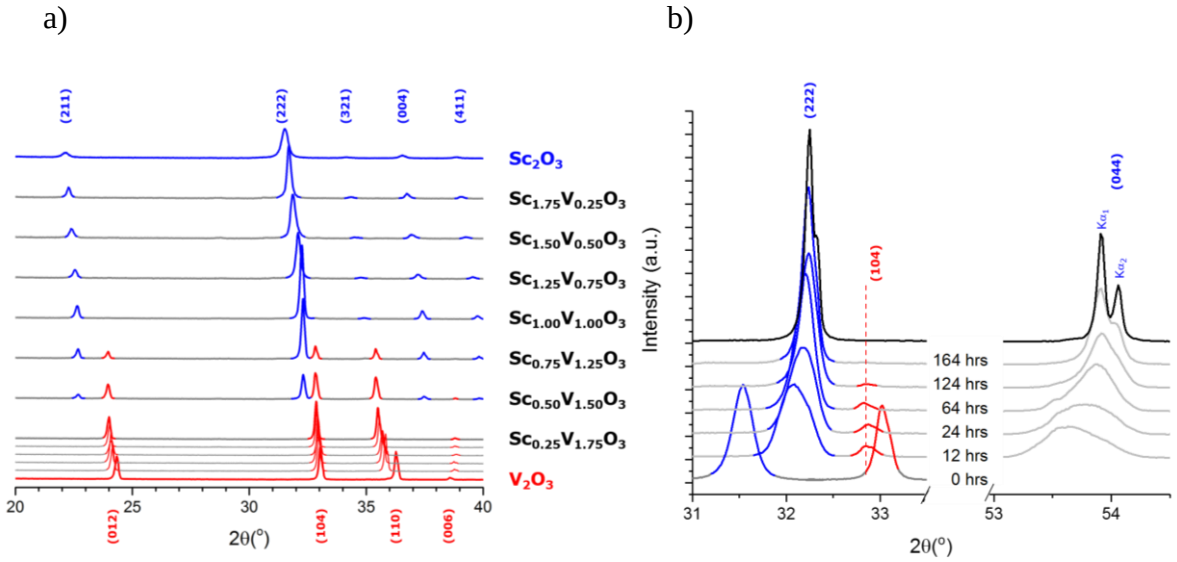

Figure 4.2a: Room temperature powder X-ray diffractograms (Cu $K\alpha_{1,2}$) for the compositional series $Sc_{(2-x)}V_xO_3$. Blue peaks belong to the cubic bixbyite phase (space group: Ia-3) and red peaks belong to the trigonal corundum phase (space group: R-3c). Note: Corundum peaks are indexed with respect to the trigonal cell. The diffraction patterns for the pure corundum phases (bottom) use an increment of x = 0.05. Sc_2O_3 and V_2O_3 patterns are provided for a comparison. Note that only the nominal compositions $Sc_{0.75}V_{1.25}O_{3.00}$ and $Sc_{0.50}V_{1.50}O_{3.00}$ show the presence of both phases.

Figure 4.2b: Room temperature powder X-ray diffractograms for the solid-state formation of $ScVO_{3.00}$ from Sc_2O_3 and V_2O_3 as a function of reaction time at 1500°C (in 3% H_2) show the compositional change of the bixbyite phase as indicated by the shift of the (222) bixbyite peak position. In contrast the (104) corundum peak position only shows an appreciable change during the first 12 hours, after that the intensity of the peak decreases until only the $ScVO_{3.00}$ bixbyite phase is present. The (044) bixbyite peak on the right emphasizes the peak shift and increasing crystallinity of the product phase with prolonged heating. The most upper data set (black trace) refers to $ScVO_{3.00}$ synthesized via $ScVO_4$ reduction and indicates the high degree of crystallinity of that phase using the indirect synthesis route.

Notably, the synthesis of phase pure $ScVO_3$ bulk required 164 hours for the direct synthesis at 1500°C according to equation 4.3, whereas the alternative preparation via reduction of the $ScVO_4$ zircon phase[24,25] in H_2 gas (equation 4.2) required less than 18 hours at temperatures as low as 1100°C. Figure 4.2b compares the powder diffraction peak widths for multiple heatings for the direct synthesis and the reductive route. After 164 hours at 1500°C, the crystalline domain size (estimated with the Scherrer equation) approaches 1200 Å, whereas the reductive route yielded domain sizes > 9000 Å after only 18 hours at 1100°C. We propose that the rate limiting step for

the direct reaction between Sc_2O_3 and V_2O_3 is due to grain boundary effects and the relatively large diffusion distances during the inter-particle reaction results in small crystalline domain sizes. In contrast, large crystalline domain sizes are found when no grain boundaries are involved during the intraparticle reduction of $ScVO_4$ to $ScVO_3$ in hydrogen. Figure 4.3 shows the volume per formula unit evolution, obtained from Rietveld refinements, for the bixbyite structure (Sc-rich compositions) and the corundum structure (V-rich compositions). The bixbyite and corundum phases are separated by a miscibility gap defined by the $Sc_{0.92}V_{1.08}O_3$ bixbyite and the $Sc_{0.32}V_{1.68}O_3$ corundum phases.

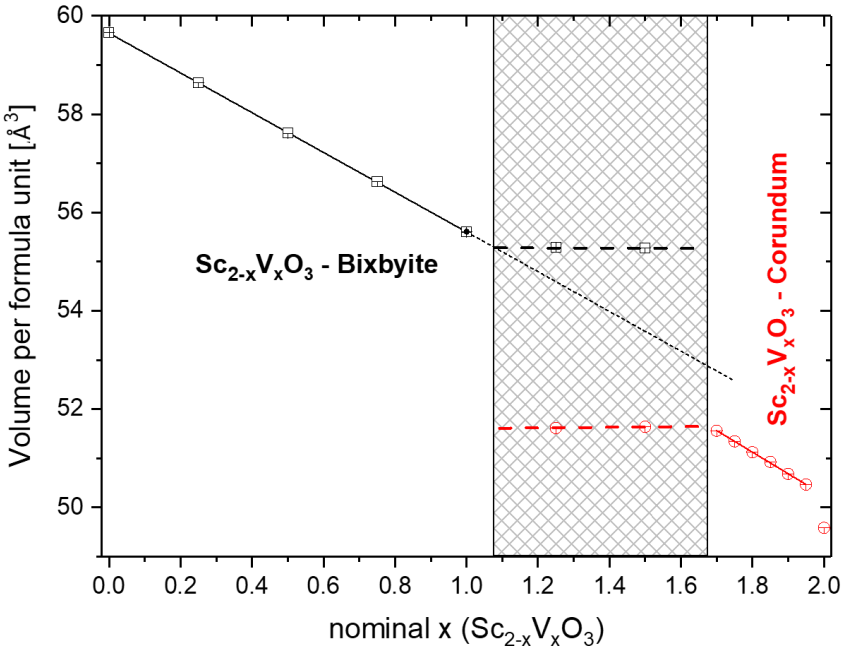

Figure 4.3: Evolution of the bixbyite and corundum phases $Sc_{(2-x)}V_xO_3$ as a function of x. The volumes per formula unit were obtained from Rietveld refinements. The miscibility gap spans from x = 1.08 to 1.68. The dashed lines serve as a guide to the eye. The V/Z value for the $ScVO_3$ phase obtained via reduction of $ScVO_4$ is shown as a solid black circle.

The phases close to the end members form readily within 12 to 24 hours at 1500°C, whereas samples closer to the miscibility gap require multiple regrinding and heating with total annealing times exceeding 5 days. The extended heating periods at 1500°C caused the formation of small amounts of $Sc_2Si_2O_7$ impurity phases due to the reaction with silicates in the ceramic boats (up to 0.2% SiO_2 in alumina).

Figure 4.3 shows a linear volume decrease for the bixbyite phases $Sc_{2-x}V_xO_3$ ($0 \leq x \leq 1.0$) as a function of vanadium concentration. The corundum phases $Sc_{2-x}V_xO_3$ ($1.70 \geq x \geq 2.00$) show a linear increase of the unit cell volume upon scandium uptake. Only V_2O_3 does not follow the otherwise linear trend. The miscibility gap limits of $1.08 \leq x \leq 1.68$ have been extrapolated from the bixbyite and corundum phases. The corundum phase is clearly the denser phase and might be

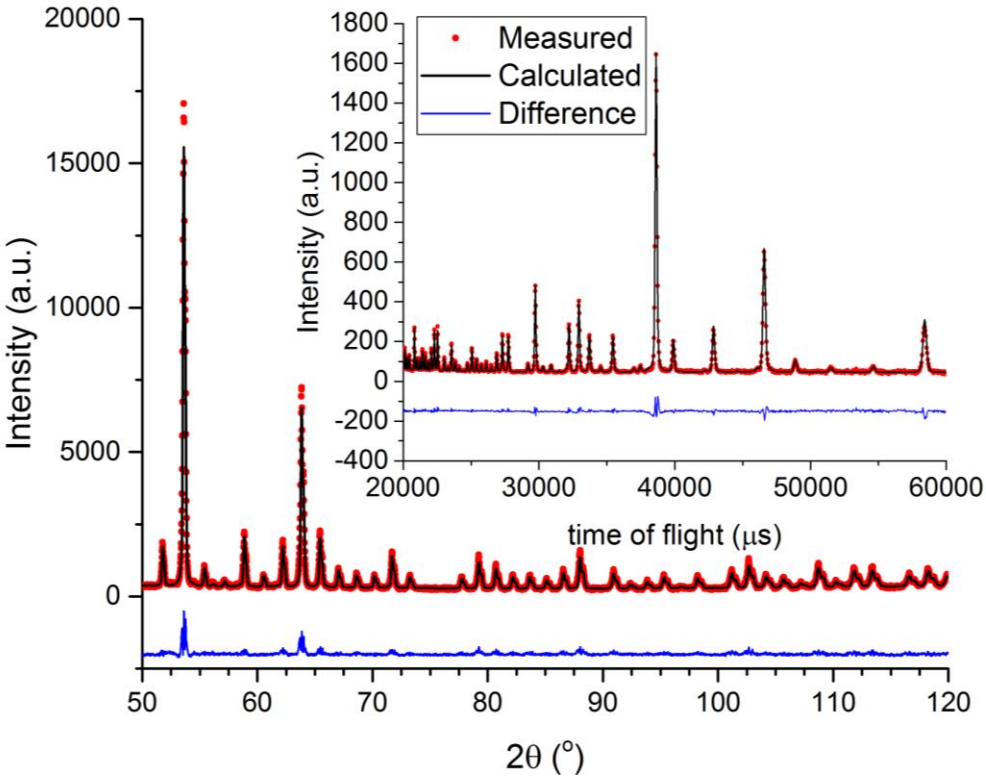

Figure 4.4: Rietveld plot of the powder X-ray diffraction data for the refinement of the cubic bixbyite phase $Sc_{1.25}V_{0.75}O_{3.00}$. The insert shows the time-of-flight powder neutron diffraction Rietveld plot. Red symbols = observed data, black line = fit, blue line = difference. All crystallographic information is provided in table 1.

obtainable for smaller vanadium concentrations using high pressure synthesis. Notably the high pressure structure of $ScVO_3$ has been reported as an orthorhombic perovskite phase [28], suggesting a potentially rich phase diagram for high pressure phases across the $Sc_{2-x}V_xO_3$ system.

4.4.2. Structural Information of the $Sc_{2-x}V_xO_3$ Solid Solution

For all samples where x < 1.0, simultaneous multiple-histogram Rietveld refinements were performed using time-of-flight neutron diffraction (POWGEN) and powder X-ray diffraction data. A total of 62 parameters were refined for each composition. Figure 4.4 shows the Rietveld plots for $Sc_{1.25}V_{0.75}O_{3.00}$. Additional Rietveld plots for $Sc_{1.50}V_{0.50}O_{3.00}$ and $Sc_{1.75}V_{0.25}O_{3.00}$ are provided in figure 4.5. Table 4.2 reports the structural details extracted from all refinements. V^{3+} has a slight preference towards the *8b* site in all three cubic bixbyite phases, this is in agreement with the previous report of $ScVO_3$ by Alonso et al.[16] The authors proposed that the V^{3+} preference on the *8b* site was due to a scandium deficiency. No explanation as to the preference of vanadium on the *8b* versus the *24d* site was discussed. The refined Sc:V ratio, as reported in table 1, for all three compounds (x = 0.25, 0.50, 0.75) showed a 5.5% variance, where more V was found than expected. This can be rationalized by the small impurity of $Sc_2Si_2O_7$ which can be found for most samples. Rietveld refinements suggest that this impurity phase is present typically at 2-3 wt.%. We are confident that this small impurity does not affect the current results and note that the impurity was formed as a reaction of Sc_2O_3 with silicates in the ceramic boats used during synthesis.

Table 4.2: Structural parameters for the cubic bixbyite phases (space group: $Ia\bar{3}$ (#206)) of $Sc_{2-x}V_xO_{3.00}$. Values were obtained from simultaneous Rietveld Refinement against powder X-ray diffraction data and time-of-flight powder neutron data measured at room temperature.

Target Composition		$Sc_{1.25}V_{0.75}O_{3.00}$	$Sc_{1.50}V_{0.50}O_{3.00}$	$Sc_{1.75}V_{0.25}O_{3.00}$
Refined Composition		$Sc_{1.14}V_{0.86}O_{3.00}$	$Sc_{1.39}V_{061}O_{3.00}$	$Sc_{1.64}V_{0.36}O_{3.00}$
space group		$Ia\bar{3}$ (206)	$Ia\bar{3}$ (206)	$Ia\bar{3}$ (206)
unit cell	a (Å) V (Å^3)	9.669400(80) 904.063(23)	9.726734(60) 920.240(17)	9.78607(6) 937.18(2)
Sc/V(*8b*) (¼, ¼, ¼)	Occupancy (%): Sc V B_{iso}	 43.7 (3) 56.3 (3) 0.144 (25)	 58.5 (3) 41.5 (3) 0.215 (18)	 75.3 (3) 24.7 (3) 0.22 (1)
Sc/V (*24d*) (x, 0, ¼)	x/a Occupancy (%): Sc V B_{iso}	-0.03540 (6) 61.2 (2) 38.8 (2) 0.201 (13)	-0.03555 (6) 73.0 (2) 27.0 (2) 0.235 (10)	-0.03565 (4) 84.5 (2) 15.5 (2) 0.224 (9)
O (*48e*) (x, y, z)	x/a y/b z/c Occupancy (%) B_{iso}	0.39143 (7) 0.15559 (7) 0.38053 (7) 100 0.342 (13)	0.39154 (6) 0.15547 (7) 0.38076 (6) 100 0.341 (12)	0.39153 (6) 0.15535 (6) 0.38085 (6) 100 0.30 (1)
χ^2/R_{wp}:	Neutron (T.O.F.)[a] Neutron (T.O.F.)[b] X-ray (Cu-k_α)[c] Overall	2.27/3.51 5.82/6.22 2.16/8.27 3.01/5.53	2.35/3.09 6.29/7.51 1.97/7.43 3.10/5.45	2.21/2.84 6.47/6.42 2.16/8.22 3.18/5.18

[a]Neutron T.O.F range: 6778 – 118037 μs, 3574 data points
[b]Neutron T.O.F range: 26213 – 97998 μs, 1650 data points
[c]X-ray Cu-K_α, $20° \leq 2\theta \leq 120°$, $\Delta 2\theta = 0.0167°$, 5984 data points

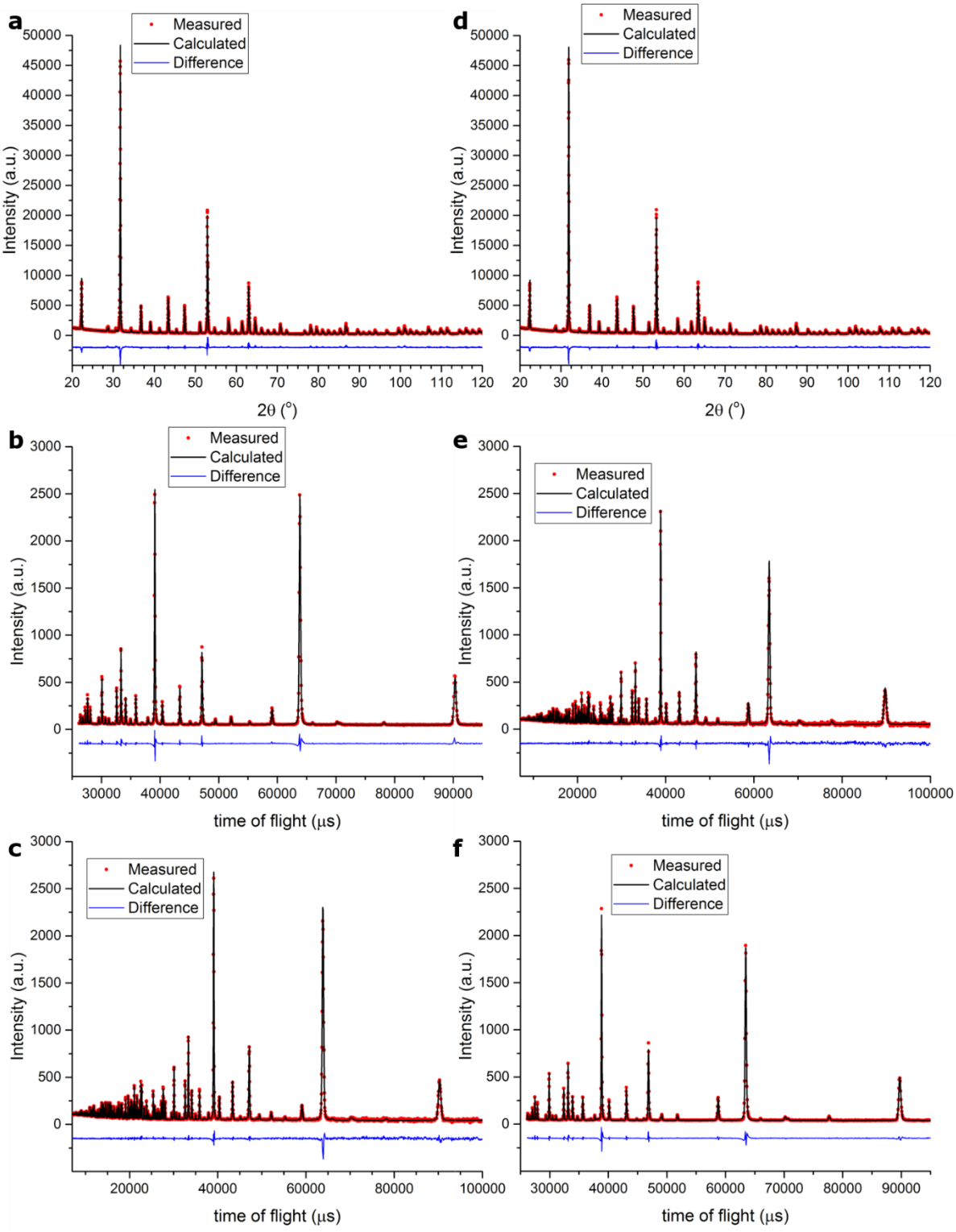

Figure 4.5: Rietveld plots of the powder diffraction data for the refinements of the cubic bixbyite phases: a-c) $Sc_{1.75}V_{0.25}O_3$; d-f) $Sc_{1.50}V_{0.50}O_3$. Refinements are based on a,d) X-ray diffraction data; b,e) time-of-flight neutron powder diffraction data (centre wavelength = 2.665 Å); c,f) time-of-flight neutron powder diffraction data (centre wavelength = 1.066 Å). Red symbols = observed data, black line = fit, blue line = difference. All crystallographic information can be found in table 1.

4.4.3. Stability Range of the $Sc_{2-x}V_xO_3$ System

In an effort to understand the oxidation pathway of the bixbyite starting materials, high temperature *in-situ* powder X-ray diffraction experiments were carried out in flowing O_2. These experiments allow for the investigation of the various oxidative pathways during the oxidation of $Sc_{2-x}V_xO_{3.00}$, which include various topotactic and reconstructive reactions.

Figure 4.6 shows contour plots of the oxidation of the $Sc_{2-x}V_xO_{3.00}$ series. Rietveld refinements were conducted at each heating step in order to create figure 4.7, which illustrates the formation of competing oxidative products during heating of the $Sc_{2-x}V_xO_{3.00}$ samples in O_2 using *in-situ* powder X-ray diffraction.

The Sc-rich compositions spanning $0 \leq x \leq 1.08$ form bixbyite structures for the V^{3+} containing phases. Upon oxidation the formation of $Sc_{1.75}V_{0.25}O_{3.25}$ bixbyite phase is observed. The original $Sc_{1.75}V_{0.25}O_{3.00}$ and fully oxidized variant $Sc_{1.75}V_{0.25}O_{3.25}$ seem to coexist between 300°C and 375°C. Only at 800°C is the phase separation into $ScVO_4$ and residual Sc_2O_3 observed. $Sc_{1.50}V_{0.50}O_{3.00}$ oxidizes at 300°C to the defect fluorite structure $Sc_{1.50}V_{0.50}O_{3.50}$ and at 375°C the entire sample has been converted to the fully oxidized product. This can be seen in the contour plot by the disappearance of the bixbyite superstructure (321), (411), and (332) peaks; which is accompanied by a shift of the main peaks to larger d-spacings due to oxygen uptake. The phase separation into $ScVO_4$ and excess Sc_2O_3 is observed at 650°C. The $Sc_{1.25}V_{0.75}O_{3.00}$ phase oxidizes at 300°C to the defect fluorite structure $Sc_{1.25}V_{0.75}O_{3.50}$ and complete conversion is observed at 400°C. Between 400°C and 625°C further oxidation of the defect fluorite phase is observed and at 700°C the defect fluorite phase decomposes into $ScVO_4$ and additional Sc_2O_3. The *in-situ*

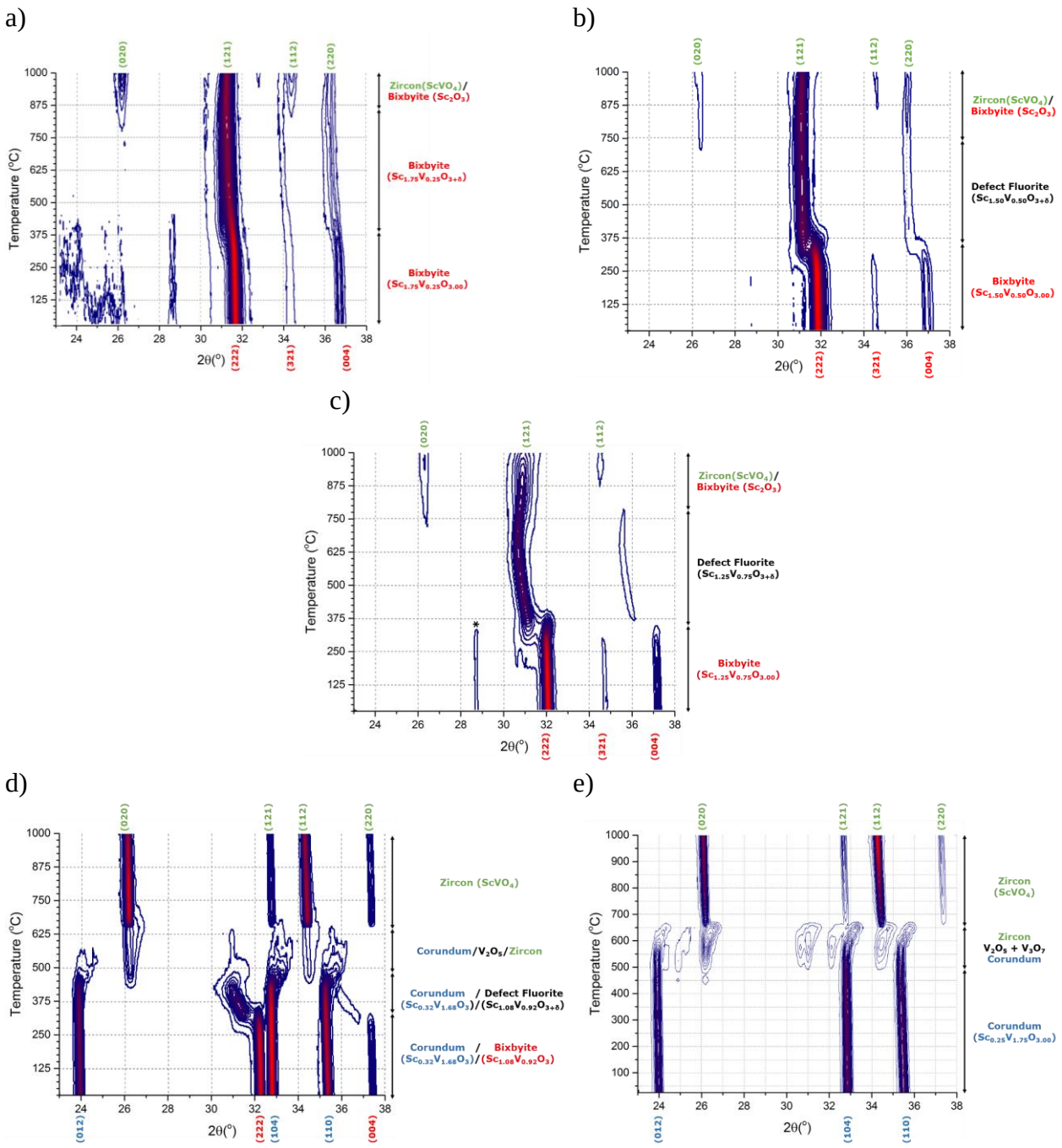

Figure 4.6: Contour plots of high temperature powder X-ray in-situ diffraction data showing the oxidation pathway of a) the bixbyite $Sc_{1.75}V_{0.25}O_{3.00}$, b) the bixbyite $Sc_{1.50}V_{0.50}O_{3.00}$, c) the bixbyite $Sc_{1.25}V_{0.75}O_{3.00}$ d) the biphasic bixbyite $Sc_{1.08}V_{0.92}O_{3.00}$ plus corundum $Sc_{0.32}V_{1.68}O_{3.00}$, and e) the corundum $Sc_{0.25}V_{1.75}O_{3.00}$ phases. The intermediate and final product phases are indicated with the respective temperature ranges on the right. Miller indices for the diffraction peaks are indicated at the bottom and top of the figures. Intensities are shown as constant increments from blue to red.

oxidation of $ScVO_{3.00}$ has been reported in the literature[16,24] and showed the formation of the defect fluorite structure $ScVO_{3.50}$ at 300°C which oxidizes further to $ScVO_{3.72}$ (defect fluorite) and finally undergoes a reconstructive oxidation to $ScVO_4$. The nominal composition $Sc_{0.50}V_{1.50}O_{3.00}$ contains a bixbyite phase of composition $Sc_{0.92}V_{1.08}O_{3.00}$ and a corundum phase with composition $Sc_{0.32}V_{1.68}O_{3.00}$. The bixbyite phase oxidizes at 300°C to the defect fluorite phase $Sc_{0.92}V_{1.08}O_{3.50}$ and after the entire bixbyite fraction oxidized to $Sc_{0.92}V_{1.08}O_{3.50}$, further topotactic oxidation to $Sc_{0.92}V_{1.08}O_{3.75}$ is observed. Notably the corundum phase $Sc_{0.32}V_{1.68}O_{3.00}$ remains stable up to 500°C before releasing vanadium oxide while converting together with the defect fluorite structure to the zircon phase $ScVO_4$. At 670°C vanadium oxide is fully oxidized to V_2O_5 and melts, this increases the diffraction pattern background and a rapid formation of $ScVO_4$ is observed at that temperature. It is proposed

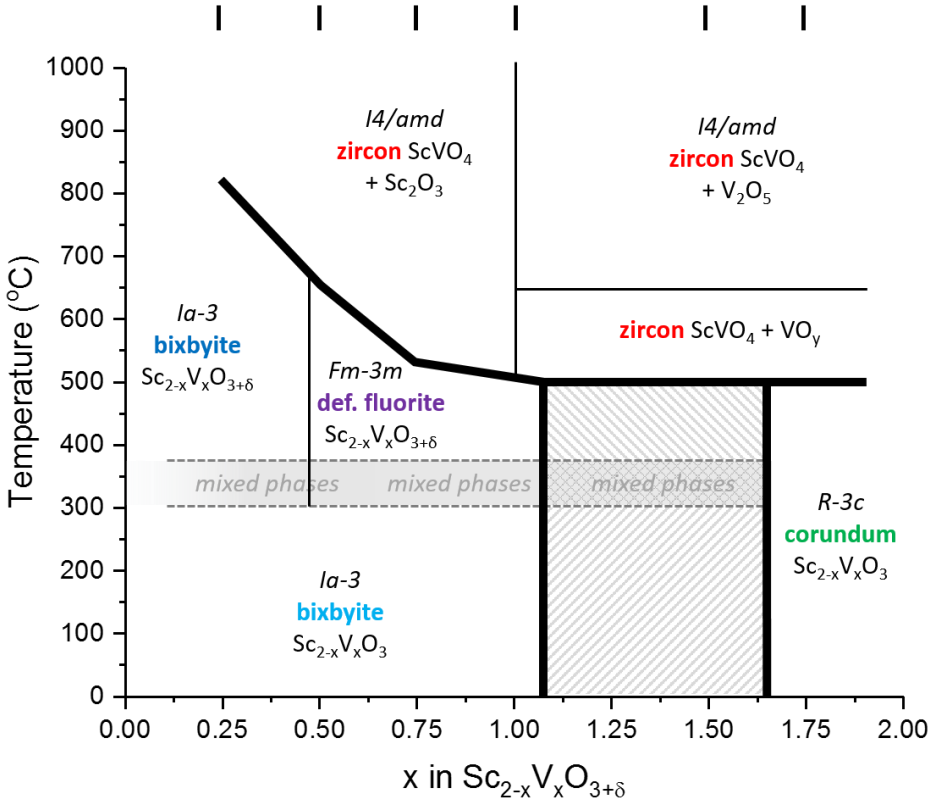

Figure 4.7: Summarizing diagram of oxidation reactions of the $Sc_{(2-x)}V_xO_{3.00}$ phases as determined by in-situ powder X-ray diffraction experiments. The scandium rich phases form cubic bixbyite and cubic defect fluorite structures before fully oxidizing to zircon phases. Notably between 300°C and 375°C the reduced and partially oxidized phases coexist. The reduced vanadium rich members (x > 1.68) oxidize directly to zircon and partially oxidized vanadium oxides at 500°C. At 650°C oxidation to V_2O_5 is observed and when reaching the melting point of V_2O_5 (670°C) the zircon phase increases crystallinity.

that the liquid V_2O_5 phase increases the reactivity and initiates the formation of a highly crystalline $ScVO_4$ phase. The composition $Sc_{0.25}V_{1.75}O_{3.00}$ is a pure corundum phase which undergoes oxidative decomposition at 500°C with the formation of V_3O_7 and V_2O_5. V_3O_7 oxidizes to V_2O_5 and consecutively melts at 670°C which initiates the rapid formation of highly crystalline $ScVO_4$.

It can be concluded that the topotactic oxidation occurs at the same temperature for all $Sc_{2-x}V_xO_{3.00}$ bixbyite materials; however, a minimum amount of x = 0.50 V for the solid solution is required in order to permit the formation of the disordered defect fluorite structure upon oxidation. The initial oxidation (if a sufficient quantity of vanadium is present) results in a $Sc_{2-x}V_xO_{3.50}$ defect fluorite structure. Further topotactic oxidation is observed until either only V^{5+} is present or until the oxygen stoichiometry has reached 3.75. Further heating and oxidation (if a sufficient quantity of vanadium is present) results in the formation of the $ScVO_4$ zircon phase and residual Sc_2O_3 for $x < 1.00$. For $x > 1.00$ vanadium oxides are the observed by-products. Notably, the corundum structure is inherently oxidatively stable; it does not permit a low energy topotactic oxidation pathway which is consistent with the fact that no topotactic oxidation products are known for the corundum structure.

The formation temperature of $ScVO_4$ increases as the vanadium concentration decreases in the fluorite phase. The decomposition from the defect fluorite to the zircon structure is believed to be due to the large size difference of the cations as vanadium is oxidized ((Sc^{3+}(r(VI) = 0.745Å), V^{3+}(r(VI) = 0.64Å) , V^{4+}(r(VI) = 0.58Å) , V^{5+}(r(VI) = 0.54Å)).[29] These size differences cause the cations to undergo ordering with the small V^{5+} forming isolated VO_4^{3-} tetrahedra. The increased stability of the scandium rich defect fluorite phases found here is due to the smaller amount of vanadium in the disordered cation lattice. Consequently, the smaller V^{5+} cations are found less often in the lattice, having less of an impact on the overall structure and reducing the need to order.

The increase in stability of the defect fluorite as the amount of vanadium in the system is decreased is favourable for use as solid-state oxide ion conductors due to the extended working temperature regime. Because these devices typically run at high temperatures (e.g. intermediate and high temperature SOFCs operate between 500 °C and 1000 °C), extending the stability field of the materials working temperatures is important. However, in order to understand the potential applications for these materials the effect of the change in Sc:V ratio on electrical conductivity must be investigated.

4.5. Conclusions

The $Sc_{2-x}V_xO_{3+\delta}$ ($0 \leq x \leq 2.00$ and $0 \leq \delta \leq 1$) series was explored using powder X-ray and neutron diffraction experiments. We have illustrated that a phase pure bixbyite solid solution exists between x = 0.00 and 1.08; and between x = 1.68 and 2.00 phase pure corundum structures are found. Between x = 1.08 and 1.68 there is a miscibility gap where a mixture of the bixbyite $Sc_{0.92}V_{1.08}O_{3.0}$ and the corundum $Sc_{0.32}V_{1.68}O_{3.0}$ is present with corresponding phase fractions based on the nominal composition. It has been shown that the corundum phase reaches scandium saturation quickly, reacting with the bixbyite more slowly until phase pure samples result. A comparison of reaction strategies for the synthesis of $ScVO_{3.0}$ indicate that the rate limiting step for the direct reaction between Sc_2O_3 and V_2O_3 is due to the large diffusion distances and grain boundary effects. Structural parameters are reported for the bixbyite solid solution, and a slight vanadium preference towards the *8b* site for all materials is found throughout the series. In-situ X-ray oxidation studies reveal the oxidative pathway of the series, and a multitude of oxidative transitions throughout the series are reported. All oxidation pathways end with $ScVO_4$ as a final product and are accompanied by Sc_2O_3 when $x < 1.0$ and V_2O_5 when $x > 1.0$.

4.6. Acknowledgements

M.B. acknowledges the support from NSERC, CFI and MIF. J.A.L. is thankful for financial support from the University of Manitoba and the NSERC Postgraduate Scholarship-Doctoral program. V.T. would like to thank NSERC for support. A portion of this research at ORNL's Spallation Neutron Source was sponsored by the Scientific User Facilities Division, Office of Basic Energy Sciences, U.S. Department of Energy. The Authors would like to thank Melanie Kirkham and Ashfia Huq for data collection and technical help with POWGEN data.

References

(1) Miyasaka, S.; Okimoto, Y.; Iwama, M.; Tokura, Y. Spin-Orbital Phase Diagram of Perovskite-Type RVO_3 (R=rare-Earth Ion or Y). *Phys. Rev. B: Condens. Matter Mater. Phys.* **2003**, *68* (10), 100406.

(2) Johnson, R. D.; Tang, C. C.; Evans, I. R.; Bland, S. R.; Free, D. G.; Beale, T. A. W.; Hatton, P. D.; Bouchenoire, L.; Prabhakaran, D.; Boothroyd, A. T. X-Ray Diffraction Study of the Temperature-Induced Structural Phase Transitions in $SmVO_3$. *Phys. Rev. B: Condens. Matter Mater. Phys.* **2012**, *85* (22), 224102.

(3) Dorogova, M.; Navrotsky, A.; Boatner, L. A. Enthalpies of Formation of Rare Earth Orthovanadates, $REVO_4$. *J. Solid State Chem.* **2007**, *180* (3), 847–851.

(4) Mahlik, S.; Amer, M.; Boutinaud, P. Energy Level Structure of Bi^{3+} in Zircon and Scheelite Polymorphs of YVO_4. *J. Phys. Chem. C* **2016**, *120* (15), 8261–8265.

(5) Ren, Y.; Palstra, T. T. M.; Khomskii, D. I.; Pellegrin, E.; Nugroho, A. A.; Menovsky, A. A.; Sawatzky, G. A. Temperature-Induced Magnetization Reversal in a YVO_3 Single Crystal. *Nature* **1998**, *396* (6710), 441–444.

(6) Mizokawa, T.; Khomskii, D. I.; Sawatzky, G. A. Interplay between Orbital Ordering and Lattice Distortions in $LaMnO_3$, YVO_3, and $YTiO_3$. *Phys. Rev. B: Condens. Matter Mater. Phys.* **1999**, *60* (10), 5.

(7) Nguyen, H. C.; Goodenough, J. B. Magnetic Studies of Some Orthovanadates. *Phys. Rev. B: Condens. Matter Mater. Phys.* **1995**, *52* (1), 324–334.

(8) Sarkar, T.; Ivanov, S. A.; Bazuev, G. V.; Nordblad, P.; Mathieu, R. Thermal Evolution of the Spin Ordering at the Concomitant Spin-Orbital Rearrangement Temperature in RVO_3

(R=Lu, Yb and Tm). *J. Magn. Magn. Mater.* **2016**, *409*, 87–91.

(9) Yan, J. Q.; Zhou, J. S.; Goodenough, J. B. Opposing Spin-Canting Mechanism in Single-Crystal $LuVO_3$ and YVO_3. *Phys. Rev. B: Condens. Matter Mater. Phys.* **2005**, *72* (9), 94412.

(10) Zhang, Q.; Singh, K.; Simon, C.; Tung, L. D.; Balakrishnan, G.; Hardy, V. Impact of the Various Spin- and Orbital-Ordering Processes on the Multiferroic Properties of Orthovanadate $DyVO_3$. *Phys. Rev. B: Condens. Matter Mater. Phys.* **2014**, *90* (2), 24418.

(11) Muñoz, A.; Alonso, J.; Casáis, M.; Martínez-Lope, M.; Martínez, J.; Fernández-Díaz, M. Crystallographic and Magnetic Transitions in $CeVO_3$: A Neutron Diffraction Study. *Phys. Rev. B: Condens. Matter Mater. Phys.* **2003**, *68* (14), 144429.

(12) Goodenough, J. B. Ceramic Technology: Oxide-Ion Conductors by Design. *Nature* **2000**, *404* (6780), 821–823.

(13) Tang, S.; Huang, M.; Wang, J.; Yu, F.; Shang, G.; Wu, J. Hydrothermal Synthesis and Luminescence Properties of $GdVO_4$: Ln^{3+} (Ln = Eu, Sm, Dy) Phosphors. *J. Alloys Compd.* **2012**, *513*, 474–480.

(14) Oshikiri, M.; Ye, J.; Boero, M. Inhomogeneous RVO_4 Photocatalyst Systems (R = Y, Ce, Pr, Nd, Sm, Eu, Gd, Tb, Dy, Ho, Er, Tm, Yb, Lu). *J. Phys. Chem. C* **2014**, *118* (16), 8331–8341.

(15) Reid, A. F.; Sienko, M. J. Scandium Titanite and Scandium Vanadite. *Inorg. Chem.* **1967**, *6* (3), 521–524.

(16) Alonso, J. A.; Casais, M. T.; Martinez-Lope, M. J. Preparation and Topotactical Oxidation of $ScVO_3$ with Bixbyte Structure: A Low-Temperature Route to Stabilize the New Defect Fluorite $ScVO_{3.5}$ Metastable Phase. *Dalton Trans.* **2004**, *8* (9), 1294–1297.

(17) Lundgren, R. J.; Cranswick, L. M. D.; Bieringer, M. In Situ X-Ray Powder Diffraction, Synthesis, and Magnetic Properties of $InVO_3$. *J. Solid State Chem.* **2006**, *179* (12), 3599–3606.

(18) Soderholm, L.; Greedan, J. E. Ferromagnetic Semiconductors: Magnetic Properties of the Pyrochlores, $(Y_xLu_{1-x})_2V_2O_7$ and $(Sc_xLu_{1-x})_2V_2O_7$. *Mater. Res. Bull.* **1979**, *14* (11), 1449–1455.

(19) Troyanchuk, I. O. Preparation and Properties of $R_2V_2O_7$ (R = Er, Ho, Y, Dy) with the Pyrochlore Structure. *Inorg. Mater.* **1990**, *26* (1), 182–183.

(20) Bazuev, G. V. Magnetic Properties of Solid Solutions in the Sc_2O_3 - V_2O_3 System. *Inorg. Mater.* **1972**, *8* (4), 729–732.

(21) Zhilyaev, V. Oxidation of Solid Solutions of Vanadium, Scandium, and Chromium Sesquioxides in Air. *Inorg. Mater.* **1972**, *8* (3), 576–577.

(22) Pokrovskii, B. I.; Isaeva, E. V. Structure Determination of Complex Oxides from X-Ray Powder Patterns by the Method of Concentration Waves (Superstructures Based on the Fluorite Lattice). *Acta Crystallogr.* **1978**, *34*, 1051–1059.

(23) Cong, H.; Zhang, H.; Yao, B.; Yu, W.; Zhao, X.; Wang, J.; Zhang, G. $ScVO_4$: Explorations of Novel Crystalline Inorganic Optical Materials in Rare-Earth Orthovanadate Systems. *Cryst. Growth Des.* **2010**, *10* (10), 4389–4400.

(24) Shafi, S. P.; Lundgren, R. J.; Cranswick, L. M. D.; Bieringer, M. Formation, Structure and Magnetism of the Metastable Defect Fluorite Phases $AVO_{3.5+x}$ (A = In, Sc). *J. Solid State Chem.* **2007**, *180* (12), 3333–3340.

(25) Shafi, S. P.; Kotyk, M. W.; Cranswick, L. M. D.; Michaelis, V. K.; Kroeker, S.; Bieringer, M. In Situ Powder X-Ray Diffraction, Synthesis, and Magnetic Properties of the Defect

Zircon Structure $ScVO_{4-x}$. *Inorg. Chem.* **2009**, *48* (22), 10553–10559.

(26) Goodenough, J. B. Oxide-Ion Electrolytes. *Annu. Rev. Mater. Res.* **2003**, *33* (1), 91–128.

(27) Foord, E. E.; Birmingham, S. D.; Demartin, F.; Pilati, T.; Gramaccioli, C. M.; Lichte, F. E. Thortveitite and Associated Sc-Bearing Minerals from Ravalli County, Montana. *Can. Mineral.* **1993**, *31* (2), 337–346.

(28) Castillo-Martinez, E.; Bieringer, M.; Shafi, S. P.; Cranswick, L. M. D.; Alario-Franco, M. A. Highly Stable Cooperative Distortion in a Weak Jahn-Teller d2 Cation: Perovskite-Type $ScVO_3$ Obtained by High-Pressure and High-Temperature Transformation from Bixbyite. *J. Am. Chem. Soc.* **2011**, *133* (22), 8552–8563.

(29) Shannon, R. D. Revised Effective Ionic Radii and Systematic Studies of Interatomic Distances in Halides and Chalcogenides. *Acta Crystallogr.* **1976**, *A32* (5), 751–767.

Chapter 5. Exploring the Polymorphs and Phase Transitions of $Y_xPr_{2-x}O_3$ Materials

Joey A. Lussier [a,b], Diego H. P. de Souza [a], Pamela S. Whitfield [c,‡], and Mario Bieringer [a,b]

[a] Department of Chemistry, University of Manitoba, Winnipeg, MB, R3T 2N2, Canada

[b] Manitoba Institute for Materials, University of Manitoba, Winnipeg, MB, R3T 2N2, Canada

[c] Spallation Neutron Source, Oak Ridge National Laboratory, Oak Ridge, Tennessee 37830, USA

[‡] Current address: Excelsus Structural Solutions, Park Innovaare, 5234 Villigen, Switzerland

Preface

This manuscript, which will soon be submitted for publication to Inorganic Chemistry, explores the structural diversity of the $Y_xPr_{2-x}O_{3+\delta}$ system. A continuation of the studies found in chapters 2 and 3, this is the first report of $Y_xPr_{2-x}O_{3+\delta}$ with structures other than bixbyite or defect fluorites. Focusing on the Pr-rich side of the solid solution ($x \leq 0.8$) allows for a more detailed analysis of the borders between phases in the cation radius vs. temperature plot often used to describe lanthanide sesquioxides. Furthermore, a comprehensive structural study using combined neutron and X-ray diffraction is undertaken, and oxidative processes are followed for all phases, *in-situ*.

Contributions

Ex-situ and oxidative studies of the series was undertaken by Diego H. P. de Souza in collaboration with Joey A. Lussier, *in-situ* neutron studies were completed by Joey A. Lussier. Pamela S. Whitfield, and Mario Bieringer. The manuscript was written by Joey A. Lussier and Mario Bieringer.

5.1. Abstract

We report, for the first time, members of the $Y_{2-x}Pr_xO_3$ system with non-bixbyite or defect fluorite structures. The synthesis, structure, phase transitions, and high temperature reactivity of the trigonal A-type and monoclinic B-type structures are reported along with those of the cubic C-type phase (bixbyite). Combined powder X-ray and neutron diffraction Rietveld refinements are used to report structural details of all 3 reported phases. Phase transitions are investigated, showing a clear dependence on average cation size. Using neutron diffraction phase transitions are followed *in-situ*, revealing that all phases are quenchable and non-reversible. *In-situ* powder X-ray diffraction experiments in flowing oxygen allow insights into mechanistic details of redox processes in the reported phases. In contrast to the C-type cubic bixbyite, the trigonal A-type and monoclinic B-type structures do not allow any oxygen uptake, displaying instead a phase transition to either the bixbyite C-type or defect fluorite structure before accepting more anions. The findings reported here can be used to fill the gaps in accepted lanthanide sesquioxide phase diagrams, thus allowing the prediction of structure types, and the synthetic control needed for rational design of functional materials.

5.2. Introduction

Transition metal and rare-earth oxides give access to diverse compositions and particular rich phase diagrams. The compositional and structural diversity permits to tune physical properties and gives access to a wide range of materials that can serve as valuable precursors for targeted synthesis of functional materials. Despite the many functional oxide materials the synthesis of solids is only poorly understood. The vast majority of materials that are prepared by high temperature solid-state syntheses are thermodynamically stable products. In recent years an increasing attention has been paid to the formation of kinetic products, often microwave synthesis, hydrothermal synthesis, high-pressure synthesis, and the sol-gel method, among others have allowed this trend to develop. With this increased access to novel phases, as well as improvement to computational predictions and machine learning techniques, it becomes even more important to explore phase diagrams and further understand how properties will be affected by the structure of the materials.

The series of lanthanide sesquioxides, Ln_2O_3, have been studied extensively[1–3], with the first noteworthy publication in 1925 by Goldschmidt et al.[4] Further crystallographic studies have been conducted, revealing a total of 5 polymorphs, two high-temperature polymorphs (> 2000 °C)[5] and three low-temperature polymorphs (< 2000 °C). The three low-temperature polymorphs are the trigonal A-type phase, the monoclinic B-type phase, and the cubic bixbyite C-type phase (these phases will be referred to as trigonal (A), monoclinic (B), and cubic bixbyite (C) from now onwards). They are believed to transition in the order C - B – A with increasing temperature.[1] The two high temperature polymorphs, H and X, are believed to be polymorphs derived from the trigonal (A) and cubic bixbyite (C) phases, respectively.[6]

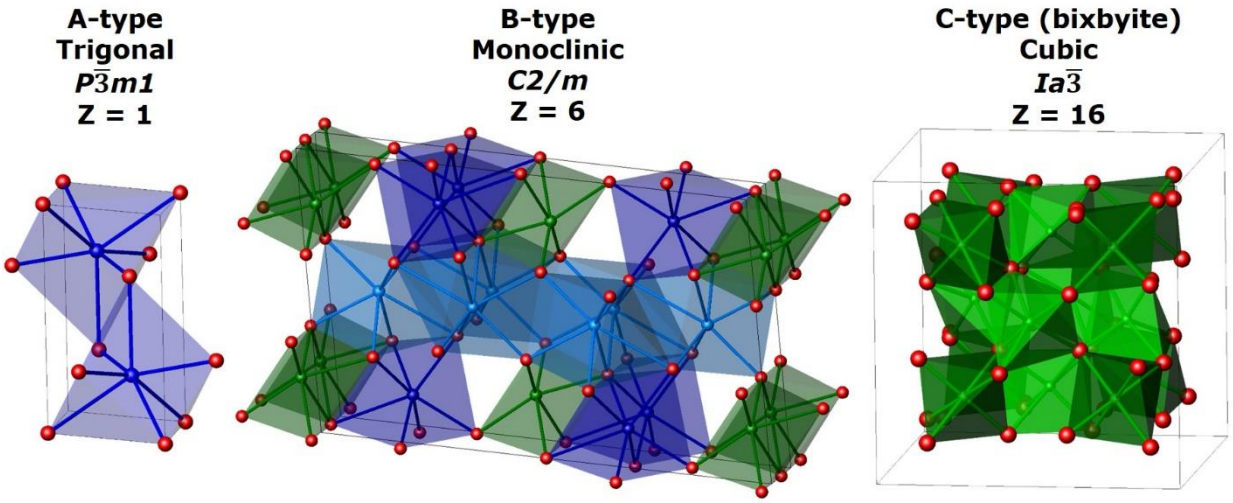

Figure 5.1: Illustration of the 3 low-temperature polymorphs of the Ln_2O_3 series found in the trigonal (A) (left), monoclinic (B) (center), and cubic bixbyite (C) (right) structures. Blue/green spheres = cations, red spheres = oxide; Blue polyhedra show 7-coordinated cations, green polyhedra represent 6-coordinated cations.

There has been a lot of controversy over the space group of the trigonal (A) phase,[7,8] however it is now widely accepted that the structure determined by Pauling is correct.[9] This polymorph crystallizes in space group $P\bar{3}m1$ (space group # 164) with the cations found fully occupying a *2d* site, while the anions fully occupy a *2d* and the *1a* site with one formula unit per unit cell. The cations are coordinated to 7 oxide anions. Pr_2O_3 is commonly found in this structure with a = 3.8589(1) Å, c = 6.0131(2) Å.[10] The monoclinic (B) phase crystallizes in space group *C2/m* (space group # 12) and is a distorted variant of the trigonal (A) structure. The monoclinic (B) polymorph contains 6 formula units in the unit cell with the cations in three different *4i* sites. The anions fully occupy 5 different crystallographic sites; four in *4i* positions, and one in the *2b* position. The cubic bixbyite (C) phase has 16 formula units per unit cell and crystallizes in the cubic space group $Ia\bar{3}$ (space group # 206). The cations are located in the *8b* and *24d* sites, and the anions fully occupy the *48e* site. Y_2O_3 is an example of a cubic bixbyite (C) sesquioxide with a = 10.6106(15) Å.[11] These three polymorphs are illustrated in figure 5.1.

The trigonal (A), monoclinic (B), cubic bixbyite (C) structures are all related to the cubic fluorite, CaF_2, structure. The cubic fluorite structure crystallizes in space group $Fm\bar{3}m$ (space group # 225) with a single cation site (*4a*) and a single anion site (*8c*). The cations are eight-fold coordinated with anions, forming regular cubes which share all edges. The cubic bixbyite (C)-type structure is related to the fluorite by removing 25% of the anions, forming all six-fold coordinated cations. This results in the situation where one quarter of the cubes are missing anions along the body diagonal, and three quarters are missing anions along the face diagonal. In the case of the trigonal (A)-type structure, the anion lattice of the fluorite remains intact and the cations are moved into interstitial sites, shearing in regular intervals. This creates the seven-fold coordination. The monoclinic (B)-type is simply a distortion of the trigonal (A)-type, which changes the environment around the cations to a mixture of six- and seven-fold coordination.[1]

The lanthanide sesquioxide phase diagram, first published by Föex and Traverse[5], and later improved by Atkinson[12] (figure 5.2) shows clear trends based on cation size. However due to the lack of available lanthanide sesquioxides, a large number of

Figure 5.2 has been removed by the author due to copyright concerns. Figure is available from university of Salford Institutional Repository:

http://usir.salford.ac.uk/id/eprint/30746

Page 208, Figure 9.1

Figure 5.2: Lanthanide sesquioxide phase diagram as presented by Atkinson.[12]

unknown regions are found in the diagram, specifically at the boundaries between the phases. In order to further explore this phase diagram a two-cation system (i.e. ABO_3) can be used. Furthermore, using a continuous solid solution ($A_{2-x}B_xO_3$) allows tuning of the average cation size in order to select different regions of the phase diagram. Adding a second cation allows for the possible presence of different cation and anion ordering schemes. In addition to the five known lanthanide sesquioxide phases, corundum, ilmenite, and a number of perovskite structures are possible, among others. Ionic radii ratios are often used to predict the structures of these systems, where similar A and B cation sizes will often yield a cubic bixbyite (C) phase. Care must be taken to select a system which can mimic the lanthanide sesquioxides.

The disordered cation sites found in the cubic bixbyite (C) solid solution $Y_{2-x}Pr_xO_3$, along with the difference in size between the cations spanning from 0.99 Å (Pr^{3+} (VI)) to 0.9 Å (Y^{3+} (VI)), make it an ideal candidate to explore this phase diagram more fully. The $Y_{2-x}Pr_xO_3$ solid solution has been reported as fully reduced cubic bixbyites (C) in thin films synthesized by molecular beam epitaxy[13–16], and bulk samples which were made via a sol-gel method.[17] Furthermore, the bulk samples studied by Lussier, et al. explored the oxidation of the bixbyite starting materials to fluorites.

Here, we are reporting the formation of the first trigonal (A) and monoclinic (B)-type $Y_xPr_{2-x}O_3$ materials. A full structural characterization of both phases using time-of-flight powder neutron diffraction and powder X-ray diffraction is described. This is made possible due to the favorable contrast in scattering length (b(Y) = 7.75 fm; b(Pr) = 4.58 fm; b(O) = 5.803 fm).[18] A systematic study of the phase transitions throughout the series is confirmed using high temperature *in-situ* neutron powder diffraction at POWGEN. This allows for a more detailed look at the effect of

cation size on the phases of sesquioxide materials which can in turn, help to predict expected phases. Furthermore, oxidation reactions are explored in detail using *in-situ* powder X-ray diffraction in order to understand the redox processes of the trigonal (A)-, monoclinic (B)-, and cubic bixbyite (C)-type phases during oxidation.

5.3. Experimental

5.3.1. Synthesis

Bulk samples of parent materials $Y_xPr_{2-x}O_{3+\delta}$ (x= 0.05, 0.10, 0.15, 0.20, 0.40, 0.60, and 0.80) were prepared using stoichiometric amounts of calcined Y_2O_3 (Cerac, 99.999% purity) and Pr_6O_{11} (Alfa Aesar, 99.996% purity) via the citrate sol-gel method as previously outlined by Lussier, et al.[19,17] Parent materials were reduced at 500 °C for 12 hours in 3-5% H_2 (balance N_2). All samples were confirmed to be phase pure cubic bixbyite (C) phases by powder X-ray diffraction (section 5.3.2.1).

Trigonal (A) $Y_{0.05}Pr_{1.95}O_{3.00}$ and monoclinic (B) $Y_{0.2}Pr_{1.8}O_3$ were obtained by heating the cubic bixbyite (C) parent compound to 1200 °C for 24 hours under 3-5% H_2 (balance N_2) in order to prevent reoxidation. The phase pure trigonal (A) and monoclinic (B) materials crystallize as a green powders.

Temperature-dependent *ex-situ* experiments were carried out on approximately 200 mg of each cubic bixbyite (C) sample which were heated to 600 °C for 12 hours under 3-5% H_2 (balance N_2) in order to prevent reoxidation. This process was repeated in 100 °C increments up to 900 °C followed by 50 °C increments up to 1300 °C. Powder X-ray diffraction was conducted at each step in order to determine phases present.

5.3.2. Characterization

5.3.2.1. *Laboratory Powder XRD at Room Temperature*

Room Temperature powder X-ray diffraction was collected using Cu Kα radiation (λ ($K\alpha_1$) = 1.540598 Å, and λ ($K\alpha_2$) = 1.544426 Å) on a PANalytical X'Pert Pro diffractometer in Bragg-Brentano geometry (PANalytical B.V., Almelo, the Netherlands).The measurements were carried out using a 1° divergence slit, 10 mm mask, and 0.04 rad soller slits for the primary beam and a Ni filter and 0.04 rad soller slits for the diffracted beam. Samples were cast as acetone slurries in order to mount thin layers on a zero background sample holder (Si (510)). They were measured on a spinning sample stage at 1 Hz and data were collected with 0.0167° steps covering a 2θ range from 15° to 145° at 120 s/step counting time for Rietveld refinements. The diffractometer line profiles were confirmed with NIST standard LaB_6 SRM 660a, and peak positions were confirmed with NIST standard Si SRM 640b.

5.3.2.2. *Synchrotron Powder XRD at Room Temperature*

Room temperature high resolution synchrotron diffraction data were collected using beamline 11-BM at the Advanced Photon Source (APS), Argonne National Laboratory in Argonne, Illinois. The instrument is described elsewhere.[20] A Kapton capillary (ø = 0.8mm) was coated with the sample and data were collected with an average wavelength of 0.459990 Å out to 2θ = 40˚ in 0.001˚ steps using a scan rate of 0.1 ˚/s. A mixture of NIST standard reference materials, Si (SRM 640c) and Al_2O_3 (SRM 676) were used to calibrate the instrument.

5.3.2.3. *Room-Temperature Neutron Powder Diffraction*

Preliminary neutron powder diffraction data were collected on the trigonal (A) phase using the POWGEN diffractometer, at the Spallation Neutron Source (SNS) at Oak Ridge National Laboratory in Oak Ridge, Tennessee. Approximately 0.7 grams of sample was loaded into an 8mm diameter cylindrical vanadium sample can. Using a center wavelength of 1.333 Å with a d-spacing range from 0.41 Å to 5.37 Å, data were collected for approximately one hour using a slit width of 20 mm and a slit height of 35 mm.

Preliminary neutron powder diffraction data were collected on the monoclinic (B) phase using the Nanoscale Order MAterials Diffractometer (NOMAD)[21] instrument at the SNS, Oak Ridge National Laboratory in Oak Ridge, Tennessee. Approximately 150 mg of powder was loaded in a 3 mm diameter quartz capillary and sealed with wax. The capillary was loaded in the sample shifter carousel at the NOMAD instrument at the Spallation Neutron Source and aligned. Data were collected at 300 K (controlled by an Argon cryostream) for a total of 1 hour at 60 Hz setting. The NOMAD data reduction programs were used to normalize collected spectra, subtract background and container scattering signals, and produce histograms appropriate for Rietveld analysis.

5.3.2.4. *High-Temperature in-situ Powder X-ray Diffraction*

High temperature *in-situ* powder X-ray diffraction experiments were carried out using the same diffractometer described in section 5.3.2.1, where samples were mounted as an acetone slurry directly on a 10mm platinum resistive strip heater within a self-masking Anton Paar HTK2000 high temperature camera (Anton Paar GmbH). The furnace is reliable within 5 °C up to temperatures of 1300 °C. X-ray diffractograms were collected in increments of 10 °C from 25 °C

to 625 °C. Data were collected with 0.0167° steps covering 25° ≤ 2θ ≤ 35° with 100 s/step counting time for a total of 10 minutes at each temperature.

5.3.2.5. *High-Temperature Neutron Powder Diffraction*

High temperature neutron powder diffraction experiments were carried out using the POWGEN diffractometer. Approximately 1 gram of samples were loaded into cylindrical vanadium ILL furnace sample cans and inserted into an ILL furnace. This furnace is kept at a vacuum level of approximately $2x10^{-5}$ torr and uses vanadium heating elements in order to reach temperatures of 1200 °C. Data were collected using a center wavelength of 1.333 Å with a d-spacing range from 0.41 Å to 6.14 Å for sample compositions of x = 0.05 and x = 0.20. For composition x = 0.10, a center wavelength of 2.665 Å with a d-spacing range from 1.10 Å to 10.52 Å. Samples were heated at a rate of 300 °C/hour to 800 °C, before slowing the heating rate to 60 °C/hour (for x = 0.05, 0.20) or 20 °C/hour (for x = 0.10) up to a final temperature of 1200 °C. Diffraction data were collected continuously throughout the heating profile, allowing for post processing of data using the MANTID software.[22] For Rietveld refinements, data were binned in 10 °C increments, and for contour plots they were binned in 5 °C increments.

5.3.3. Rietveld Refinements

Rietveld refinements in sections 5.4.1 and 5.4.3 were carried out using the *Topas (version 5)* software. The crystallographic structures of each phase were refined simultaneously against powder X-ray and time-of-flight neutron diffraction data. Optimized parameters include background coefficients, peak shapes and asymmetries, unit cell parameters, atomic positions, and temperature factors (both isotropic and anisotropic). Using these structures as starting points,

Rietveld refinements were carried out against i*n-situ* high-temperature TOF neutron powder diffraction data, with a primary focus on determining phases present and retrieving phase fractions.

Rietveld refinements in section 5.4.2 were carried out using the Rietveld package FullProf.2k[23] with a particular focus on identifying phases present and phase fractions. The background was described using linearly interpolated background points, and optimized parameters include unit cell dimensions, peak shapes, and atomic positions. Phase fractions were extracted and reported as a function of temperature.

5.4. Results and Discussion

5.4.1. Structure determinations

In order to describe the series of phase transitions in the $Y_xPr_{2-x}O_3$ system, a full structural characterization of the 3 expected structures is necessary. As far as the authors know, this represents the first time yttrium doped praseodymium oxide has been seen in either the trigonal (A) or monoclinic (B) structures.

The structural information for the cubic bixbyite (C) phase of the full solid solution $Y_xPr_{2-x}O_3$ has been described in detail elsewhere.[17,19]

The trigonal (A) $Y_{0.05}Pr_{1.95}O_3$ was obtained by heating the bixbyite parent compound in a flow of 3% hydrogen at 1200 °C. The structure was refined against neutron powder diffraction data from POWGEN, and laboratory X-ray powder diffraction data. This phase crystallizes in the trigonal space group $P\bar{3}m1$ (space group # 164) with a = 3.84973(4) Å and c = 6.01128(9) Å. 24 parameters were refined including: lattice parameters, atomic coordinates, thermal parameters, background coefficients, and peak shape functions. Figure 5.3(i) shows the Rietveld plots for the trigonal (A) refinement of $Y_xPr_{2-x}O_3$. The Y^{3+} and Pr^{3+} are fully disordered on the cation site (*2d*)

and the anions fully occupy the *2d* and *1a* sites. The metal ions are 7-fold coordinated with 3 bonds each at 2.3102(4) Å and 2.6719(6) Å, and 1 bond of 2.4155(14) Å. This structure agrees well with the Pr_2O_3 structure reported by Greis et al.[10] with slightly smaller unit cell parameters and bond lengths in agreement with the smaller cation size of the Y-dopant. Table 5.1 summarizes the structural details refined for this phase.

The monoclinic (B) $Y_{0.2}Pr_{1.8}O_3$ was similarly obtained by heating the bixbyite parent compound in flowing 3% hydrogen at 1200 °C. Figure 5.3(ii) shows the Rietveld plots of the synchrotron X-ray (11-BM) and time-of-flight neutron (NOMAD) data for $Y_{0.2}Pr_{1.8}O_3$, and the structural details are listed in table 5.2. This sample crystallizes in the monoclinic C2/m space group (space group # 12) with a = 14.34187(6) Å, b= 3.69744(2) Å, c=8.98836(4) Å, and β = 100.3793(3) °. Cation sites 1 and 2 are 7-fold coordinated with 6 regular bonds and one long bond, while cation site 3 is typically considered 6-fold coordinated due to its much longer 7th bond (3.088(3) Å). In this refinement the overall cation ratio was set to 1:9 Y:Pr and the cations were allowed to refine over the three *4i* cation positions. The yttrium shows a significant (~5x) preference for the cation site 3. This preference is likely due to the size difference between Y^{3+} (r(VI) = 0.9 Å and Pr^{3+} (r(VI) = 0.99 Å);[24] where the larger Pr^{3+} cation prefers the large cavities provided by 7-fold coordinated cation sites 1 and 2 and the Y^{3+} cation prefers the smaller cavity provided by the 6-coordinated cation site 3.

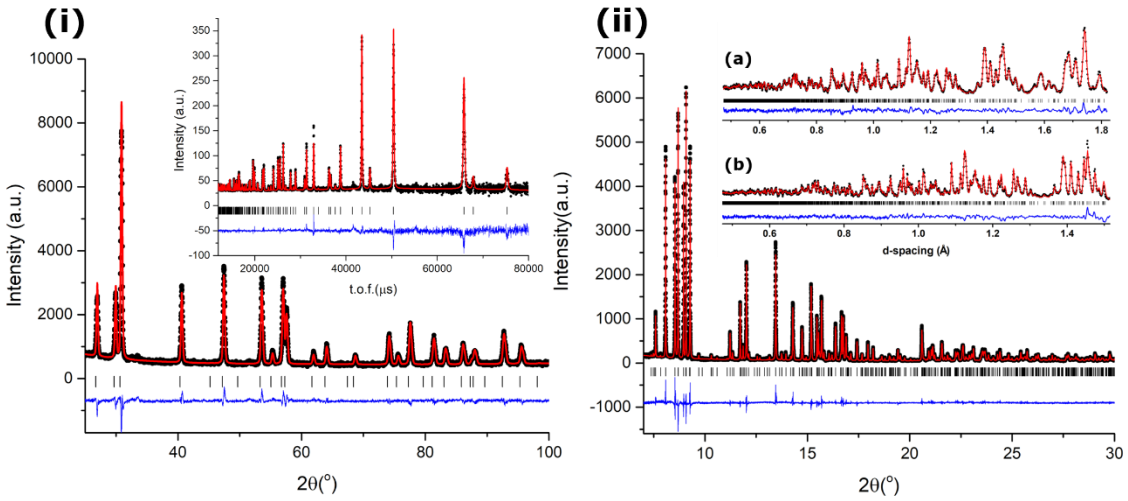

Figure 5.3: Rietveld plots for the refinement of (i) the trigonal (A) structure $Y_{0.05}Pr_{1.95}O_3$ (main) Laboratory X-ray data (inset) time-of-flight neutron diffraction data from POWGEN, (ii) the monoclinic (B) structure $Y_{0.2}Pr_{1.8}O_3$ (main) synchrotron X-ray data (insets) time-of-flight neutron diffraction data from NOMAD showing (a) the 122° bank and (b) the 154° bank. Black symbols = observed data, red line = fit, blue line = difference, tick marks = Bragg positions.

Table 5.1: Structural Parameters for the trigonal (A) phase of $Y_{0.05}Pr_{1.95}O_{3.00}$. Values were obtained from a simultaneous Rietveld refinement against powder X-ray diffraction data and time-of-flight powder neutron data measured at room temperature.

Composition		$Y_{0.05}Pr_{1.95}O_{3.00}$
Space Group		$P\bar{3}m1$ (164)
Unit Cell	a (Å) c (Å) V (Å^3) Z V/Z (Å^3)	3.84974(4) 6.01129(9) 77.154(2) 1 77.154(2)
Y/Pr (*2d*) (1/3, 2/3, z)	z/c B_{iso} (Å^2)	0.2467(2) 0.0294(94)
O1 (*2d*) (1/3, 2/3, z)	z/c B_{iso} (Å^2)	0.6485(2) 0.69(2)
O2 (*1a*) (0, 0, 0)	B_{iso} (Å^2)	0.76 (3)
Bond Lengths	Y/Pr – O1 Y/Pr – O1 Y/Pr – O2	3 x 2.3102(4) 1 x 2.4155(14) 3 x 2.6719(6)
χ^2:	Overall Neutron (T.O.F.)[a] X-ray (Cu kα)[b]	1.56 1.52 1.58

[a]Neutron T.O.F range: 12000 – 116000 μs, 5672 data points
[b]X-ray λ ($K\alpha_1$) = 1.540598 Å, and λ ($K\alpha_2$) = 1.544426 Å, 25° ≤ 2θ ≤ 145°, Δ2θ = 0.0167°, 7180 data points

Table 5.2: Structural Parameters for the monoclinic (B) phase of $Y_{0.20}Pr_{1.80}O_{3.00}$. Values were obtained from a simultaneous Rietveld refinement against synchrotron powder X-ray diffraction data and time-of-flight powder neutron data measured at room temperature.

Composition		$Y_{0.20}Pr_{1.80}O_{3.00}$
Space Group		C2/m (12)
Unit Cell	a (Å) b (Å) c (Å) β (°) V (Å^3) Z V/Z (Å^3)	14.34187(6) 3.69744(2) 8.98837(4) 100.3793(3) 468.838(3) 6 78.140(1)
Y/Pr1 (*4i*) (x, 0, z)	x/a z/c Y Occupancy (%) Pr Occupancy (%) B_{iso} (Å^2)	0.63462(5) 0.49259(7) 4.4(5) 95.6(5) 0.65(2)
Y/Pr2 (*4i*) (x, 0, z)	x/a z/c Y Occupancy (%) Pr Occupancy (%) B_{iso} (Å^2)	0.68987(5) 0.13841(8) 3.7(5) 96.3(5) 0.51(2)
Y/Pr3 (*4i*) (x, 0, z)	x/a z/c Y Occupancy (%) Pr Occupancy (%) B_{iso} (Å^2)	0.96600(6) 0.18854(9) 21.8(6) 78.2(6) 0.72(2)
O1 (*4i*) (x, 0, z)	x/a z/c B_{iso} (Å^2)	0.1310(1) 0.2887(2) 1.21(3)
O2 (*4i*) (x, 0, z)	x/a z/c B_{iso} (Å^2)	0.8255(1) 0.0253(2) 0.95(3)
O3 (*4i*) (x, 0, z)	x/a z/c B_{iso} (Å^2)	0.8015(2) 0.3679(3) 1.99(3)
O4 (*4i*) (x, 0, z)	x/a z/c B_{iso} (Å^2)	0.4748(1) 0.3416(2) 1.05(3)
O5 (*2b*) (0, 1/2, 0)	B_{iso} (Å^2)	1.74(6)
Bond Lengths:	Y/Pr1 – O3 Y/Pr1 – O4 Y/Pr1 – O4 Y/Pr1 – O1 Y/Pr1 – O3	2 x 2.327(1) 1 x 2.351(2) 1 x 2.444(2) 2 x 2.597(1) 1 x 2.820(2)

	Y/Pr1 – O average	2.495
	Y/Pr2 – O2 Y/Pr2 – O2 Y/Pr2 – O3 Y/Pr2 – O1 Y/Pr2 – O5 Y/Pr2 – O average	2 x 2.349(1) 1 x 2.352(2) 1 x 2.373(2) 2 x 2.523(1) 1 x 2.783(1) 2.465
	Y/Pr3 – O2 Y/Pr3 – O4 Y/Pr3 – O1 Y/Pr3 – O5 Y/Pr3 – O average	1 x 2.268(2) 2 x 2.294(1) 1 x 2.375(2) 2 x 2.613(1) 2.410
χ^2:	Overall Neutron (T.O.F.)[a] X-ray (λ = 0.459990 Å)[b]	1.30 1.14, 2.10, 1.37, 1.60 1.23

[a]Neutron T.O.F: 4 histograms - range: 850 – 25000 μs, 7835 data points
[b]X-ray λ = 0.459990 Å, $5.7° \leq 2\theta \leq 38.5°$, $\Delta 2\theta = 0.0001°$, 32803 data points

5.4.2. Ex-situ heating experiments

Cubic bixbyite (C) starting materials were synthesized for the solid solution of $Y_xPr_{2-x}O_3$ ($x \leq 0.8$) using the method presented in section 5.3.1. All reduced samples crystallize in the phase pure bixbyite structure with space group *Ia-3* (space group # 206).

These starting materials were heated in 100 °C steps to 900 °C followed by 50 °C steps to 1300 °C in flowing 3-5% H_2 in order to prevent oxidation. After each heating room temperature powder X-ray diffractograms were collected. The Rietveld analysis of those data allowed the determination of phase compositions. Table 5.3 shows the refined phase percentage of three phase refinements (trigonal (A), monoclinic (B), and cubic bixbyite (C)) for each powder X-ray diffractogram. Figure 5.4(a) shows the phase evolution for $Y_{0.05}Pr_{1.95}O_3$ where the cubic bixbyite (C) to trigonal (A) transition similar to that of Pr_2O_3 is seen. This transition occurs after heating the sample to 900 °C and therefore, one can deduce that the phase transition occurs between 800 °C and 900 °C.

The phase evolution for $Y_{0.2}Pr_{1.8}O_3$, however, shows a transition directly from the cubic bixbyite (C) phase to the monoclinic (B) phase. This transition begins after the heating at 950 °C, where a small fraction of the monoclinic (B) phase is found. After heating at 1000 °C the monoclinic (B) phase is the majority phase, and is essentially phase pure (97%) by 1050 °C. Figure 5.4(d) graphically represents this phase evolution.

For $Y_xPr_{2-x}O_3$ where $0.05 < x < 0.20$, shown in figure 5.4(b) ($x = 0.10$) and figure 5.4(c) ($x = 0.15$), a more complex phase evolution exists. In both cases, as the temperature increases the cubic bixbyite (C) phase is converted to both the trigonal (A) and monoclinic (B) phases, forming a 3-phase region. For $x = 0.10$, the newly formed monoclinic (B) phase is converted to the trigonal (A) phase upon further heating, and a phase pure trigonal (A) trigonal phase is found above 1200 °C. Where $x = 0.15$, as the temperature is increased further, the monoclinic (B) phase begins to replace the trigonal (A). Upon further heating, however, the trigonal (A) phase begins to replace the monoclinic (B) up to the maximum temperature reached, 1300 °C, where an approximately equal mixture of the phases is found.

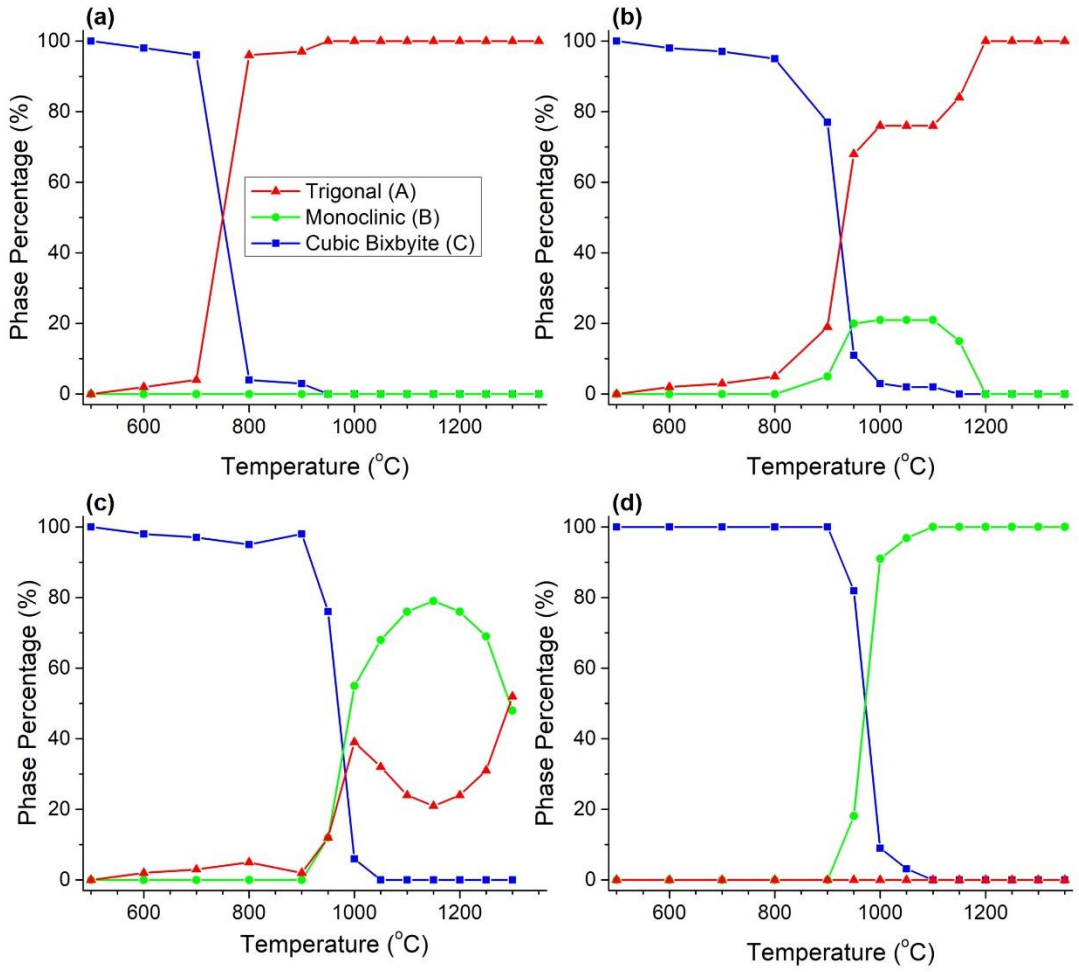

Figure 5.4: Phase percentages derived from Rietveld refinements against room temperature X-ray diffraction data after 12 hour heatings of $Y_xPr_{2-x}O_3$, x = (a) 0.05, (b) 0.10, (c) 0.15, and (d) 0.20. Red triangles represent the trigonal (A) phase, green circles represent the monoclinic (B) phase, and blue squares represent the cubic bixbyite (C) phase.

Table 5.3: Refined phase percentage of the trigonal (A), monoclinic (B), and cubic bixbyite (C) phases at each step in the *ex-situ* experiment. Shaded regions show samples which are phase pure within 5% (the approximated error): (red) trigonal (A), (green) monoclinic (B), and (blue) cubic bixbyite (C).

T ↓	x →	0.05	0.10	0.15	0.20	0.40	0.60	0.80
500 °C	A-type	0%	0%	0%	0%	0%	0%	0%
	B-type	0%	0%	0%	0%	0%	0%	0%
	C-type	100%	100%	100%	100%	100%	100%	100%
600 °C	A-type	2%	2%	2%	0%	0%	0%	0%
	B-type	0%	0%	0%	0%	0%	0%	0%
	C-type	98%	98%	98%	100%	100%	100%	100%
700 °C	A-type	4%	3%	3%	0%	0%	0%	0%
	B-type	0%	0%	0%	0%	0%	0%	0%
	C-type	96%	97%	97%	100%	100%	100%	100%
800 °C	A-type	96%	5%	5%	0%	0%	0%	0%
	B-type	0%	0%	0%	0%	0%	0%	0%
	C-type	4%	95%	95%	100%	100%	100%	100%
900 °C	A-type	97%	19%	2%	0%	0%	0%	0%
	B-type	0%	5%	0%	0%	0%	0%	0%
	C-type	3%	77%	98%	100%	100%	100%	100%
950 °C	A-type	100%	68%	12%	0%	0%	0%	0%
	B-type	0%	20%	12%	14%	14%	0%	0%
	C-type	0%	11%	76%	86%	86%	100%	100%
1000 °C	A-type	100%	76%	39%	0%	0%	0%	0%
	B-type	0%	21%	55%	91%	88%	11%	0%
	C-type	0%	3%	6%	9%	12%	89%	100%
1050 °C	A-type	100%	76%	32%	0%	0%	0%	0%
	B-type	0%	21%	68%	97%	100%	72%	7%
	C-type	0%	2%	0%	3%	0%	28%	93%
1100 °C	A-type	100%	76%	24%	0%	0%	0%	0%
	B-type	0%	21%	76%	100%	100%	96%	37%
	C-type	0%	2%	0%	0%	0%	4%	63%
1150 °C	A-type	100%	84%	21%	0%	0%	0%	0%
	B-type	0%	15%	79%	100%	100%	100%	92%
	C-type	0%	0%	0%	0%	0%	0%	8%
1200 °C	A-type	100%	100%	24%	0%	0%	0%	0%
	B-type	0%	0%	76%	100%	100%	100%	100%
	C-type	0%	0%	0%	0%	0%	0%	0%
1250 °C	A-type	100%	100%	31%	0%	0%	0%	0%
	B-type	0%	0%	69%	100%	100%	100%	100%
	C-type	0%	0%	0%	0%	0%	0%	0%
1300 °C	A-type	100%	100%	52%	0%	0%	0%	0%
	B-type	0%	0%	48%	100%	100%	100%	100%
	C-type	0%	0%	0%	0%	0%	0%	0%

The cubic bixbyite (C) to monoclinic (B) transition for $Y_xPr_{2-x}O_3$ with $0.2 \leq x \leq 0.80$ are shown in figure 5.5 as phase fractions upon heating. No trigonal (A) phase is found at any point in the heating of these materials. The transition for x = 0.2 and x = 0.4 occur at similar temperatures; however, as x increases further, higher temperatures are required for the transition.

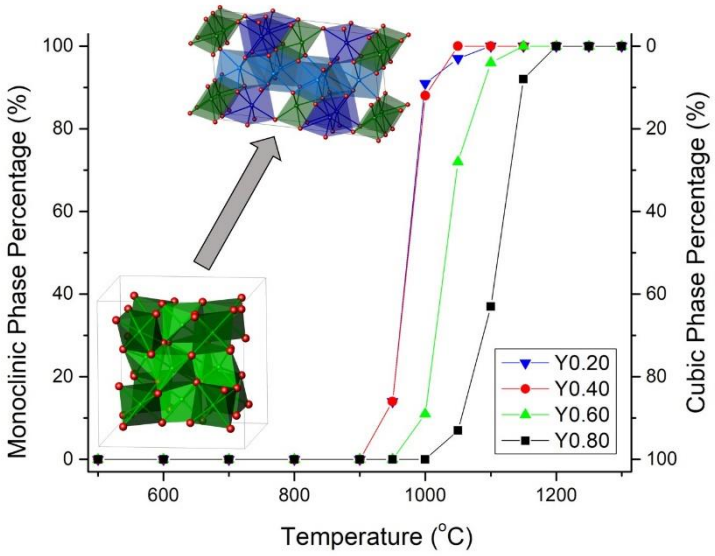

Figure 5.5: Phase percentages of the cubic bixbyite (C) phase vs. monoclinic (B) phase derived from Rietveld refinements against room temperature X-ray diffraction data after 12 hour heatings of $Y_xPr_{2-x}O_3$, x = 0.20 (blue triangles), 0.40 (red circles), 0.60 (green triangles), and 0.80 (black squares).

Combining this data into a phase diagram emphasizes the complexity of the series, due to the bi- and tri-phasic regions. Figure 5.6 shows an RGB colour map of the phase diagram, where the cubic bixbyite (C) phase is blue, the monoclinic (B) phase is green, and the trigonal (A) phase is red. The black lines have been added as guides to the eye to aid in the definition of the phase boundaries. When comparing the phase diagram explored here with that of the lanthanide sesquioxide series reported by Atkinson,[12] it is clear that the average cation size is the biggest factor in determining the phase of the material. This can allow synthetic chemists to predict

structures based on their cation sizes, and will allow for the design of materials with desired structures by mixing cations.

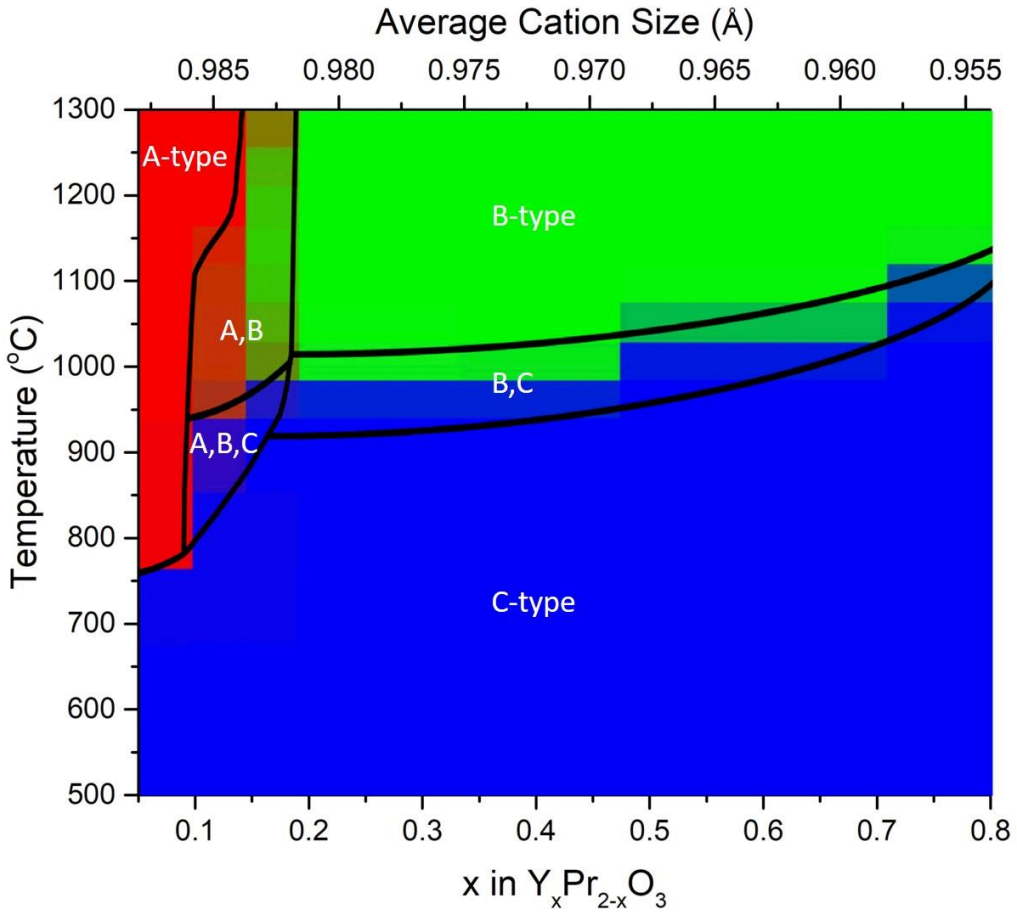

Figure 5.6: RGB colour map of the phases found during ex-situ heating experiments. Red = trigonal (A), Green = monoclinic (B), and Blue = cubic bixbyite (C). The black lines do not represent a fit to the data and are a guide to the eye only.

5.4.3. *In-situ* heating experiments

In order to better understand the phase transitions explored in section 5.4.2, *in-situ* high temperature neutron diffraction was utilized on the POWGEN diffractometer. Cubic bixbyite (C)starting materials of $Y_xPr_{2-x}O_3$ (x = 0.05, 0.1, and 0.2) were quickly heated (~300 °C/hour) under vacuum to approximately 800 °C before heating more slowly from 800 °C to 1200 °C.

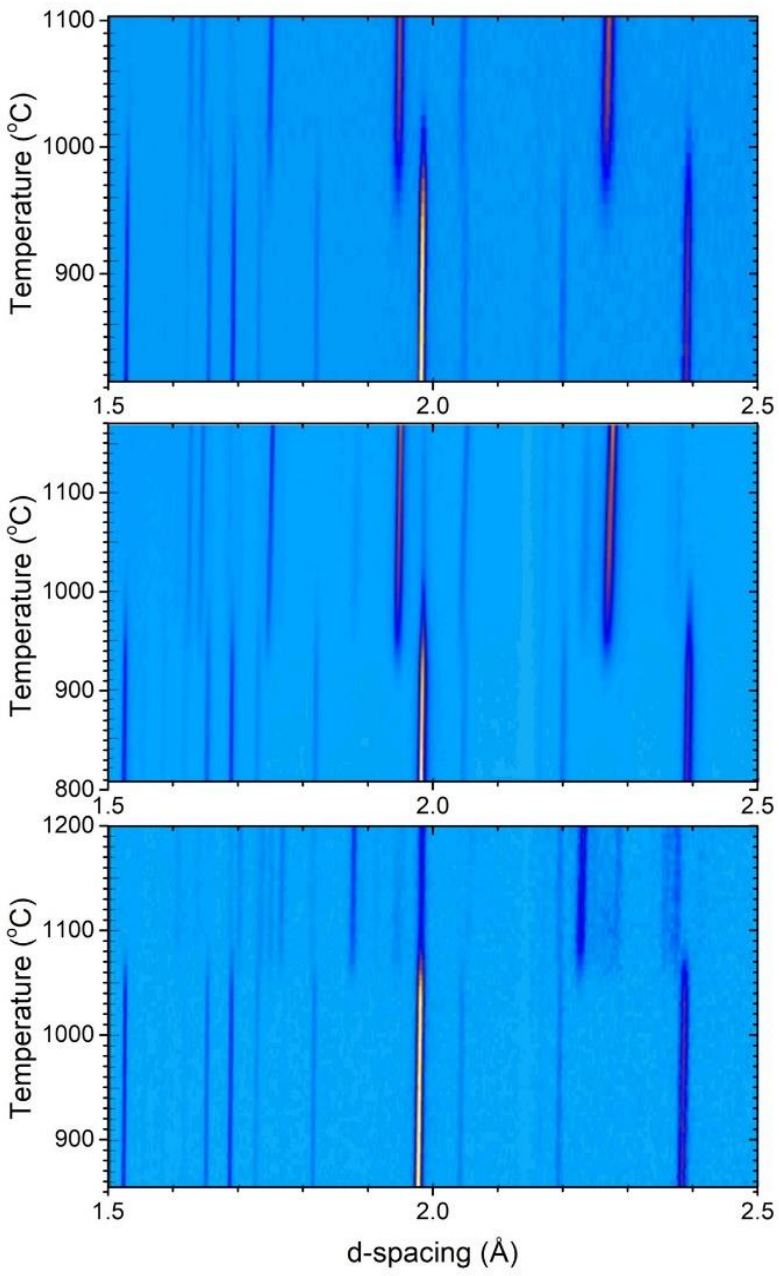

Figure 5.7: Contour plots of high-temperature neutron powder diffraction data under vacuum showing the phase transitions of (a) $Y_{0.05}Pr_{1.95}O_3$, (b) $Y_{0.1}Pr_{1.9}O_3$, and (c) $Y_{0.2}Pr_{1.8}O_3$.

Contour plots for each composition are shown in figure 5.7. Data was binned in 10 °C slices for full Rietveld refinements, where phase percentages were refined and plotted against temperature for each composition (

figure 5.88). $Y_{0.05}Pr_{1.95}O_3$ shows a transition from the cubic bixbyite (C) phase to the trigonal (A) phase beginning at 930 °C completing the transition by approximately 1050 °C. Between 930 °C and 1050 °C the two phases coexist with varying phase percentages. For the composition $Y_{0.2}Pr_{1.8}O_3$, the cubic bixbyite (C) phase persists to higher temperature, 1020 °C, before a phase transition to the monoclinic (B) monoclinic phase begins, completing by 1090 °C. The x = 0.1 composition shows a phase transition from the cubic bixbyite (C) phase to the trigonal (A) phase beginning at 890 °C, above 920 °C the monoclinic (B) phase also begins to form. The

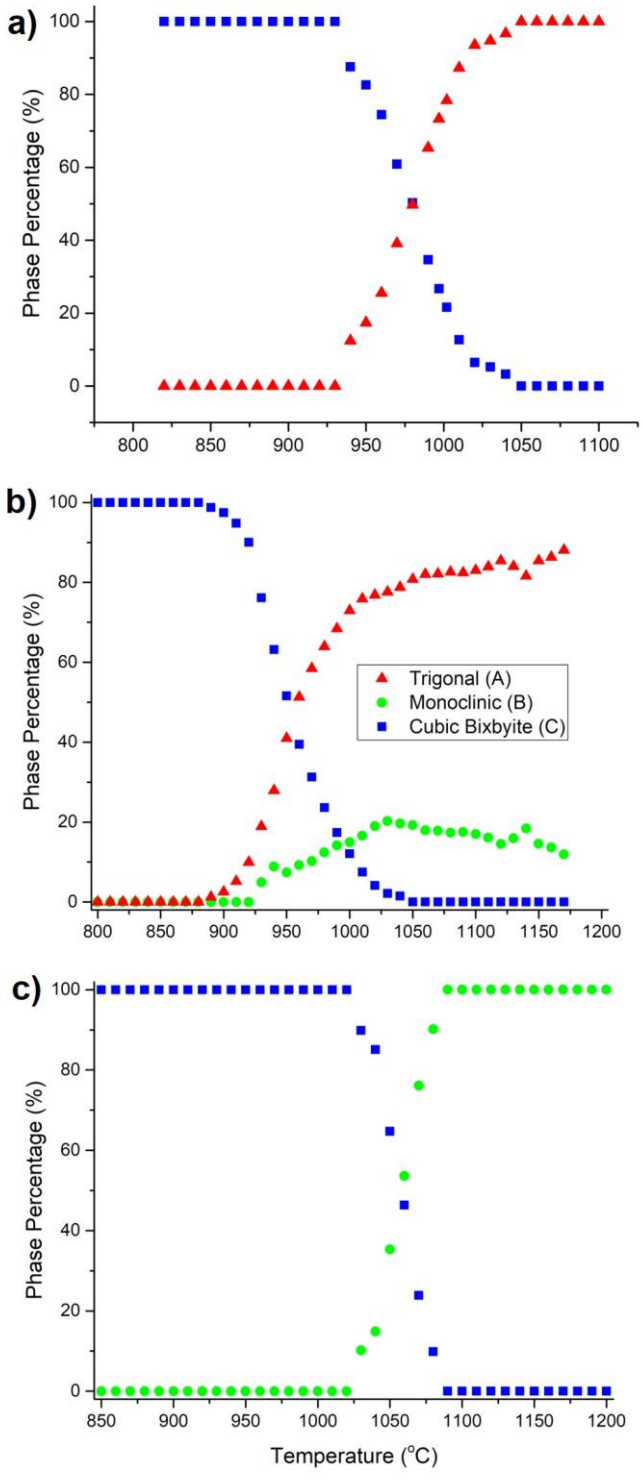

Figure 5.8: Phase percentages derived from Rietveld refinements against in-situ neutron powder diffraction data of $Y_xPr_{2-x}O_3$, x = (a) 0.05, (b) 0.10, and (c) 0.20. Red triangles represent the trigonal (A) phase, green circles represent the monoclinic (B) phase, and blue squares represent the cubic bixbyite (C) phase.

weight percent of the trigonal (A) and monoclinic (B) phases both increase up to approximately 1030 °C where the trigonal phase continues to increase, while the monoclinic phase fraction begins to decrease. The cubic bixbyite (C) phase is no longer visible after 1050 °C, however the monoclinic (B) phase persists up to the end of the experiment.

Although the trends seen in the *in-situ* results are consistent with the *ex-situ* results presented in section 5.4.2, the temperatures reported in the *in-situ* experiment are consistently higher than those reported for the ex-situ. Therefore, one would expect that if further heating was possible, the monoclinic (B) $Y_{0.1}Pr_{1.9}O_3$ would continue to decrease in phase percentage, and the phase pure trigonal (A) phase would result. The consistency between *ex-situ* and *in-*

situ results suggest that all phases are quenchable, and that the phase transitions in the $Y_xPr_{2-x}O_3$ series are non-reversible.

5.4.4. *In-situ* oxidation experiments

Because the trigonal (A), monoclinic (B), and cubic bixbyite (C) phases are all related to the cubic fluorite structure, upon oxidation at high temperature, Pr^{3+} will oxidize to Pr^{4+} forming fluorite structures. The oxidation pathways of these materials were explored further using high temperature *in-situ* powder X-ray diffraction experiments in flowing oxygen. This allows for speculations on mechanistic details during the oxidative processes. Oxidation of all 3 phases occurs in the same temperature range between 250 °C and 300 °C. Figure 5.9a and c shows the (222) and (400) peak of the cubic bixbyite (C) phase which shifts continuously to higher angle upon oxidation as they become the (111) and (200) peaks of the cubic fluorite phase. Furthermore, the disappearance of the (411) superstructure peak belonging to the bixbyite phase indicates the fluorite phase is being formed. This continuous shift shows that the cubic bixbyite (C) phase can accommodate extra oxides in its structure. During oxidation of the trigonal (A) and monoclinic (B) phases (figure 5.9), no peak shifts are visible, instead, an oxidative transition to the defect fluorite phase followed by a topotactic oxidation is seen. This suggests that the trigonal (A) and monoclinic (B) phases are not susceptible to additional oxides in their structures, and a phase transition must be realized before any additional anions can be added.

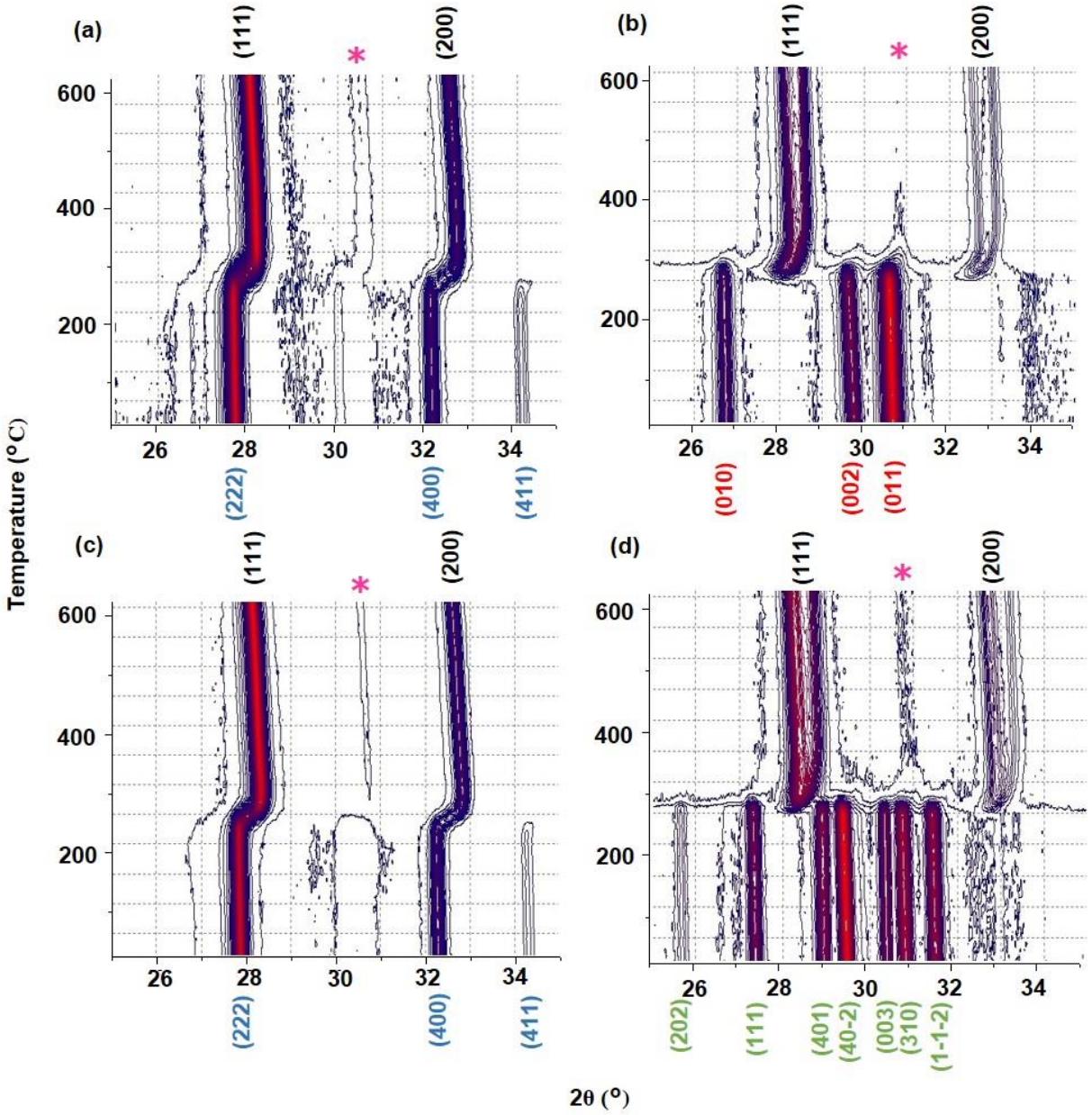

Figure 5.9: Contour plots showing the oxidation in oxygen of (a) and (b) $Y_{0.05}Pr_{1.95}O_3$; and (c) and (d) $Y_{0.2}Pr_{1.8}O_3$. Figures are annotated with the Miller indices of the respective peaks belonging to the (red) trigonal (A); (green) monoclinic (B); (blue) cubic bixbyite (C); and (black) cubic fluorite phases. Magenta star represents the (111) peak from tungsten radiation, visible due to the decay of the anode. Intensities are shown as constant increments from blue to red.

5.5. Conclusions

The Pr-rich compositions of the $Y_{2-x}Pr_xO_{3+\delta}$ series ($0.05 \leq x \leq 0.8$) were explored using a combination of X-ray and neutron powder diffraction experiments. Previously, only cubic bixbyite (C) and defect fluorite phases were known for this series. Using both *in-situ* and *ex-situ* techniques, the phase transitions of the series under non-oxidizing conditions are reported. For the $x = 0.05$ composition a direct phase transition from the cubic bixbyite (C) to the trigonal (A) structure is seen, whereas compositions with $x \geq 0.2$ show a direct cubic bixbyite (C) to monoclinic (B) transition. Intermediate compositions show a more complicated 3-phase regime. Structural details of the novel trigonal (A) $Y_{0.05}Pr_{1.95}O_3$ and monoclinic (B) $Y_{0.2}Pr_{1.8}O_3$ are reported, revealing site preference in the monoclinic (B) phase only. *In-situ* X-ray diffraction is used to understand the oxidation of all three phases, with all compositions oxidizing to the defect fluorite structure at low temperatures. However, only the cubic bixbyite (C) phase is able to accommodate additional oxide anions without first realizing an oxidative phase transition. Comments are made on how the results found in this manuscript are able to bring otherwise unknown details to the lanthanide sesquioxide phase diagram, and aid in the rational design of future functional materials.

5.6. Acknowledgements

M.B. acknowledges the support from NSERC, CFI and MIF. J.A.L. is thankful for financial support from the University of Manitoba and the NSERC Postgraduate Scholarship-Doctoral program, and would like to thank the “Modern Methods in Rietveld Refinement for Structural Analysis” School along with all instructors for data collection and help with Rietveld refinements. The authors also recognize Graham Devitt and Kevin Szkop for help with syntheses. We would like to thank Saul Lapidus from the APS for data collection and technical help. Use of the Advanced Photon Source at Argonne National Laboratory was supported by the U. S. Department of Energy, Office of Science, Office of Basic Energy Sciences, under Contract No. DE-AC02-06CH11357. A portion of this research at ORNL's Spallation Neutron Source was sponsored by the Scientific User Facilities Division, Office of Basic Energy Sciences, U.S. Department of Energy. The Authors would like to thank Melanie Kirkham and Ashfia Huq for data collection and technical help with POWGEN data, and Katharine Page for data collection and technical help with NOMAD data.

References

(1) Adachi, G.-Y.; Imanaka, N. The Binary Rare Earth Oxides. *Chem. Rev.* **1998**, *98* (94), 1479–1514.

(2) Zinkevich, M. Thermodynamics of Rare Earth Sesquioxides. *Prog. Mater. Sci.* **2007**, *52* (4), 597–647.

(3) Warshaw, I.; Roy, R. Polymorphism of the Rare Earth Sesquioxides. *J. Phys. Chem.* **1961**, *65* (11), 2048–2051.

(4) Goldschmidt, V. M.; Ulrich, F.; Barth, T. Geochemische Verteilungsgesetze der Elemente. *Mater. Naturv.* **1925**, *5*, 5–24.

(5) Foex, M.; Traverse, J. P. Polymorphism of Rare Earth Sesquioxides at High Temperatures. *Rev. Int. des hautes Temp. des Refract.* **1966**, *3*, 429.

(6) Aldebert, P.; Traverse, J. P. Etude Par Diffraction Neutronique Des Structures de Haute Temperature de La_2O_3 et Nd_2O_3. *Mater. Res. Bull.* **1979**, *14* (3), 303–323.

(7) Gouteron, J.; Michel, D.; Lejus, A. M.; Zarembowitch, J. Raman Spectra of Lanthanide Sesquioxide Single Crystals: Correlation between A and B-Type Structures. *J. Solid State Chem.* **1981**, *38* (3), 288–296.

(8) Greis, O. A Contribution to the Structural Chemistry of A-Type Rare Earth Sesquioxides. *J. Solid State Chem.* **1980**, *34* (1), 39–44.

(9) Pauling, L. The Crystal Structure of the A-Modification of the Rare-Earth Sesquioxides. *Z. Kristallogr.* **1929**, *69*, 415–421.

(10) Greis, O.; Ziel, R.; Breidenstein, B.; Haase, A.; Petzel, T. The Crystal Structure of the Low-Temperature A-Type Modification of Pr_2O_3 from X-Ray Powder and Electron Single

Crystal Diffraction. *J. Alloys Compd.* **1995**, *216* (2), 255–258.

(11) Heiba, Z. K.; Arda, L. X-Ray Diffraction Analysis of Powder and Thin Film of $(Gd_{1-x}Y_x)_2O_3$. *Cryst. Res. Technol.* **2008**, *43* (3), 282–288.

(12) Atkinson, S. C. Crystal Structures and Phase Transitions in the Rare Earth Oxides, University of Salford, 2013.

(13) Giussani, A.; Zaumseil, P.; Seifarth, O.; Storck, P.; Schroeder, T. A Novel Engineered Oxide Buffer Approach for Fully Lattice-Matched SOI Heterostructures. *New J. Phys.* **2010**, *12* (9), 93005.

(14) Seifarth, O.; Schubert, M. A.; Giussani, A.; Klenov, D. O.; Schmeier, D.; Schroeder, T. Single Crystalline $Pr_{2-x}Y_xO_3$ (x = 0-2) Dielectrics on Si with Tailored Electronic and Crystallographic Structure. In *Journal of Applied Physics*; American Institute of PhysicsAIP, 2010; Vol. 108, p 103709.

(15) Niu, G.; Zoellner, M. H.; Zaumseil, P.; Pouliopoulos, A.; D'Acapito, F.; Schroeder, T.; Boscherini, F. X-Ray Diffraction and Extended X-Ray Absorption Fine Structure Study of Epitaxial Mixed Ternary Bixbyite $Pr_xY_{2-x}O_3$ (x = 0 – 2) Films on Si (111). *J. Appl. Phys.* **2013**, *113* (4), 43504.

(16) Seifarth, O.; Dietrich, B.; Zaumseil, P.; Giussani, A.; Schroeder, T.; Storck, P. Integration of Strained and Relaxed Silicon Thin Films on Silicon Wafers via Engineered Oxide Heterostructures: Experiment and Theory. *IEEE Trans. Power Syst.* **1993**, *8* (3), 1366–1374.

(17) Lussier, J. A.; Devitt, G.; Szkop, K. M.; Bieringer, M. Oxygen Trapping and Cation Site-Splitting in $Y_{(2-x)}Pr_xO_{3+\delta}$ ($0.0 \leq x \leq 2.00$ and $\delta \leq 1.0$). *J. Solid State Chem.* **2016**, *242*, 126–132.

(18) Sears, V. F. Neutron Scattering Lengths and Cross Sections. *Neutron News* **1992**, *3* (3), 26–37.

(19) Lussier, J. A.; Szkop, K. M.; Sharma, A. Z.; Wiebe, C. R.; Bieringer, M. Order/Disorder and in Situ Oxide Defect Control in the Bixbyite Phase $YPrO_{3+\delta}$ ($0 \leq \delta < 0.5$). *Inorg. Chem.* **2016**, *55* (5), 2381–2389.

(20) Wang, J.; Toby, B. H.; Lee, P. L.; Ribaud, L.; Antao, S. M.; Kurtz, C.; Ramanathan, M.; Von Dreele, R. B.; Beno, M. A. A Dedicated Powder Diffraction Beamline at the Advanced Photon Source: Commissioning and Early Operational Results. *Rev. Sci. Instrum.* **2008**, *79* (8), 1–7.

(21) Neuefeind, J.; Feygenson, M.; Carruth, J.; Hoffmann, R.; Chipley, K. K. The Nanoscale Ordered MAterials Diffractometer NOMAD at the Spallation Neutron Source SNS. *Nucl. Instruments Methods Phys. Res. Sect. B* **2012**, *287*, 68–75.

(22) Arnold, O.; Bilheux, J. C.; Borreguero, J. M.; Buts, A.; Campbell, S. I.; Chapon, L.; Doucet, M.; Draper, N.; Ferraz Leal, R.; Gigg, M. A.; et al. Mantid—Data Analysis and Visualization Package for Neutron Scattering and μ SR Experiments. *Nucl. Instruments Methods Phys. Res. Sect. A* **2014**, *764*, 156–166.

(23) Rodriguez-Carvajal, J. FullProf.2K. Full Prof 2K V. 4.40 2013.

(24) Shannon, R. D. Revised Effective Ionic Radii and Systematic Studies of Interatomic Distances in Halides and Chalcogenides. *Acta Crystallogr.* **1976**, *A32* (5), 751–767.

Chapter 6. Conclusion and Future Directions

There is no doubt that the defect fluorite structure will continue to play a crucial role as fast ion conductors for future solid-state oxide electrolytes. In order to design and successfully synthesize these materials, research is required to understand the synthesis techniques, structure, and high temperature properties they exhibit. Throughout this thesis, a key theme has been to understand the synthesis and structure – reactivity relationships of a number of different materials belonging to the $Y_{2-x}Pr_xO_{3+\delta}$ and $Sc_{2-x}V_xO_{3+\delta}$ series. Using in-situ diffraction techniques to study phase transitions, redox processes, and reaction pathways has facilitated a deeper understanding of the materials of interest. In stark contrast, the majority of studies in the literature contain only ex-situ methods. Focusing on materials with multivalent cations to form intrinsic vacancies has allowed for in-situ techniques to investigate the formation and annihilation of defects. Using this approach rather than the traditional approach of doping has allowed for insights into the effect of oxide defects on structural properties and chemical reactivity.

The phase-pure synthesis of the $Y_{2-x}Pr_xO_{3+\delta}$ series using the sol-gel method shows the importance of understanding synthetic techniques, and choosing the correct synthesis method for the intended product. Comments on the different synthesis strategies (reductive vs. oxidative vs. sol-gel) are rationalized using structural details and reactivity studies. Combined powder neutron and X-ray Rietveld refinements were employed to decipher structural details including the addition of oxide anions on the *16c* site and a novel cation site-split model for oxidized bixbyites. The response of the $Y^{3+}/Pr^{3+}/Pr^{4+}$ cation sublattice to additional oxide anions and the onset of the fluorite structure were explored in detail. The compositions close to $Y_{0.6}Pr_{1.4}O_{3+\delta}$ are predicted to

have the greatest ion mobility do to the ideal ratio of holes to anions allowing for the greatest number of oxide vacancies while maintaining the defect fluorite structure. Magnetic susceptibility and thermogravimetric analysis were utilized in order to confirm oxidation states of some members of the series.

It was found that further structural control of the Pr-rich compositions of the$Y_{2-x}Pr_xO_{3.00}$ series could be realized by heating samples under non-oxidizing conditions. Using both in-situ and ex-situ studies, the phase transitions between the trigonal (A), monoclinic (B), and cubic bixbyite (C) A_2O_3 phases were explored. Combined neutron and X-ray Rietveld refinements were used to understand the structures of each phase, comparing the results to the well-known phase diagram of the lanthanide sesquioxides, revealed that average cation size is one of the most important factors in predicting the phase of the material. The oxidation pathways of all three phases was studied, with all phases showing oxidation to the defect fluorite at low temperature, suggesting that all structures are related. Only the cubic bixbyite (C) structure, however, shows an uptake of oxide, all others requiring an oxidative phase transition before any additional anions can be accommodated.

The $Sc_{2-x}V_xO_{3+\delta}$ series was also explored, in contrast to the $Y_{2-x}Pr_xO_{3+\delta}$ series, the reduced scandium vanadates do not form a solid solution for the whole series. Bixbyite phases are found for samples where $x \leq 1.08$ and corundum phases are found where $x \geq 1.68$. Intermediate compositions show a mixture of $Sc_{0.92}V_{1.08}O_{3.0}$ and $Sc_{0.32}V_{1.68}O_{3.0}$. The comparison of different synthesis strategies shows that using a 2-step method where reduction of $ScVO_4$ is used to form $ScVO_3$ forms highly crystalline materials in comparison to the direct synthesis. Combined neutron and X-ray Rietveld refinements reveal structural details of the bixbyite materials, including the preference of vanadium for the *8b* site. In-situ oxidations of the series emphasize the close

relationship between the bixbyite and the fluorite, showing topotactic oxidation of the bixbyite phase, while the corundum phase requires higher temperatures to oxidize. Furthermore, no excess oxygen can be added to the corundum phase, and an oxidative decomposition is found.

In this thesis simple systems are used as models to understand relationships between structure and reactivity. A focus on the fluorite structure and related structures were explored in order to understand and target specific design criteria for solid oxide electrolytes in the future.

Further work should focus on progressing from structure – reactivity relationships to structure – property relationships. Using electrochemical techniques such as impedance spectroscopy to explore the oxide ion conductivity in these series is of particular interest. A systematic study of ionic conductivity while varying cation ratios and oxide defect concentrations seems like a logical first step. However, in order to truly understand the relationship between the structures and ion conductivities of these materials simultaneous impedance spectroscopy and in-situ diffraction should be explored.

Furthering the mechanistic redox studies of these materials can include isothermal oxidation/reduction using a variety of different gases. Changing the reduction potential of the oxidant/reductant used can also be accomplished by mixing gases (i.e. CO_2 and CO or N_2 and H_2) Adjusting the temperature to the topotactic regime, or to the reconstructive oxidation regime can gain insights into the movement of ions in crystal structures. Understanding these processes is a first step to reporting mechanisms of solid-state reactions. Furthermore, with recent advances to instrumentation, exploring local structure using pair distribution function (pdf) analysis is much simpler and can greatly aid in this endeavor.

Adopting some of the structural findings from this thesis, in particular the site split cation model, to other candidates, should also be explored. This is an important structural detail, which is quite

easy to overlook if the focus of the research is not on the structure. This model should be applied to other oxidized bixbyite materials in order to ensure that reliable structures are reported.

Finally, expanding to mixed anion systems is of great interest for these materials. Incorporating halides such as F^- or Cl^- to form oxyhalides can massively impact the properties of the materials. The ability to further alter the ratio between cation oxidation state and oxygen defect concentration allows access to a series of tunable materials which can expand the stability field of the defect fluorite by preventing zircon formation.

This thesis brings to light the importance of understanding syntheses and structural details when designing materials. It shows the powerful tool that in-situ diffraction has become in order to identify new materials, understand reactions, facilitate synthesis, and further develop the field of solid-state chemistry.